Technical Report

WIND LOADS ON A HOUSE ROOF

by

K. J. Dreher

and

J. E. Cermak

Prepared Under

National Bureau of Standards
Contract No. NBS 273-70

Fluid Dynamics and Diffusion Laboratory
College of Engineering
Colorado State University
Fort Collins, Colorado 80521

March 1973

CER72-73KJD-JEC22

ABSTRACT

WIND LOADS ON A HOUSE ROOF

The wind loads on the roof of a house were experimentally investigated by placing a 1:50 scale model house in a wind tunnel capable of generating thick, turbulent shear flows. The effects of roof geometry and wind direction were isolated by making the wind-tunnel flow representative of natural winds over very flat, open terrain. This flow simulation was accomplished by placing vortex generators at the entrance to the wind-tunnel test section. Mean pressures, root-mean-square values of the fluctuating pressures, and instantaneous peak pressures were measured at 11 preselected locations on the model's roof for 24 wind directions. A secondary purpose of the study was to determine the effects of an upwind fence on the roof pressures.

ACKNOWLEDGMENTS

The support of the National Bureau of Standards Center for Building Technology in conducting this investigation is gratefully appreciated. The model and instrumentation provided by NBS along with the helpful suggestions offered by Dr. R. D. Marshall are especially appreciated.

TABLE OF CONTENTS

TABLE OF CONTENTS - Continued

LIST OF FIGURES

LIST OF FIGURES - Continued

LIST OF FIGURES - Continued

LIST OF SYMBOLS

Symbol

$C_{\overline{p}}$	=	mean pressure coefficient
C_{p}'	=	fluctuating pressure coefficient (RMS)
$C_{p_{peak}}$	=	instantaneous peak pressure coefficient
C_{p_o}	=	specific heat at constant pressure
d	=	perpendicular distance from house to fence
E	=	mean voltage
Ec	=	Eckert number
e	=	fluctuating voltage about mean voltage
g	=	gravitational acceleration
H	=	height of model house
K	=	thermal conductivity
k	=	Kármán constant
L	=	length
n	=	exponent in power-law formulation of mean velocity
P	=	a pressure difference
Pr	=	Prandtl number
p	=	total local pressure
Re	=	Reynolds number
Ri	=	Richardson number
Ro	=	Rossby number
T	=	total temperature
Tu_x	=	local longitudinal turbulence intensity
t	=	time
U	=	mean longitudinal velocity

Symbol

u	=	total local longitudinal velocity
u_*	=	"friction velocity"
x_i, x_j, x_k	=	orthogonal coordinates
z	=	vertical height above ground
z_o	=	surface roughness height

Greek symbols

α	=	wind incidence angle
Δ	=	difference
δ_{ij}	=	Kronecker Delta
ε_{ijk}	=	permutation tensor
Ω	=	earth's angular velocity for rotation about its own axis
ϕ	=	dissipation function
ρ	=	density
$\rho_x(\tau)$	=	autocorrelation coefficient for longitudinal velocity fluctuations
θ'	=	fluctuating temperature about mean temperature
τ	=	delay time
ν	=	kinematic viscosity

Subscripts

i,j,k	=	directions of orthogonal axes
o	=	reference quantity
RMS	=	root-mean-square value of fluctuations
ref	=	reference quantity

Superscripts

*	=	nondimensional quantity

Symbol

Additional symbols

$\langle\ \rangle$	=	mean quantity
$\overline{(\ \ )}$	=	mean quantity
$(\ )'$	=	fluctuating quantity about a mean quantity

Chapter I

INTRODUCTION

During the last twenty years, engineers have increasingly realized the importance of wind loads for all types of structures. Recent disasters such as Hurricanes Camille and Celia in 1969 and 1970 are vivid examples of what can happen if wind effects are not fully taken into account. Except for hurricanes and tornadoes, complete destruction of buildings by wind is rare. However, local failures of roofs, cladding, and glass are both common and more costly in the aggregate than complete failures.

Single-family houses in high-wind areas experience large, negative roof pressures which can lead to local failures. Figure 1 shows roof damage of varying severity on houses which were exposed to the winds of Hurricane Camille. Inspection teams surveying the damage made several interesting observations (Refs. 9 and 24). First, the shape of the roof seemed to be a major factor in the extent of damage. Hip roofs (see Figure 2) generally suffered much less damage than gabled roofs. Another major factor was the amount of roof overhang. Severe roof damage usually appeared to be initiated by the loss of large overhangs or carports. Therefore, more information describing the wind loads on house roofs is needed.

At the present time, the only satisfactory method of predicting wind loads is the use of large wind tunnels for measuring aerodynamic pressures on model structures. These pressures are converted into nondimensional pressure coefficients which are used with a design wind speed to obtain design loads.

1.1 Purpose and Scope

The primary purpose of this investigation is to determine the pressure distribution over a typical gabled roof with an overhang as a function of wind direction. The prototype house chosen for modeling is shown in Figure 3. This 2,000 sq-ft ranch-style house is located on Malmstrom Air Force Base (MAFB) near Great Falls, Montana. The 1:50 scale model shown in Figure 4 was immersed in a thick, turbulent, wind-tunnel shear flow. The model flow was designed to be typical of flows over extremely open land so that effects of wind direction and roof geometry could be isolated. This shear flow was established by using triangular-shaped vortex generators without any upstream roughness. Mean, fluctuating, and instantaneous peak pressures were measured at eleven points on the model's roof for 24 wind directions. A secondary purpose of the study was to investigate the effect of a fence upon roof pressures. A model of a solid fence was introduced upwind of the house and the effect on the roof pressures for varying house-to-fence distances determined.

This investigation was performed to supplement a joint study conducted by the National Bureau of Standards Center for Building Technology and the Fluid Dynamics and Diffusion Laboratory at Colorado State University. This joint investigation was undertaken to correlate full-scale roof pressures measured on the prototype house at MAFB with pressures obtained from model tests. A brief description of this study is included as Appendix C to this report.

1.2 Literature Review

1.2.1 Wind Loads on Houses - Several wind-tunnel simulations have previously been conducted to investigate the action of the wind on

houses (Refs. 5, 11, 12, and 14). The results presented in Refs. 5 and 11 were obtained from uniform wind-tunnel flows which do not adequately represent conditions in natural winds. Therefore, these results are of little practical importance and will not be described.

The purpose of Jensen's paper (Ref. 12) was to show that the Reynolds number is not the essential parameter in the aerodynamics of the natural wind. Rather, the natural wind with neutral thermal stratification depends on the surface roughness over which it is developed. Jensen confirmed this by measuring wind-induced pressures on a small, full-scale house with a gabled roof in natural winds. These were compared with measurements taken during tests on a 1:20 scale model using flows developed in a wind tunnel over varying heights of roughness. Jensen concluded that mean wind loads obtained from a model house in an appropriate wind tunnel could be made to agree within 10% of the actual loads. To accomplish this, the ratio between wind-tunnel roughness height and full-scale roughness height must be maintained between 0.6 and 1.7 times the chosen geometric scale. In addition, the wind tunnel must be long enough to allow the boundary-layer flow to fully develop and become at least several times thicker than the height of the model house.

Besides including a more detailed explanation of the above, Jensen and Frank (Ref. 14) present the results of many more wind-tunnel tests using model houses. Various full-scale roughness conditions were simulated by using smooth masonite, sandpaper, corrugated paper, broken stones, and randomly placed wooden strips as roughness on the wind-tunnel floor. Several sizes of model houses were used with flat, desk, gabled, and hip roofs; none had overhangs. Unfortunately, Jensen and

Frank lacked the necessary equipment to measure fluctuating pressures, and their work was limited to measurement of mean quantities only.

1.2.2 Use of Vortex Generators - Several investigators have used vortex generators for two purposes: to stimulate boundary layer growth when a wind-tunnel test section long enough to allow sufficient natural growth was not available; and to introduce a larger eddy size than might otherwise be attainable. The most notable efforts are presented in Refs. 6 and 23.

Counihan (Ref. 6) proposes the use of quarter-ellipse wedge-shaped vortex generators in combination with an upstream castellated barrier and appropriate surface roughness. The velocity gradients, turbulence intensities, and turbulence scales are adjusted by changing the height and spacing of the generators along with the dimensions and position of the barrier. Results are presented which are in satisfactory agreement with existing full-scale data for flow over rural areas.

Spire-shaped vortex generators similar to the ones used in this investigation have been used by Standen (Ref. 23), and favorable results again obtained. Standen varied the spire height from six inches to seven feet in free-stream velocities varying from 50 ft/sec to 100 ft/sec. Several modifications were also investigated. These included hole patterns in the spires, removed sections of the spires, and vertical splitter plates attached to the downstream side of the spires. Standen concluded that in order to successfully simulate the turbulent properties of natural winds, both splitter plates and roughness elements downstream of the spires must be used.

Chapter II

ORIGIN OF WIND-INDUCED ROOF PRESSURES

When a building is in the path of the wind, the air flow is deflected. The resultant change in momentum causes pressure to act on the building. Depending on the part of the building being considered and its structural geometry, this pressure can be positive or negative and can fluctuate rapidly or be fairly stable.

2.1 Mean Pressures

Figure 5 is an idealistic sketch of the steady-state flow* over a house with a gabled roof. In the approaching turbulent wind, the air follows mean streamlines which are basically parallel to the ground surface. The presence of the house causes the wind to change direction which results in the distortion of the velocity and pressure fields. The displacement zone in Figure 5 is defined as the region in which either velocity distortion is greater than 5% or pressure distortion is greater than 10% of the approaching parallel flow. Near the house, an adverse pressure gradient exists causing the kinetic energy of the air stream along the ground surface to dissipate. This dissipation continues until finally the particles of air next to the ground no longer have enough kinetic energy to further penetrate the region of increased pressure. The air particles then separate and flow over the shelter zone in front of the house.

---

*Throughout this paper, the assumption is made that the flow over a bluff object such as a building is self-stationary. Hence, both the flow field and wind-induced pressures are implicitly assumed to be ergodic random processes.

The shelter zone is bounded by the discontinuity surface shown in Figure 5. This surface is a vortex-sheet which passes up in a concave curve to the windward edge of the roof. If the house has a roof slope 30° or less, the surface of discontinuity will have an inclination at the windward roof edge which is larger than the roof slope (Ref. 14). Since the air stream is unable to accelerate enough to follow the roof surface, it separates from the roof at the windward edge. The air stream can reattach itself near the top of the windward slope or on the ridge of the roof depending on the width and the inclination of the roof. Hence, the mean wind-induced pressures are negative (suction) over most of the windward roof slope. Conversely, if the roof slope is greater than 30°, the discontinuity surface is inclined less at the windward edge than the roof slope. Separation will not occur, and the time-averaged pressures will be positive over the windward slope.

The house being considered in this investigation has a roof slope of 10.5°. As a result, separation will occur at the windward roof edge, and the pressures over most of the windward slope will be negative.

At the roof ridge separation will inevitably occur, and the discontinuity surface will continue in a convex upwards curve from the ridge to leeward of the house. On this side of the house, a cavity* exists where fluid motion is characterized by a large loss of momentum, large eddy motion, low pressure, and strong turbulent mixing. Thus, the mean pressures on the leeward roof slope are always negative.

---

*The cavity size is a function of both the length and height of the house. Figure 5 shows the cavity extending downwind a distance of two to three times the house height. However, for an infinitely long house, the cavity length would increase to approximately 12 times the height of the house.

2.2 Fluctuating Pressures

In addition to the generation of mean pressures, the atmospheric wind always causes fluctuating pressures. These fluctuations are the result of combinations of the following disturbances: (Ref. 2)

(1) atmospheric turbulence;

(2) reattachment on the building of flows which have separated;

(3) vortex formation;

(4) wakes shed from upwind buildings; and

(5) oscillation of the building.

Not only do these disturbances produce pressure fluctuations, they also affect the mean roof pressures.

Since this investigation is concerned with the effects of roof geometry and wind direction, disturbance (4) is not considered. Also, the height-to-width ratio of a typical house is so small that disturbance (5) is negligible. Of the three other disturbances, flow reattachment and the formation of vortices cause the largest pressure fluctuations. However, atmospheric turbulence interacts with these disturbances and its effect must not be regarded as negligible.

Separation and reattachment of the air stream has already been briefly described. While flow separation from simple building roofs is limited to sharp edges or corners, reattachment points are unsteady in position and form what is called the reattachment zone. Normally, surface pressures in this zone are quite variable with large pulsations occurring frequently. Reattachment is not only dependent on the roof geometry but also depends on the amount of atmospheric turbulence. There is some experimental evidence which indicates turbulence can hasten reattachment (Ref. 22).

Even larger pressure fluctuations are likely to occur when conical edge vortices form in the region where the air flow is separated. Figure 6 shows a flow visualization with smoke of two vortices forming on the flat roof of a model building located in a thick, turbulent boundary layer. Additional cases of vortex formation on buildings with desk roofs (see Figure 2) are presented in Ref. 17 by Ostrowski, et al. Vortex flow is not common to all roof geometries and exists over a limited range of wind directions. The severest pressure pulsations occur along the edges where the vortices are formed. Again, the gustiness of the wind can affect vortex formation.

Figure 7 shows the locations where vortex flow is expected to develop on the house being studied in this investigation. The wind direction shown is skewed approximately 45° with respect to the main axis of the house. A similar vortex flow would exist for winds approaching the house 180° from the direction shown.

Chapter III

MODELING CRITERIA

In order for any wind-tunnel flow to exactly represent a prototype flow with a different scale length, the two flows must be:

(1) geometrically similar;

(2) dynamically similar;

(3) thermally similar;

(4) kinematically similar; and

(5) their boundary conditions must be similar.

These similarity conditions are described by performing an inspectional analysis of the governing equations of motion (continuity, momentum and energy). Unfortunately, exact simulation of the atmospheric boundary layer in a wind tunnel is not presently possible. As a result, approximate or partial similarity is achieved by requiring exact equality for the most important factors while those of lesser importance are approximated. The general discussion which follows is largely based on developments found in Refs. 1, 3, and 4.

3.1 Geometric and Mass-Flow Similarity

Geometric similarity is satisfied simply by using an undistorted scale model. The model used in this study was constructed with a common length scale of 1/50th the vertical and horizontal dimensions of the prototype house at MAFB.

Assuming geometric similarity, the tensor form of the continuity equation

$$\frac{\partial \rho}{\partial t} + \frac{\partial (\rho u_i)}{\partial x_i} = 0 \qquad (i=1,2,3) \tag{1}$$

is examined. The variables in this equation can be expressed in dimensionless form by using the following scaling factors:

$$\rho^* = \frac{\rho}{\rho_o} , \quad t^* = \frac{t\ U_o}{L_o} , \quad u_i^* = \frac{u_i}{U_o} , \text{ and } \quad x_i^* = \frac{x_i}{L_o} .$$

Substitution into the continuity equation for ρ , t , u_i , and x_i yields the dimensionless continuity equation

$$\frac{\partial \rho^*}{\partial t^*} + \frac{\partial (\rho^* u_i^*)}{\partial x_i^*} = 0 \tag{2}$$

which is exactly the same as the original equation. Therefore, mass-flow similarity is automatically satisfied when geometric similarity exists.

3.2 Dynamic Similarity

Requirements for dynamic similarity result from consideration of the momentum equation. The following equation is the tensor form of the time-averaged instantaneous momentum equation in a fixed frame of reference:

$$\frac{\partial \bar{u}_i}{\partial t} + \bar{u}_j \frac{\partial \bar{u}_i}{\partial x_j} + \frac{\partial \langle u_i' u_j' \rangle}{\partial x_j} + 2\varepsilon_{ijk}\Omega_j \bar{u}_k = - \frac{1}{\rho_o} \frac{\partial \bar{P}}{\partial x_i} - g \frac{\Delta \bar{T}}{\bar{T}_o} \delta_{i3} + \nu_o \frac{\partial^2 \bar{u}_i}{\partial x_k \partial x_k} . \tag{3}$$

The dependent variables in this equation have been replaced by a mean value plus a fluctuation about the mean. The term $[-g\delta_{i3}\Delta\bar{T}/\bar{T}_o]$ expresses the temperature stratification effect as a body force. This term is based on the Boussinesq approximation which limits Eq. 3 to flows where $\Delta\bar{T} << \bar{T}_o$. The approximation results in $\bar{P}$ being the pressure difference between the mean pressure in the flow and the hydrostatic pressure for air of density ρ_o . Equation 3 is

nondimensionlized by using the same scaling factors as for the continuity equation plus the following additional factors:

$$\bar{u}_i^* = \frac{\bar{u}_i}{U_o} , \quad (u_i')^* = \frac{u_i'}{U_o} , \quad \Omega_j^* = \frac{\Omega_j}{\Omega_o} , \quad \bar{P}^* = \frac{\bar{P}}{\rho_o U_o^2} ,$$

$$\Delta\bar{T}^* = \frac{\Delta\bar{T}}{(\Delta\bar{T})_o} , \text{ and } \quad g^* = \frac{g}{g_o} .$$

Substituting for the variables in Eq. 3 and dividing by U_o^2/L_o yields the dimensionless momentum equation

$$\frac{\partial \bar{u}_i^*}{\partial t^*} + \bar{u}_j^* \frac{\partial \bar{u}_i^*}{\partial x_j^*} + \frac{\partial \langle u_i' u_j' \rangle^*}{\partial x_j^*} + \left[\frac{L_o \Omega_o}{U_o} \right] 2\varepsilon_{ijk} \Omega_j^* \bar{u}_k^*$$

$$= - \frac{1}{\rho_o} \frac{\partial \bar{P}^*}{\partial x_i^*} - \left[\frac{(\Delta\bar{T})_o}{\bar{T}_o} \frac{L_o g_o}{U_o^2} \right] \Delta\bar{T}^* g^* \delta_{i3} + \left[\frac{\nu_o}{U_o L_o} \right] \frac{\partial^2 \bar{u}_i^*}{\partial x_k^* \partial x_k^*} . \tag{4}$$

Exact dynamic similarity between wind-tunnel and prototype flows requires that the three dimensionless parameters formed by the inspectional analysis procedure be equal for both flows. These parameters have been given the following names:

Rossby number - $Ro = U_o/L_o\Omega_o$

Reynolds number - $Re = U_o L_o/\nu_o$

bulk Richardson number - $Ri = [(\Delta\bar{T})_o/\bar{T}_o][L_o g_o/U_o^2]$.

3.2.1 Rossby Number Equality - The Rossby number can be interpreted physically as the ratio of convective inertial forces to rotational inertial forces. Although some attempts have been made, current laboratory facilities cannot provide Rossby number equality. Hence, this similarity requirement must usually be relaxed. Fortunately, most natural winds of interest have Rossby numbers on the order of

10^{-1} which means the earth's rotation is negligible. Only when characteristic lengths of the prototype flow exceed 500,000 ft do the earth's rotational effects become important.

3.2.2 Reynolds Number Equality - The Reynolds number physically represents the ratio of convective inertial forces to viscous forces. Similarity requires that

$$\left[\frac{U_o L_o}{\nu_o} \right]_{\text{prototype}} = \left[\frac{U_o L_o}{\nu_o} \right]_{\text{model}} . \qquad (5)$$

The prototype house in this study is approximately 10 ft high. If a wind with a velocity of 40 ft/sec is assumed to act on this house, then Eq. 5 requires $(U_o L_o)_{\text{model}} = 400$ ft^2/sec. One configuration satisfying this requirement would be a 4-ft high model placed in a wind tunnel capable of velocities to 100 ft/sec. Obviously this requirement cannot be easily met. Thus, Reynolds number equality is relaxed and the model velocity is set equal to the prototype velocity. This implies

$$\left[\frac{L_o}{t} \right]_{\text{prototype}} = \left[\frac{L_o}{t} \right]_{\text{model}} .$$

For a model scale of 1:50, this means events related to the wind such as pressure fluctuations will occur 50 times faster than in the prototype flow.

When flow around buildings with sharp edges is being considered, the relaxation of Reynolds number equality does not introduce serious error. This is because separation of the flow from the building will always occur at certain of the sharp edges as determined by the building geometry and orientation with respect to the approaching wind. Since the points of separation are fairly constant, the flow patterns in the

vicinity of the separated region will not strongly depend on the flow velocity. All other essential relations in this flow region must also be rather independent of the velocity. Therefore, the nondimensional pressure coefficients are Reynolds number independent provided the Reynolds number is large enough to indicate that the flow is a fully rough flow. The lower Reynolds number limit is approximately of the order 10^5 (Ref. 19). Based on the smallest dimension of the house cross-section, the Reynolds number in this model study is larger than 10^5. The independence of wind-induced pressures from Reynolds number has been experimentaly verified during a number of wind-tunnel tests. (For example see Refs. 16 and 19.)

3.2.3 Richardson Number Equality - The bulk Richardson number is the ratio of buoyancy forces to inertial forces. This implies

$$Ri = \frac{\text{restoring force in a unit mass of air}}{\text{inertial force in a unit mass of air}}$$

$$= \frac{\text{rate of consumption of turbulent energy by buoyancy force}}{\text{rate of production of turbulent energy by the mean wind shear.}}$$

Therefore, $Ri > 0$ means the flow is stably stratified; $Ri = 0$ means the flow is neutral; and $Ri < 0$ means the flow is unstably stratified. For this study, as for most structural aerodynamic studies, the wind velocity and turbulence intensities are assumed to be high enough so that intense turbulent mixing takes place. Hence, temperature gradients are assumed to be equal to the adiabatic lapse rate for the atmosphere and zero for the model. Therefore, $(Ri)_{prototype} = (Ri)_{model} = 0$.

3.3 Thermal Similarity

To determine thermal similarity, the same nondimensionalizing procedure is applied to the time-averaged instanteous energy equation

$$\frac{\partial \overline{T}}{\partial t} + \overline{u}_i \frac{\partial \overline{T}}{\partial x_i} + \frac{\partial\, \theta' u_i'}{\partial x_i} = \left[\frac{K_o}{\rho_o C_{p_o}} \right] \frac{\partial^2 \overline{T}}{\partial x_k \partial x_k} + \frac{\phi}{\rho_o C_{p_o}} \qquad (6)$$

where ϕ is the dissipation function. The additional scaling factors needed are $\overline{T}^* = \overline{T}/(\overline{\Delta T})_o$, $\theta'^* = \theta'/(\overline{\Delta T})_o$, and $\phi^* = \phi L_o^2/U_o^2 \rho_o \nu_o$. After substitution, the following dimensionless equation is formed:

$$\frac{\partial \overline{T}^*}{\partial t^*} + \overline{u}_i^* \frac{\partial \overline{T}^*}{\partial x_i^*} + \frac{\partial \langle \theta' u_i' \rangle^*}{\partial x_i^*} = \left[\frac{K_o}{\rho_o C_{p_o} \nu_o} \right] \left[\frac{\nu_o}{U_o L_o} \right] \frac{\partial^2 \overline{T}^*}{\partial x_k^* \partial x_k^*} +$$

$$+ \left[\frac{\nu_o}{U_o L_o} \right] \left[\frac{U_o^2}{C_{p_o} (\Delta \overline{T})_o} \right] \phi^* \ . \qquad (7)$$

Two more dimensionless similarity parameters are generated. They are:

Prandtl number - $Pr = \rho_o \nu_o C_{p_o} / K_o$

Eckert number - $Ec = U_o^2 / C_{p_o} (\Delta \overline{T})_o$.

The Prandtl number is the ratio of molecular viscosity to thermal diffusivity. When air is used as the model fluid, the Prandtl number automatically equals that for the atmosphere. The Eckert number expresses the relative importance of heat due to friction and compression. Since flows in structural aerodynamic studies involve velocities much smaller than the speed of sound, a negligible amount of heat is generated by friction and compression. Consequently, the Eckert number is another similarity parameter which is commonly ignored.

3.4 Boundary Condition Similarity

Similarity of boundary conditions requires geometric similarity of the lower boundary, of upstream conditions, of flow conditions at the upper boundary, and a zero pressure gradient in the direction of the mean flow.

For this investigation, the prototype house was assumed to be located in extremely flat and open surroundings with little vegetation of any kind. This exposure was chosen so that effects of roof geometry and wind direction could be determined without the added effects from upstream buildings, trees, etc. To insure that the model was immersed in a thick turbulent flow with the same mean velocity gradient and turbulence structure as the assumed prototype flow, three vortex generators together with a tripping fence were placed at the entrance of the wind-tunnel test section. Roughness elements were not added downwind of the generators in order to determine the effectiveness of the vortex generators alone in simulating the flow.

The upper boundary for the model flow was chosen to correspond to a prototype height of 200 ft. Although the gradient wind height could be as high as 1000 ft for a flow over this type of terrain, it is not likely that winds above 100 ft contribute very much to the wind loads on a house with this exposure.

Unfortunately, the longitudinal pressure gradient in the wind tunnel could not be set to zero since the wind-tunnel ceiling had no provisions for height adjustment. However, this should not introduce significant errors in the pressures acting on the model house. Not only is the pressure gradient in this wind tunnel relatively small, but the more important regions of the flow are of very limited extent.

3.5 Kinematic Similarity

Kinematic similarity requires the same patterns of streamlines for model and prototype flow fields. This condition is automatically satisfied when all the other similarity conditions are met.

3.6 The Model-Law of Jensen

A brief description of Jensen's investigations has already been presented in Chapter I. The importance of his work was that he showed reliable results from wind-tunnel studies could be obtained provided the ratio of upwind surface roughness height z_o to structure height H for the model is within 0.6 and 1.7 times the ratio for the prototype flow. But this is merely a summarized statement of the similarity requirements presented above. However, simply providing the appropriate upwind roughness in a wind tunnel will not always produce a flow containing the longer wave-length turbulence which produce low-frequency pressure fluctuations.

Chapter IV

EXPERIMENTAL FACILITIES

4.1 Wind Tunnel

The wind tunnel used to simulate flow conditions in this experimental investigation was the low-speed wind tunnel of the Fluid Dynamics and Diffusion Laboratory at Colorado State University. As shown in Figure 8, this tunnel is of the closed circuit type and has a working section 36.50 ft long. The axial-flow blower is driven by a 75 hp constant speed motor. The blower is capable of generating wind speeds of 65 ft/sec in the 6 ft-by-6 ft test section (without vortex generators). The wind speed can be changed continuously by varying the fan blade pitch.

The model house was placed a distance of 33.75 ft downstream of the entrance to the working section. Figure 9 shows the location of a pitot-static tube for continuous monitoring of the reference velocity in the center of the test section at a height of 4 ft above the wind-tunnel floor. The reference velocity was maintained at 71 ft/sec with the vortex generators in place*.

4.2 Vortex Generators

Three spire-shaped vortex generators were placed at the entrance of the wind-tunnel test section along with a triangular-shaped fence. The purpose of the vortex generators was to stimulate growth of the boundary layer and to introduce large-scale turbulence. The triangular

---

* The vortex generators constrict the cross-sectional area of the lower part of the entrance to the wind-tunnel working section thereby causing higher velocities in the upper part of the entrance section.

fence was used to generate turbulence of smaller wave lengths and to help promote mixing of the vortices shed from the spires. The spires and fence are shown installed in the wind tunnel in Figure C3. Their pertinent dimensions are given in Figures 10 and 11.

The dimensions and spacing of the spired generators were determined by trial and error. Constructed from 3/8-in. plywood, their height and width were varied until the best combination of flow uniformity and agreement with prototype flow structure was obtained at the location of the model.

4.3 The Model House

The 1:50 scale model house shown in Figure 4 was constructed by the National Bureau of Standards Center for Building Technology (NBS). The part of the model in the left of Figure 4 consists of a solid piece of hard wood with a 3/16-in. thick plastic roof. The hollow portion of the model was constructed from 3/16-in. "Lucite." The bottom of both the solid and hollow parts was made from 1/4-in. "Lucite" which was fastened to a 1/16-in. thick metal plate. The circular portion of this plate had a diameter of 15 in. and provided a convenient means for positioning the model over the hole for the pressure transducer lines in the wind-tunnel floor.

Figure 12 shows the location and numbering of the eleven pressure taps in the roof. The pressure taps were located where the wind-induced pressures were expected to be the largest. These anticipated locations were determined from a preliminary wind-tunnel test conducted in the small wind tunnel of the National Bureau of Standards. The pressure taps were made by drilling 3/32-in. holes in the roof of the

model. These holes were then joined by 1/8-in. diameter holes drilled approximately half the thickness of the roof from the inside. Small plastic taps were then glued in the 1/8-in. holes so that pressure tubing could be connected.

As a last step, all the joints in the model were sealed with Dow Corning 781 silicone rubber sealant. This was done to insure that the pressure inside the hollow part of the model would remain at a constant level when exposed to the turbulent wind-tunnel flow.

The final dimensions of the model house are shown in Figures 12 and 13. Based on these dimensions, the largest exposed cross-sectional area of the model is approximately 0.85% of the wind-tunnel cross-sectional area. Since this blockage is much less than the maximum allowable value of 5% (Ref. 14), the blockage effects of the model are negligible.

Chapter V

EXPERIMENTAL TECHNIQUE AND INSTRUMENTATION

The following sections describe the experimental procedure used to determine the structure of the simulated flow and the wind-induced pressures on the roof of the model house. Brief performance specifications for the instrumentation used during this study are included as Appendix A to this report.

5.1 Velocity and Turbulence Measurements

5.1.1 Mean Velocity Profile - The mean velocity profile was measured at the model location 33.75 ft downwind of the vortex generators with the model house removed. Velocity surveys were made directly in line with the center vortex generator and between generators. Measurements were made with both a pitot-static tube and a hot-wire anemometer attached to a heavy stand and securely anchored with piano wire.

The pitot-static tube was a 1/8-in. rounded-nose probe with an impact orifice of 1/32 in. Calibration against a National Physics Laboratory standard probe showed negligible differences between the two probes throughout the velocity range of interest (30-70 ft/sec). The static and dynamic ports of the pitot-static probe were connected to a pressure meter with 1/8-in. I.D. Tygon tubing. Small pieces of cotton were inserted in the tubing leading from the static port to damp fluctuations in the static pressure. The instrumentation scheme for mean velocity measurements is shown in Figure 14.

The 80% platinum - 20% iridium wire soldered on the tip of the hot-wire probe had a nominal diameter of 0.00025 in. and was 0.0625 in.

long. An overheat ratio* of 1.2 was used, and the hot-wire anemometer was calibrated against the pitot-static tube in the wind tunnel with the vortex generators removed at a height of 4 ft above the wind-tunnel floor. The calibration curves exhibited the linear relationship between the square of the voltage output and the square-root of the velocity known as King's law (Ref. 20). The calibration was reproducible within 3%. A sample calibration curve is provided by Figure 15. The hot-wire anemometer instrumentation used to measure mean velocities is shown in Figure 16.

5.1.2 Turbulence Measurements - The hot-wire anemometer used to measure mean velocities was also used to measure the longitudinal turbulence intensity and scale in the simulated flow. The turbulence intensity was measured simultaneously with the velocity profile at the model location, and the related instrumentation is shown in Figure 16. To measure the integral longitudinal scale of the turbulence, an auto-correlation of the longitudinal velocity fluctuations was made. The hot-wire probe was again attached to the heavy stand at the model position and securely anchored with piano wire. Measurements were made with the model removed both in line with the center vortex generator and between generators at a height of 5-3/16 in.** above the wind-tunnel floor. The instrumentation that was used is portrayed in Figure 17.

---

* The overheat ratio is defined as the ratio of the resistance of the wire when heated by the operating current to the resistance when unheated by current (cold resistance).

** This height corresponded to the height of the anemometer installed on the prototype house.

5.2 Pressure Measurements

5.2.1 Pressure Transducers - The mean, fluctuating, and peak pressures on the roof of the model house were measured by means of pressure transducers fastened underneath the model and connected to the pressure taps by flexible Tygon tubing. The tubing had an inside diameter of 1/8 in. and was used in 2 to 5 in. lengths.

Two different types of low-range, high-accuracy pressure transducers were used. The majority of the measurements were made with Validyne variable reluctance transducers supplied by NBS. The pressure sensing element in these transducers is a flat diaphragm of magnetic stainless steel clamped between case halves of the same material. Pickoff coils embedded in the case halves sense the diaphragm deflection when exposed to a pressure. Sine wave excitation is applied by a sine-wave carrier demodulator which also demodulates the output and amplifies the resulting DC signal. Figure 18 shows the frequency response of a typical transducer connected to 4.6 in. of 1/8-in. I.D. Tygon tubing. In order to damp out the large resonant peak, part of which is shown in Figure 18, a small piece of cotton was inserted in each end of the connecting tubing. The resulting improvement in the frequency response is also shown in Figure 18.

The other pressure transducer used was a Statham transducer. This transducer is quite similar to the variable reluctance transducers described above. The major differences are that the deflection of the pressure diaphragm is sensed by a strain gage, and the excitation is supplied by a DC voltage source directly resulting in a DC output signal. The frequency response of this transducer with a 3-in. length of 1/8-in. I.D. Tygon tubing without damping is shown in Figure 19.

Each pressure transducer was calibrated against the MKS pressure meter described in Appendix A. The resulting calibration curves were all linear within 1% and reproducible within 2%.

The reference pressure for each of the pressure transducers during the wind-tunnel investigation was taken as the ambient pressure at a height of 4 ft above the wind-tunnel floor. Thus, the reference port of each transducer was connected to the static side of the pitot-static tube used to monitor the reference velocity (see Figure 9). A long piece of Tygon tubing with cotton inserted was again used to damp fluctuations. The ambient pressure at this height is different from the static pressure at the height of the model. However, the static pressure indicated by a pitot-static tube at the model height could be in error because the flow streamlines are curved in the vicinity of the model, and the turbulence level is fairly large. Since the difference between the actual static pressure at these two heights should be small, the pitot-static tube located 4 ft above the wind-tunnel floor should provide a better indication of the static pressure at the model house.

5.2.2 Measurement of Roof Pressures as Functions of Wind Direction - To determine the variation of the mean, fluctuating, and instantaneous peak pressures with wind direction for each of the 11 pressure taps, the model was rotated to simulate the 24 approaching wind directions shown in Figure 20. For each wind direction, one-minute samples of the 11 output signals from the pressure transducers were simultaneously recorded on tape with a 14-channel tape recorder as shown in Figure 21. Later, the tapes were replayed one channel at a time using the instrumentation in Figure 22. The mean pressure at each pressure tap for each wind direction was determined by dividing

the output of the integrating voltmeter by the output of the time counter, while the average intensity of the pressure fluctuations was determined from the voltage output of the RMS meter. The storage oscilloscope was used to store the pressure fluctuations over the length of each sample record. At the end of the record, the absolute maximum voltage fluctuation was read from the oscilloscope and the instantaneous peak pressure thereby determined.

5.2.3 Measurement of the Effects of a Solid Fence - To determine the effects the presence of a solid fence has on mean, fluctuating, and peak roof pressures, the following procedure was used. The data from the previous test series were examined to find the angle of attack corresponding to the wind approaching the back of the house causing the severest pressures. The wind direction for $\alpha = 325^{o}$ (see Figure 20) was chosen, and the model house was appropriately oriented in the wind-tunnel test section. A solid metal fence corresponding to a prototype height of 58 in. was placed 6 in. upwind of the model parallel to the model's major axis. The fence extended across the entire test section (approximately four times the length of the model house). A preliminary check of the effects of the fence on the roof pressures where they were the largest without the fence (pressure taps #2, #3, and #4 in Figure 12) was conducted. It was determined that the effects at pressure tap #2 were representative of the effects at the other locations. The house-to-fence distance was then varied from 3 to 14 in. The mean, RMS fluctuating, and instantaneous peak pressures were then measured at pressure tap #2 using the instrumentation in Figures 21 and 22 directly without the tape recorder.

Chapter VI

EXPERIMENTAL RESULTS AND DISCUSSION

The data obtained by the procedure outlined in Chapter V are analyzed and discussed in this chapter. First, the important characteristics of the simulated flow are presented and compared with full-scale data. Then the nondimensional roof pressures are examined, and it is shown how they can be used to determine actual wind loads.

6.1 Structure of the Simulated Flow

6.1.1 Mean Velocity Profile - During this investigation, mean velocities were measured in absence of the model house at 1-in. intervals above the wind-tunnel floor to a height of 6 in. and then at 6-in. intervals to a height of 4 ft. The velocity at the 4-ft level, denoted as U_{ref}, was maintained at 71 ft/sec, and surveys were made both in line with the center vortex generator and between generators. The two velocity surveys differed a maximum of 3% indicating that the wakes of the individual vortex generators had satisfactorily mixed together.

Generally, mean velocity profiles over natural terrains with different degrees of roughness are either described by a power law or a logarithmic law. The former is expressed as

$$U(z) = z^n \tag{8}$$

where $U(z)$ is the mean velocity in the direction of the wind at a height z. The power-law exponent n is a function of the surface roughness height z_o (n increases as z_o increases) (Ref. 8). Normally, the exponent n is found by plotting the velocity profile on logarithmic graph paper and determining the slope of the resulting

straight line. The alternative logarithmic representation of mean velocity profiles for neutral atmospheric flows is

$$U(z) = \frac{u_*}{k} \ln \frac{z}{z_o} \tag{9}$$

where u_* is the "friction velocity" and k is the von Kármán constant (= 0.4). When mean velocity is plotted against height above ground level on log-linear graph paper, the slope of the resulting straight line determines u_*, and the z intercept equals z_o. For this investigation, the power law (Eq. 8) was used to describe the simulated velocity profile. The logarithmic law was not used because it implicitly implies the flow was naturally developed over roughness elements, and this was not the case for the wind-tunnel flow.

The mean velocity measurements obtained from the wind tunnel were represented in the following manner. Assuming the power law expression is valid,

$$U_{ref} = z_{ref}^{n} \quad . \tag{10}$$

Combining Eq. 10 with Eq. 8 gives the nondimensional power law:

$$\frac{U(z)}{U_{ref}} = \left(\frac{z}{z_{ref}}\right)^{n} \quad . \tag{11}$$

Figure 23 shows the resulting mean velocity profile. When z/z_{ref} was plotted against $U(z)/U_{ref}$ on logarithmic graph paper, two straight lines of different slopes were obtained. The two different values for the power-law exponent probably result from the absence of upstream roughness elements in the wind tunnel. That is, the velocity gradient established by the vortex generators deteriorates since there are no roughness elements to continue causing momentum losses in the flow

region along the wind-tunnel floor. However, only the lower region of flow (below the transition region in Figure 23) causes measurable pressures on the model house, and the existence of two velocity gradients should not introduce serious error.

The lower portion of the velocity profile in Figure 23 satisfactorily agrees with results from atmospheric observations found in the literature. For flows over flat, open terrain with few trees, values of the power-law exponent in the range 0.13 to 0.22 depending on the particular terrain are given in Ref. 8. Therefore, the value of 0.12 in this study indicates the model flow is representative of flow over the smoothest terrain likely to exist. Figure 24 shows the comparison between the velocity profile for the wind-tunnel flow and a profile for flow over a harrowed field given in Ref. 13. Adequate similarity again exists.

6.1.2 Turbulence Intensity - Turbulence intensity profiles in the wind tunnel were simultaneously measured with the mean velocities. The longitudinal turbulence intensity based on the local mean velocity is commonly denoted as

$$Tu_x = \frac{u_{RMS}(z)}{U(z)} \quad . \tag{12}$$

In this expression, $u_{RMS}(z)$ is the square-root of the mean-square velocity fluctuation parallel to the mean flow velocity $U(z)$. The turbulence intensities in this investigation were calculated from the following equation: (Ref. 20)

$$\frac{u_{RMS}}{U} = \frac{4(E)(e_{RMS})}{E^2 - E_o^2} \quad . \tag{13}$$

In this relationship, E and e are respectively the mean and fluctuating voltage drops across the probe of the hot-wire anemometer. The quantity E_o^2 is the intercept of the calibration curve in Figure 15 and was obtained by extending the straight line back rather than measuring the voltage output for $U = 0$. The turbulence intensities measured in line with the center vortex generator and between generators again differed a maximum of 3% indicating satisfactory flow uniformity.

The results of this analysis are shown in Figure 25. The apparent combination of two curves in Figure 25 is again due to the absence of roughness upwind of the model's location. That is, there were no roughness elements along the wind-tunnel floor to convert mean flow energy into turbulence. Also shown in Figure 25 are local turbulence intensities for two prototype flows. The turbulence intensities for the harrowed field were obtained by expressing the harrowed field velocity profile given in Figure 24 in terms of the logarithmic law (Eq. 9). The "friction velocity" u_* was thereby obtained and the turbulence intensities calculated from: (Ref. 15)

$$Tu_x = \frac{2.5\, u_*}{U(z)} \quad . \tag{14}$$

The turbulence intensities obtained in this manner are reasonably close to those measured in the wind tunnel. The turbulence intensity profile for the "open country" flow is included in Figure 25 to show the range of variation in data found in the literature. This profile was obtained by using a nomogram based on many atmospheric observations found in Ref. 18. A value of 1 cm for z_o presented in Ref. 8 as being representative of flow over "open country" was used with this nomogram.

However, the resulting turbulence intensities are substantially larger than those obtained in the wind tunnel and probably are too high for the type of exposure considered in this study.

6.1.3 Integral Turbulence Scale - The autocorrelation function for the longitudinal velocity fluctuations was measured without the model at 5-1/4 in. above the wind-tunnel floor in line with the center vortex generator and between generators. Eight curves describing the autocorrelation coefficient as a function of delay time were obtained. One of these is shown in Figure 26. The autocorrelation coefficients for each curve at a given delay time were generally within 2% of each other indicating the validity of assuming the longitudinal velocity fluctuations in the wind tunnel form a random process that is self-stationary and therefore ergodic.

Assuming the Taylor hypothesis (Ref. 21), the average area under the autocorrelation curves was multiplied by the mean velocity at 5-1/4 in. above the floor of the wind tunnel. This yielded a characteristic length of the longitudinal turbulence in the flow known as the integral scale. The value of the integral scale 5-1/4 in. above the wind-tunnel floor is approximately 1 ft. This corresponds to a prototype value of 50 ft at a height of 21.9 ft above the ground surface. No satisfactory atmospheric measurements of the integral-scale length for flow over the smooth terrain assumed in this study could be found. The actual prototype value at the 21.9-ft level is probably on the order of 200 ft. Hence, the integral turbulence scale in the simulated flow is approximately four times too small. This means that the energy spectrum of the longitudinal velocity fluctuations in the simulated flow is shifted to frequencies that are four times higher than in the

prototype flow. However, the energy spectrum for the pressure fluctuations on the roof of a building does not generally occur over the same frequency range as the velocity fluctuations. Therefore, the effect of the energy shift due to a lack of turbulence-scale similarity between model and prototype cannot easily be determined. Although this lack of similarity exists in several other wind-tunnel simulations, no analysis of the effect on roof pressures could be found in the literature. The effect is probably relatively small since atmospheric turbulence is not the major cause of pressure fluctuations on building roofs (see Chapter II). However, measurable errors might be introduced in a model study if the integral scale in the wind tunnel is not large enough to ensure that the model building is encompassed by the turbulent eddies. In this model study, the integral scale length of 1 ft means that most of the roof of the model house was encompassed by individual turbulent eddies. Perhaps the only way to determine the amount of error introduced is to compare fluctuating pressures on a prototype building with those from model tests having varying turbulence scale lengths. Since this type of comparison will be made when the investigation described in Appendix C is completed, some information should soon be available.

6.2 Pressures on the Model House Roof

The model house was placed in the wind-tunnel flow and rotated to simulate the 24 wind directions shown in Figure 20. The mean, fluctuating, and instantaneous peak pressures were measured at each of the 11 pressure taps shown in Figure 12 for each wind direction. A solid model fence 0.46 times the height of the model house was then placed

at varying distances upwind of the house, and its effects on the pressure at one pressure tap for one wind direction determined.

6.2.1 Definition of Nondimensional Pressure Coefficients - The wind-induced pressure at any point on the surface of a building is directly proportional to the momentum of the approaching wind provided the Reynolds number is at least 10^5. Hence for a specific wind direction, knowledge of the pressures at one wind velocity enables the determination of the pressures for another wind velocity. Therefore, wind-induced pressures obtained from model studies are generally nondimensionalized with a characteristic dynamic pressure $(\frac{1}{2}\rho U^2)$ of the simulated flow.

During this investigation the following pressures were measured:

time-averaged (mean) pressure, $\overline{\Delta p} = \overline{p - p_{ref}}$

RMS fluctuating pressure, $\Delta p_{RMS} = [\overline{(p - p_{ref})^2}]^{\frac{1}{2}}$

instantaneous peak pressure, $\Delta p_{peak} = (p - p_{ref})_{maximum}$.

The pressure denoted p_{ref} in the above is the static pressure measured with the pitot-static tube shown in Figure 9 (see Chapter 5). The model roof pressures were then nondimensionalized and the following pressure coefficients formed:

$$C_{\overline{p}} = \frac{\overline{\Delta p}}{\rho U_H^2/2}$$

$$C_{p'} = \frac{\Delta p_{RMS}}{\rho U_H^2/2} \qquad (15)$$

$$C_{p_{peak}} = \frac{\Delta p_{peak}}{\rho U_H^2/2} .$$

In these expressions, U_H is the mean velocity at the height of the

roof ridge of the model house as shown in Figure 23, and ρ is the density of air which was taken as 0.00224 slugs/ft^3.

6.2.2 Roof Pressure as Functions of Wind Direction and Location - The mean, RMS, and peak pressure coefficients are plotted as functions of wind direction in Figures 27 through 37. The coefficients are also tabulated in Appendix B to this report. These Figures allow several interesting deductions.

First, the pressures on top of the entire roof are negative except immediately upwind of the chimney. This means the slope of the roof is small enough so that after the air stream separates from the windward roof edge, it never reattaches on the roof.

The severest pressures occur along the edge of roof where pressure taps #2, #3, #4, and #5 are located. This corresponds with the observation that roof damage on house roofs from hurricane Camille (see Figure 1) usually occurred at the ends of roofs. These large pressures are clearly shown in Figures 39 through 43 which show the mean, RMS, and peak pressure distributions for the winds approaching the front and back of the house which cause the severest pressures. Also, the pressures at pressure taps #2, #3, #4, and #5 in Figures 28, 29, 30, and 31 respectively show the same general variation with wind direction. The maximum pressures at these taps all occur within the limited range of $\alpha = 215° - 240°$. The largest mean pressure, $C_{\bar{p}} = -1.62$, occurs at pressure tap #4 when $\alpha = 225°$; the largest fluctuating (RMS) pressure, $C_{p'} = 0.42$, also occurs at pressure tap #4 when $\alpha = 215°$; and the largest peak pressure, $C_{p_{peak}} = -4.15$, occurs at pressure tap #2 when $\alpha = 240°$. The most consistent large pressure fluctuations and peak pressures occur at pressure tap #4 for

α = 205° - 245°. This is probably the result of vortex flow forming at the tip of the roof ridge as shown in Figure 7.

Another significant result is that even though the average fluctuating pressures are relatively small ($C_{p'} < 0.5$ at all pressure taps and for all wind directions), very large peak fluctuations occur. The ratio of $C_{p_{peak}}/C_{p'}$ is approximately 20 at some pressure taps for certain wind directions. The value of this ratio appears to change randomly with wind direction and from pressure tap to pressure tap. Hence, the ratio of $C_{p_{peak}}/C_{p'}$ does not have any general meaning in this study. If the pressure fluctuations conformed to the Gaussian distribution of a random variable as is sometimes assumed, the ratio $C_{p_{peak}}/C_{p'}$ would equal 4 (Ref. 7). Therefore, pressure fluctuations on house roofs are not Gaussian. This is in agreement with results presented by Davenport in Ref. 7.

Similarly, no generalizations can be made about the ratio $C_{\bar{p}}/C_{p'}$, or the ratio $C_{p_{peak}}/C_{\bar{p}}$. However, changes in the peak pressure vaguely correspond to changes in the mean pressure. This is shown in Figures 38, 39, 42, and 43 in which the peak pressure distributions have approximately the same shapes as the corresponding mean pressure distributions.

As expected, pressures underneath the overhangs are positive when on the windward side of the house and negative when on the leeward side of the house. The significance of the pressures underneath the overhangs is that they either enhance or reduce the effects of pressures on the top side of the roof edges. For example, the maximum mean pressure, $C_{\bar{p}} = -1.62$, occurs at pressure tap #4 when $\alpha = 225°$. However, the mean pressure coefficient representative of the total pressure at this point

is

$$(\bar{C_p})_{\#4} - (\bar{C_p})_{\#10} = -(1.62 + 1.14)$$
$$= -2.56 .$$

Therefore, the ability of a roof to withstand wind loading is definitely related to the size of its overhang. This procedure cannot be extended to calculate total fluctuating and peak pressures because no measurements were made of the cross-correlation function between pressures underneath and on top of the roof overhang.

The effects of the chimney appear to be quite minimal. The only noticeable effect occurs when the wind approached the side of the roof on which the chimney was located. For this orientation, the presence of the chimney caused a local zone of positive pressure as shown in Figures 33 and 38. No effects on the pressure fluctuations were observed.

Unfortunately, it is not possible to compare the above results with any previous work. The results presented in Refs. 5 and 11 are of little value since they were obtained in a uniform wind-tunnel flow rather than in a shear flow. Jensen (Ref. 12) showed that results obtained in uniform flows can be in error as much as 300%. The results published by Jensen and Frank (Ref. 14), although valid, cannot be used for direct comparison since no tests were performed on model houses with geometry comparable to the house in this investigation. However, the mean pressure coefficients Jensen and Frank obtained have maximum values occurring at approximately the same wind directions and are of the same order of magnitude as the mean coefficients obtained in this study.

6.2.3 Effects of a Solid Fence - Wind-induced pressures on buildings are very complex functions which strongly depend on building geometry, wind direction, and upwind conditions. When using the results of a wind-tunnel test to predict wind loads on a prototype building, the limitations of the results obtained from the model must be recognized. For instance, a fence located upwind of a house greatly affects the roof pressures. An example of the effects on the house in this study is shown in Figure 44. The effects on the fluctuating and peak pressures are very unsteady because of the eddies shed from the fence. Although the mean pressures are effectively reduced throughout most of the range for d/H considered, the fluctuating and peak pressures are substantially enhanced as d/H becomes larger than about 2.8. However, these pressures could also be reduced by increasing the fence height so that the eddies shed from the fence pass over the top of the house. Unfortunately, not enough data are available from this investigation to determine the minimum height required.

6.3 Determination of Actual Wind Loads from Pressure Coefficients

There are several problems associated with using pressure coefficients to determine actual wind loads. First, the overall effect of the fluctuating and peak pressures as measured in this investigation cannot be determined. To adequately describe fluctuating and peak roof loads, information is needed about how individual pressure fluctuations in a given area correspond to each other. This requires the measurement of the correlation of fluctuating pressures in space and time. To obtain meaningful results from space-time correlations, simultaneous pressure measurements from a much denser array of pressure taps than

used in this study must be made. The significance of the fluctuating and peak pressure coefficients obtained during this investigation is that they provide an indication of the magnitude and location of the severest pressure fluctuations likely to occur. Thus a basis is formed for future measurement of space-time correlations.

Besides providing information about local wind loads, the mean pressure coefficients obtained in this study can be used to determine the average overall wind load. This is done by converting the non-dimensional pressure coefficients into local loads at a given wind speed. These local loads are then integrated over the surface of the roof resulting in the total load for a given section of the roof. However, the pressure coefficients are relative to the reference pressure used for the pressure transducers. Unfortunately, this pressure would rarely equal the pressure internal to the roof of the actual house. The internal pressure in any building is subject to open windows, chimneys, etc.

A conservative solution to this problem is to assume the most serious condition likely to exist. For the house in this study, the mean pressures over most of the roof were negative. Hence, the roof would experience the largest negative pressures when a window on the windward side of the house was open causing positive pressure on the underside of the roof. Consequently, the magnitude of this internal pressure, relative to the same ambient pressure to which the pressures on the outside surface of the roof were referenced, should be added to the magnitude of the mean external pressures in order to obtain the total negative roof pressures. Based on pressure measurements on windward walls made by Jensen and Frank (Ref. 14), a value for the

internal pressure coefficient of 0.8 should be representative of the maximum internal pressure likely to occur. Therefore, a conservative estimate of overall wind loads could be obtained by increasing the magnitude of the negative mean pressure coefficients by 0.8.

The value of the internal pressure has no effect on the wind loads acting on the roof overhangs. Instead, the pressure underneath the overhang must be combined with the top surface pressure as done on page 34 to determine the loads on the roof overhangs.

The most important factor which must be determined in order to calculate actual loads is the maximum wind speed to which the house will be exposed. Safety requires that this wind speed not be underestimated, while economy requires that the chosen wind speed not be too large. This type of information can be obtained from records of the local weather station.

Chapter VII

CONCLUSIONS

Wind loads on the roof of a house have been experimentally investigated by placing a scale model in an appropriate wind-tunnel flow. The following conclusions can be made from the results of this investigation:

1. Vortex generators can be used in a wind tunnel to satisfactorily simulate the lower 80 ft of the atmospheric wind over very flat, open terrain. The resulting power-law exponent is 0.12.
2. The wind-induced pressures over the entire roof of the house studied are negative except immediately upwind of the chimney for all wind directions. No other effects from the chimney were observed.
3. The random roof pressure fluctuations do not follow a Gaussian distribution.
4. The pressure underneath the overhangs of the roof can account for 50% of the total wind load acting on the overhangs.
5. The largest mean and fluctuating surface pressures occur along the roof edges at the ends of the roof when the wind direction is skewed 30° - 70° from the major axis of the house. The maximum pressure occurs immediately leeward of the roof peak when the wind direction is skewed 45° from the major axis of the house.
6. The existence of a solid fence upwind of a house can effectively reduce the magnitude of the mean pressures.

However, the magnitude of the fluctuating and peak pressures can be substantially increased.

7. Additional research is needed to determine the overall fluctuating wind loads acting on the roofs of houses located in high-wind areas, and the feasibility of using fences as windbreaks for unprotected houses.

REFERENCES

1. Cermak, J.E., "Laboratory Simulation of the Atmospheric Boundary Layer," AIAA Journal, Vol. 9, No. 9, September 1971, pp. 1746-1754.

2. Cermak, J.E., "Separation-Induced Pressure Fluctuations on Buildings," Presented at U.S. - Japan Research Seminar on Wind Loads on Structures, East-West Center, University of Hawaii, Honolulu, Hawaii, October 19-24, 1970, Paper CEP70-71JEC19, Colorado State University, Fort Collins, Colorado, 1970.

3. Cermak, J.E., and S.P.S. Arya, "Problems of Atmospheric Shear Flows and their Laboratory Simulation," Presented at AGARD Specialists' Meeting, Munich, Germany, September 15-17, 1969, Journal of Boundary Layer Meteorology, Vol. 1, No. 1, March 1970.

4. Cermak, J.E., V.A. Sandborn, E.J. Plate, G.H. Binder, H. Chuang, R.N. Meroney, and S. Ito, "Simulation of Atmospheric Motion by Wind-Tunnel Flows," Report CER66JEC-VAS-EJP-GJB-HC-RNM-SI17, Fluid Dynamics and Diffusion Laboratory, Colorado State University, Fort Collins, Colorado, May 1966.

5. Chien, N., Y. Feng, H.J. Wang, and T.T. Siato, "Wind-Tunnel Studies of Pressure Distribution on Elementary Building Forms," Iowa Institute of Hydraulic Research, Iowa City, Iowa, 1951.

6. Counihan, J., "A Method of Simulating a Neutral Atmospheric Boundary Layer in a Wind Tunnel," Presented at the Fluid Dynamics Panel Specialists' Meeting, Munich, Germany, AGARD Conference Proceedings, No. 48, September 1969, pp. 14.1-14.13.

7. Davenport, A.G., "Note on the Distribution of the Largest Value of a Random Function with Application to Gust Loading," Proceedings, Institution of Civil Engineers, London, vol. 28, May 1964, pp. 187-196.

8. Davenport, A.G., B.J. Vickery, N. Isynmov, T. Jandali, D. Surry, and M. Novak, "New Approaches to Design Against Wind Action," Course Notes from Seminar sponsored by the ASCE Committee on Continuing Education and the ASCE Task Committee on Wind Forces, 1972.

9. Dikkers, R.D., R.D. Marshall, and H.D.S. Thom, "Hurricane Camille - August 1969," NBS Technical Note 569, U.S. Department of Commerce, March 1971.

10. Gorove, Arpad and J.E. Cermak, "Dynamic Response of Pressure Transmission Lines to Pulse Input," Report CER66-67AP-JEC51, Fluid Dynamics and Diffusion Laboratory, Colorado State University, Fort Collins, Colorado, June 1967.

REFERENCES - Continued

11. Ishizaki, H. and C. Huh, "The Fluctuation of Wind Pressure on the Roof of a House," Technical Translation 1306, National Research Council of Canada, Ottawa, 1967.

12. Jensen, M., "The Model-Law for Phenomena in Natural Wind," Ingenioren (International Edition), Vol. 2, No. 4, 1958, pp. 121-128.

13. Jensen, M. and N. Frank, "Model-Scale Tests in Turbulent Wind," Part I - Phenomena Dependent on the Wind Speed, The Danish Technical Press, Copenhagen, 1963.

14. Jensen, M. and N. Frank, "Model-Scale Tests in Turbulent Wind," Part II - Phenomena Dependent on the Velocity Pressure, The Danish Technical Press, Copenhagen, 1965.

15. Lumely, J.L., and H.A. Panofsky, The Structure of Atmospheric Turbulence, New York: John Wiley & Sons, Inc., 1964.

16. Marshall, R.D. and J.E. Cermak, "Wind Studies of the Bank of America World Headquarters Building — Part II, Wind-Tunnel Study," Report CER66-67RDM-JEC19, Fluid Dynamics and Diffusion Laboratory, Colorado State University, Fort Collins, Colorado, October 1966.

17. Ostrowski, J.S., R.D. Marshall, and J.E. Cermak, "Vortex Formation and Pressure Fluctuations on Buildings," Paper 17, Proceedings, International Research Seminar on Wind Effects on Buildings and Structures, Ottawa, Canada, September 11-15, 1967, Vol. 1, University of Toronto Press, 1968, pp. 459-484.

18. Panofsky, H.A., et al., "Properties of Wind and Temperature at Round Hill, South Dartmouth, Mass.," Research and Development Technical Report ECOM-0035-F, U.S. Army Electronics Command, Atmospheric Sciences Laboratory, Research Division, Fort Huachuca, Arizona, August 1967.

19. Sadeh, W.Z., J.E. Cermak, and G. Hsi, "A Study of Wind Loading on Tall Structures — Atlantic-Richfield Plaza Buildings," Report CER68-69WZS-JEC-GH-36, Fluid Dynamics and Diffusion Laboratory, Colorado State University, Fort Collins, Colorado, August 1969.

20. Sandborn, V.A., "Metrology of Fluid Mechanics," Report CER66VAS32, Colorado State University, Fort Collins, Colorado, June 1968.

21. Schlichting, H., Boundary Layer Theory, 6th ed., New York: McGraw-Hill Book Company, Inc., 1968.

22. Scruton, C., "Aerodynamics of Structures," Paper 4, Proceedings, International Research Seminar on Wind Effects on Buildings and Structures, Ottawa, Canada, September 11-15, 1967, Vol. 1, University of Toronto Press, 1968, pp. 115-161.

REFERENCES - Continued

23. Standen, N.M., "A Spire Array for Generating Thick Turbulent Shear Layers for Natural Wind Simulation in Wind Tunnels," Laboratory Technical Report LTR-LA-94, National Aeronautical Establishment, Ottawa, Canada, May 1972.

24. Zorning, H.F. and G.E. Sherwood, "Wood Structures Survive Hurricane Camille's Winds," U.S.D.A. Forest Service Research Paper FPL 123, U.S. Department of Agriculture, October 1969.

FIGURES

(a) Residential area in Bay St. Louis, Mississippi (Ref. 9)

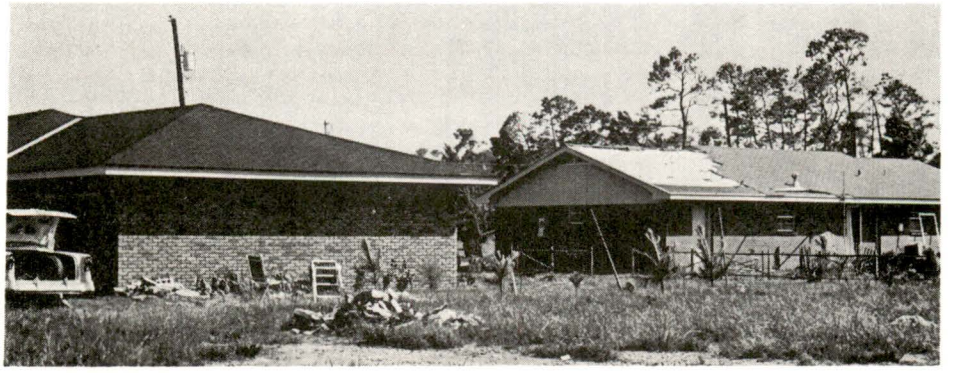

(b) Gabled roof with more damage than neighboring hip roof (Ref. 24)

Figure 1. Roof damage on houses after Hurricane Camille

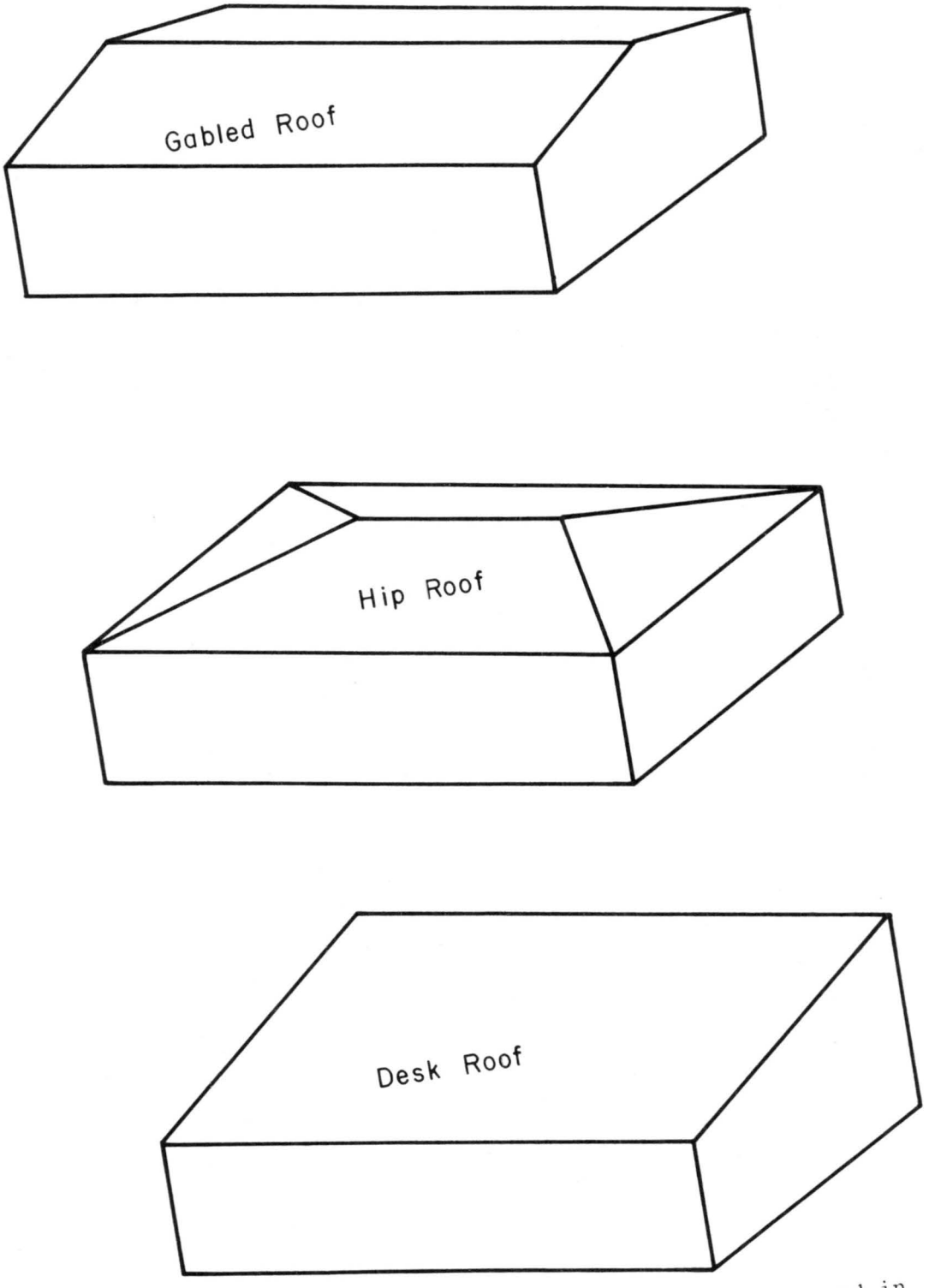

Figure 2. Roof configurations commonly found in residential areas

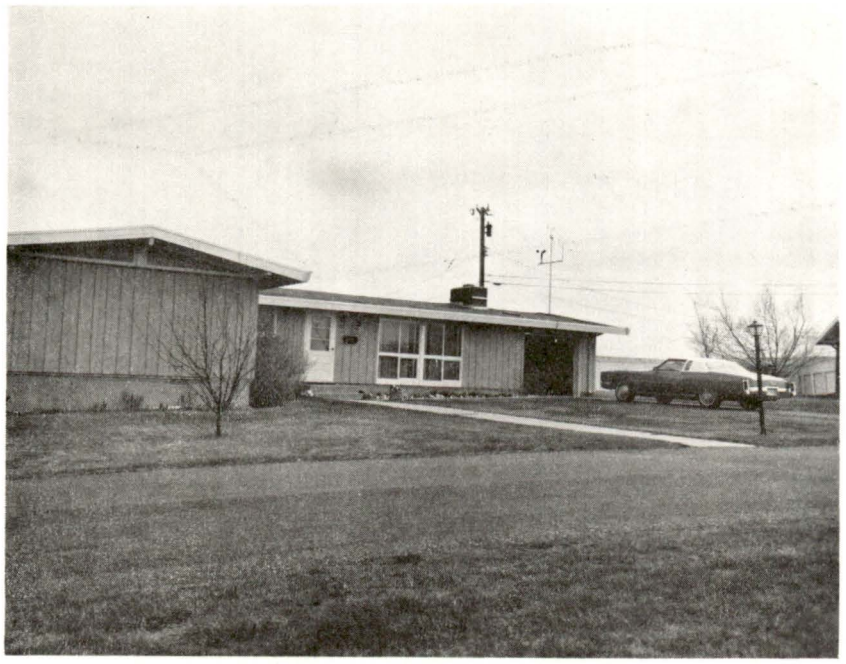

Figure 3. Prototype house

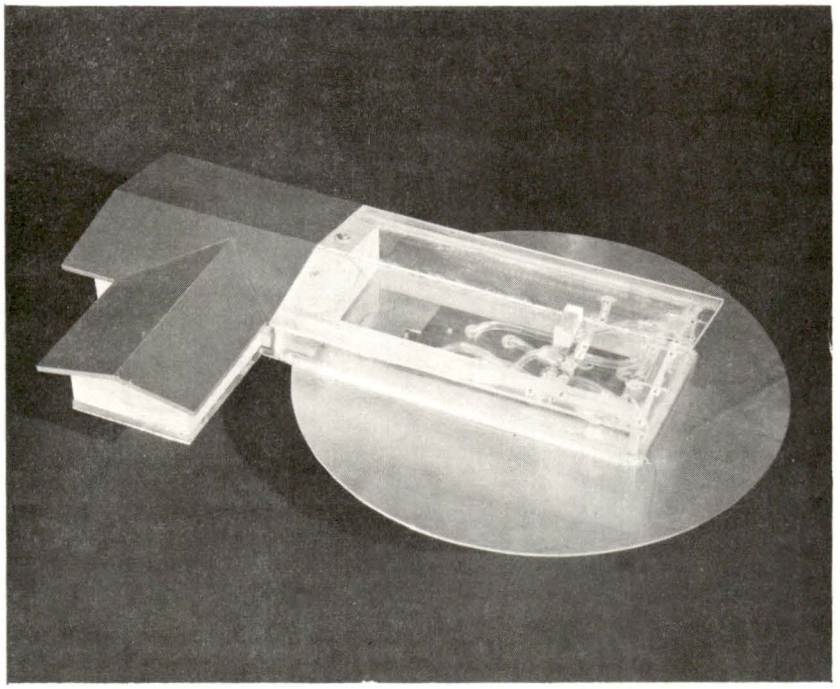

Figure 4. Model house

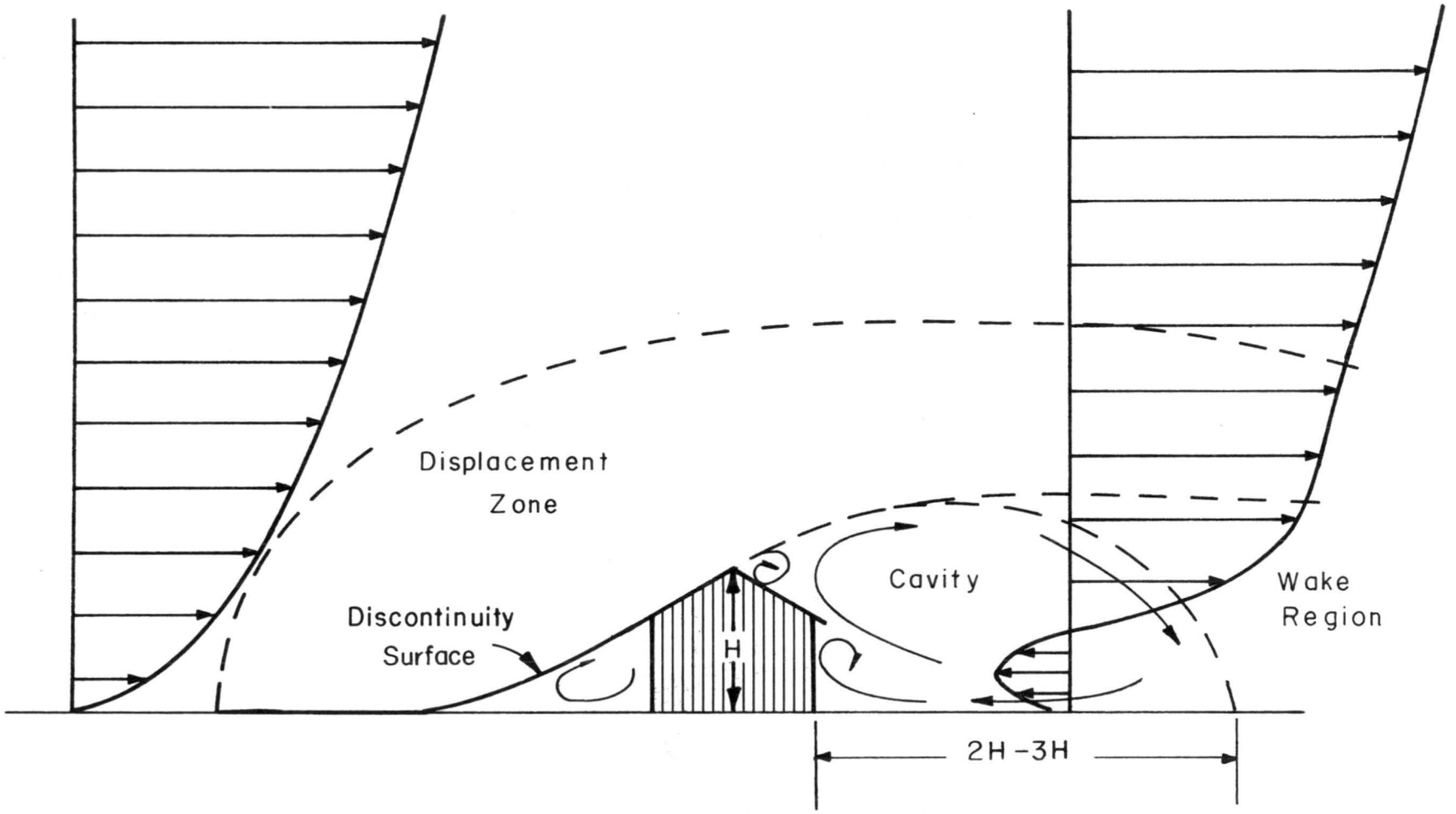

Figure 5. Mean flow pattern over a house

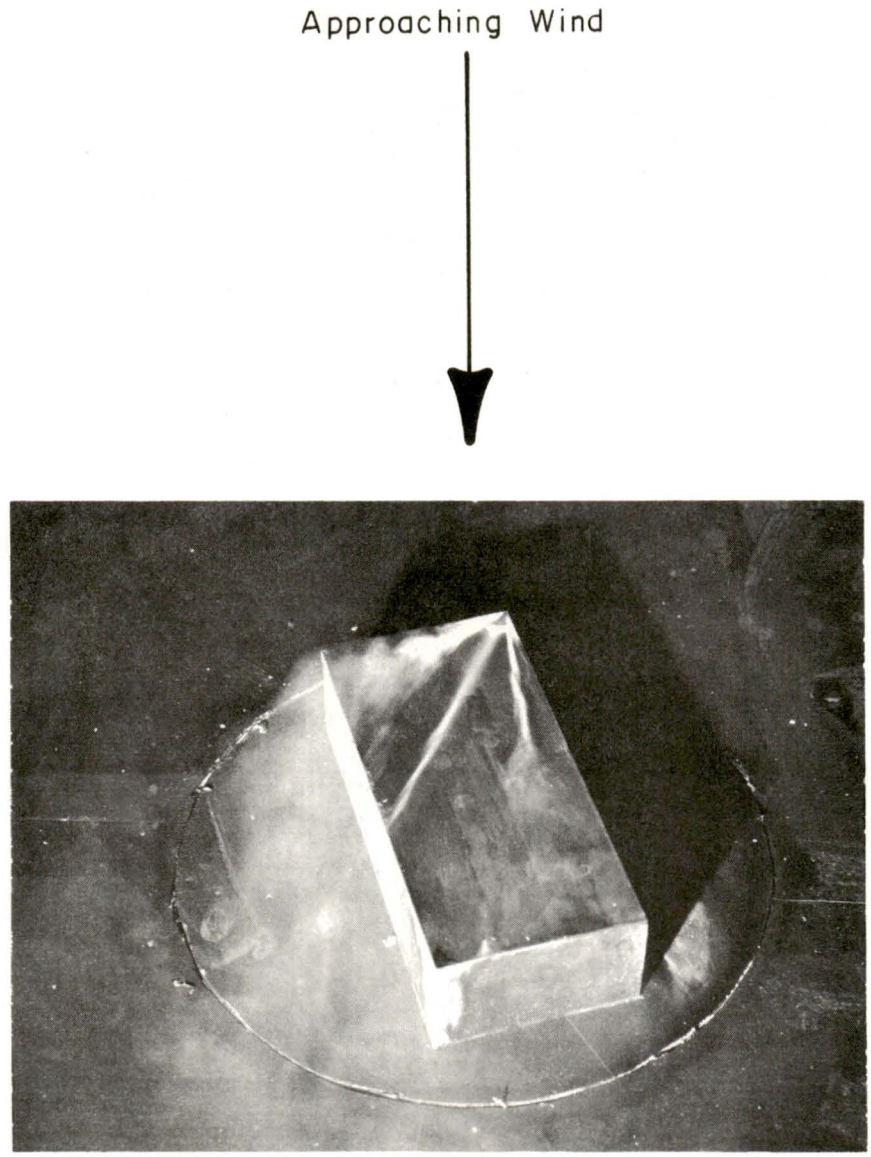

Figure 6. Flow visualization of conical vortices on flat-roofed model

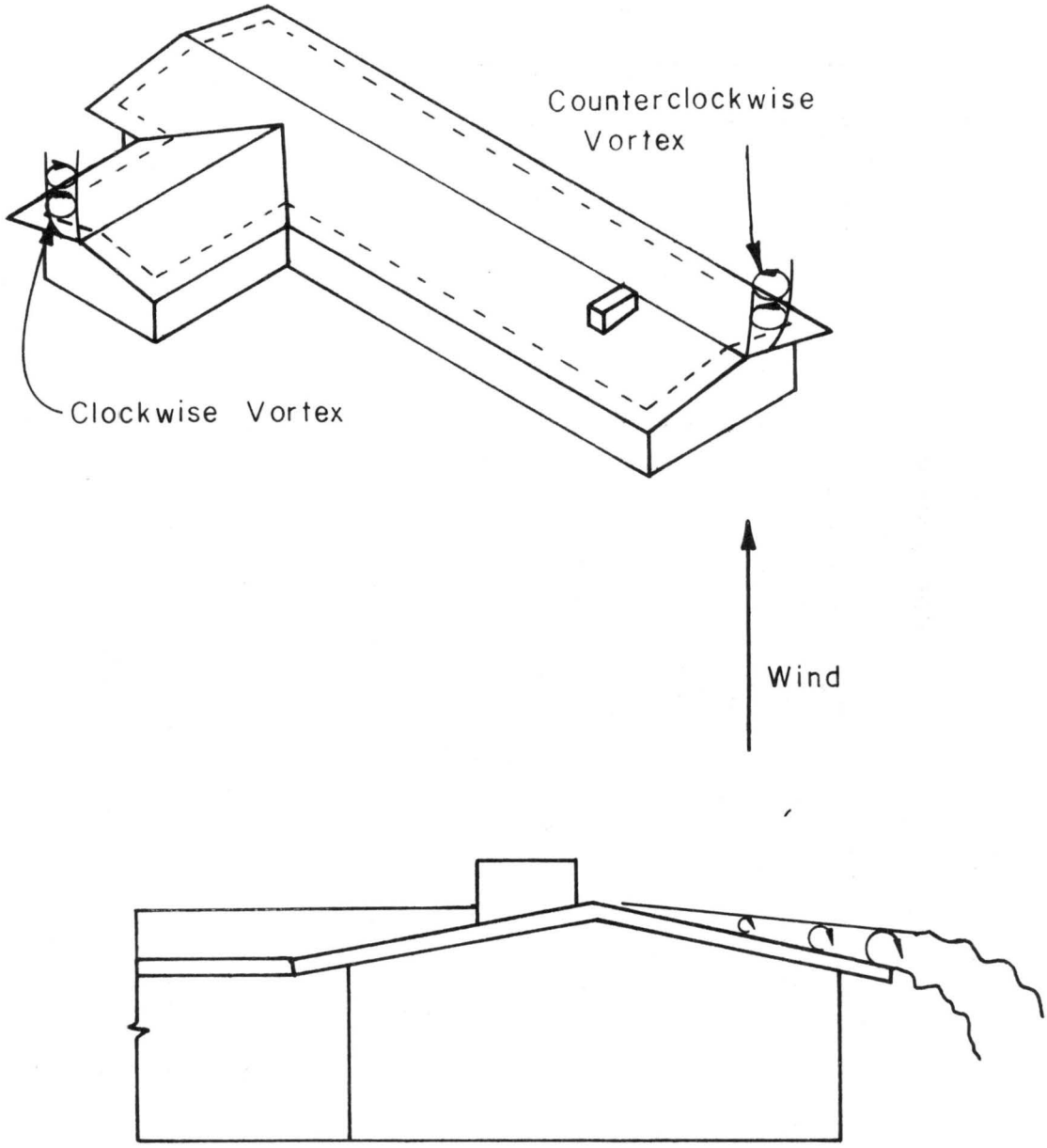

Figure 7. Probable vortex formation on house with gabled roof

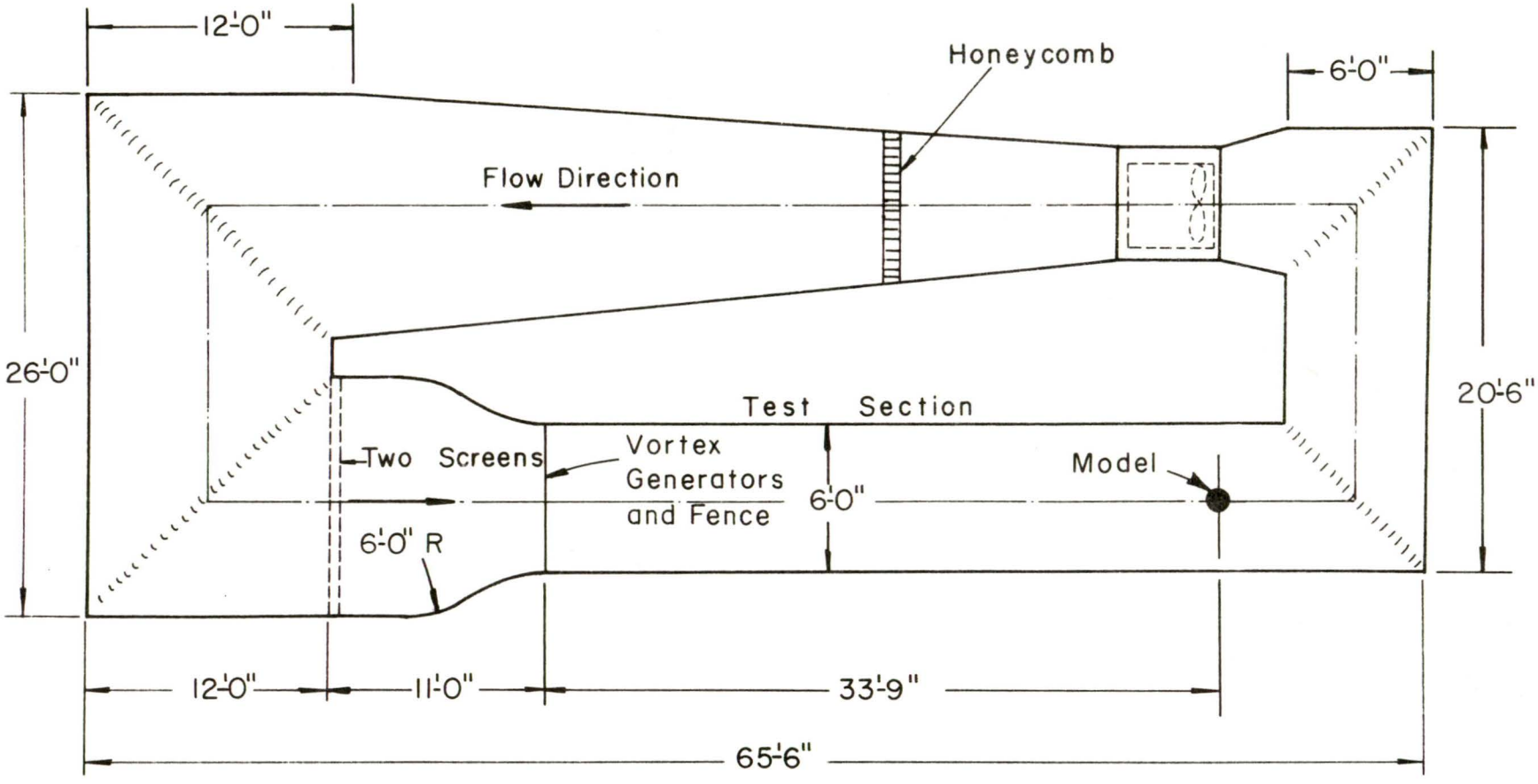

Figure 8. Top view of low-speed wind tunnel

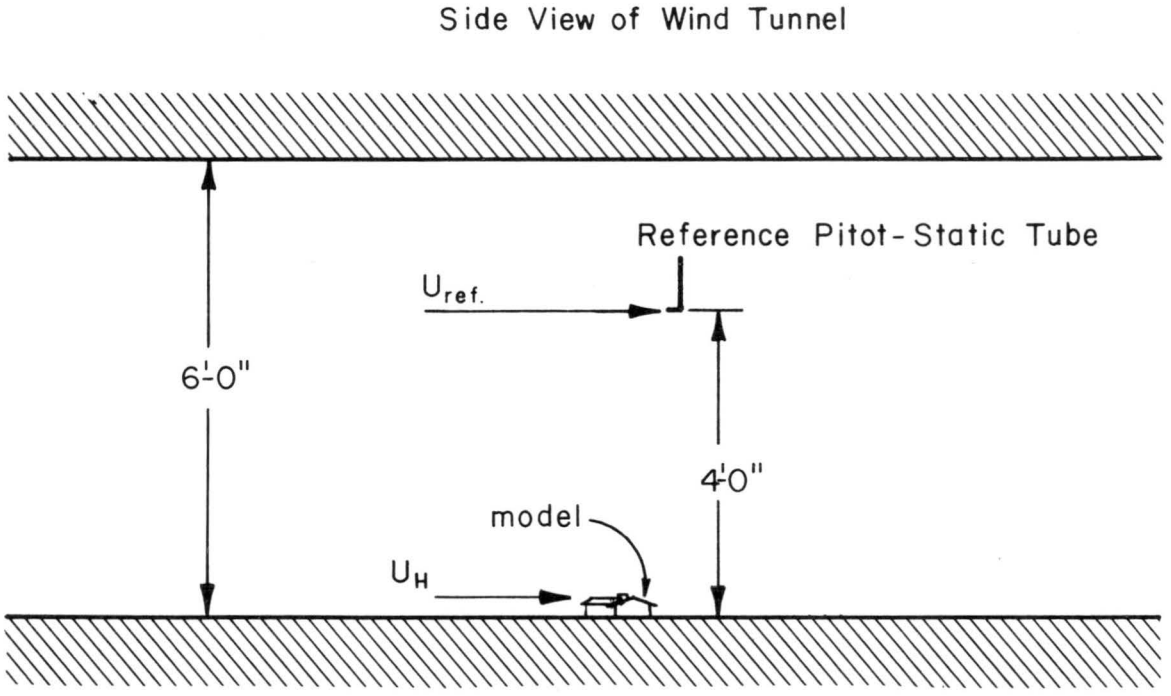

Figure 9. Side view of wind tunnel at model location

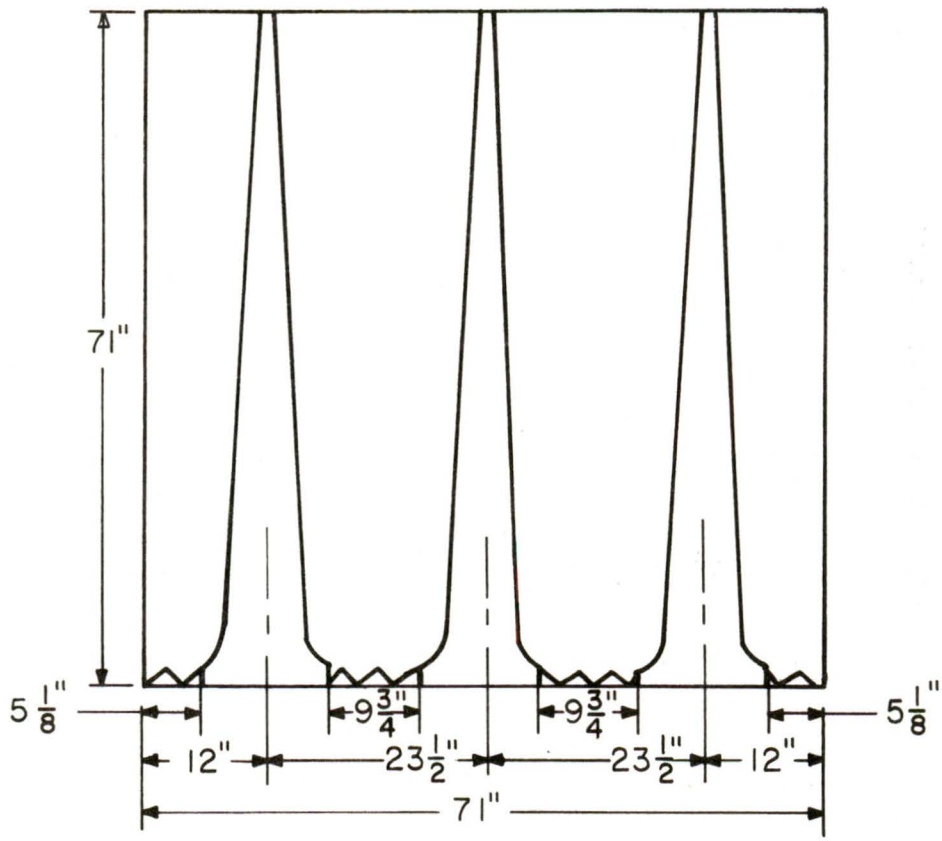

Figure 10. Vortex generators and triangular fence

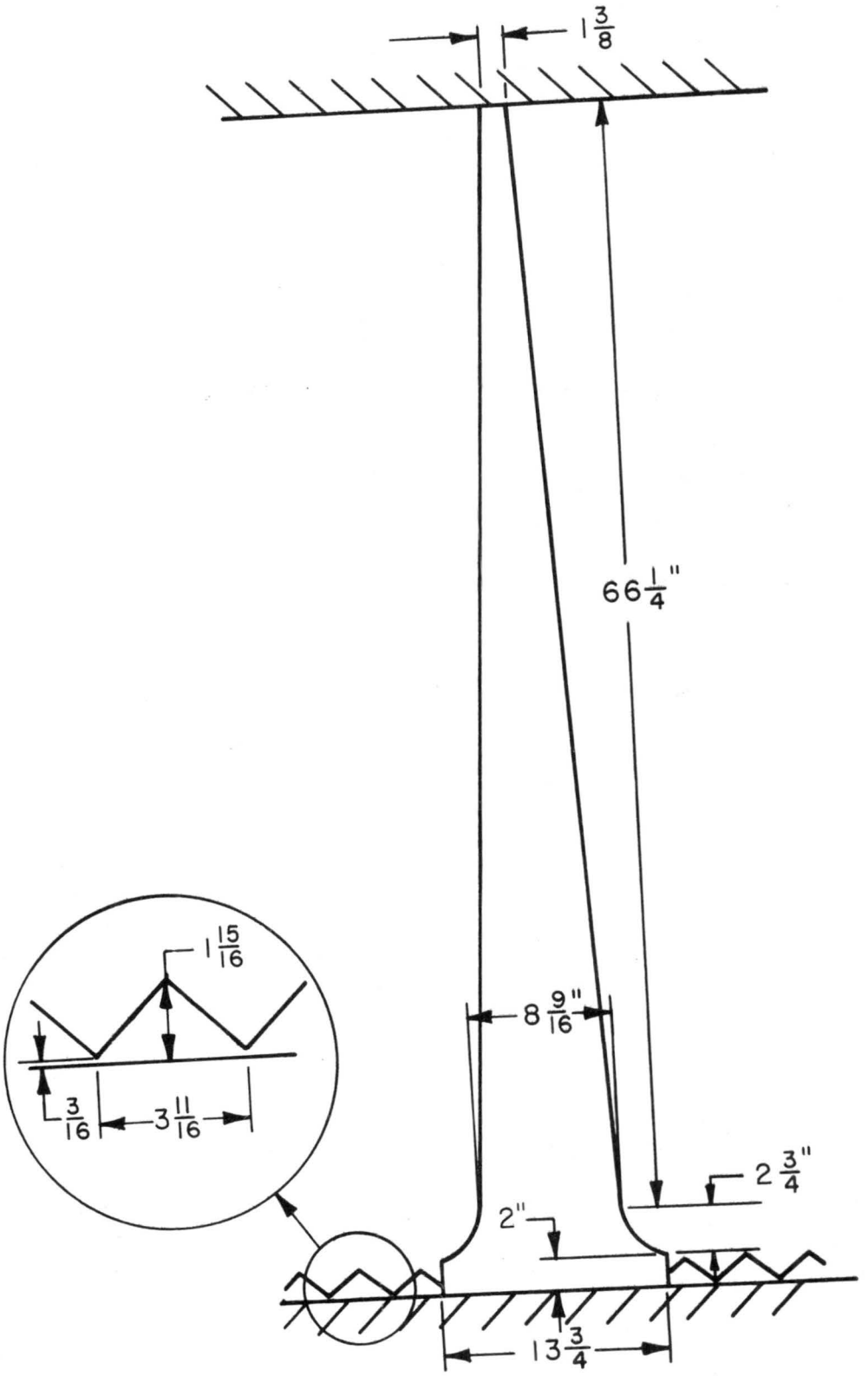

Figure 11. Details of vortex generator

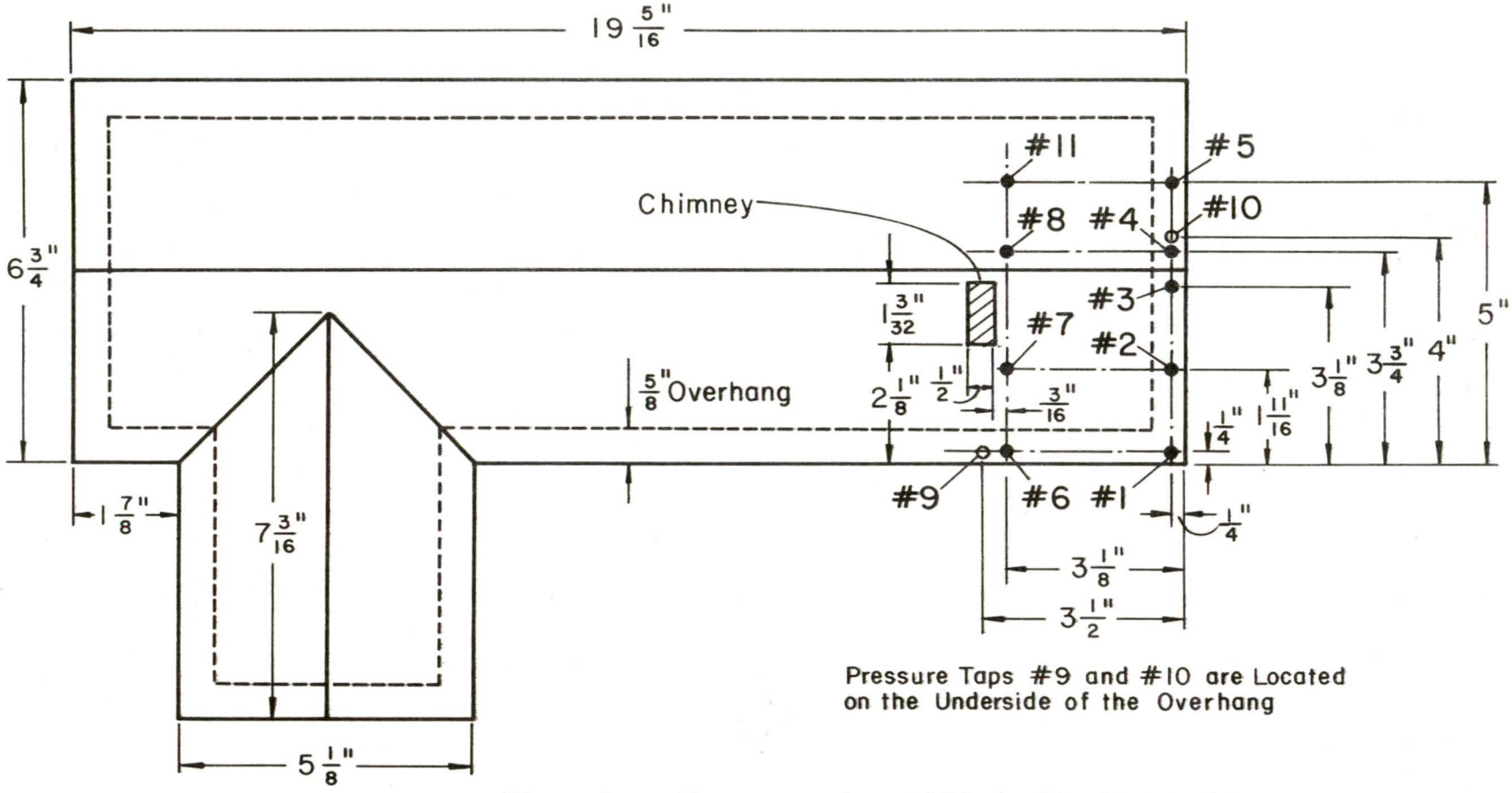

Figure 12. Top view of model house showing location and numbering of pressure taps

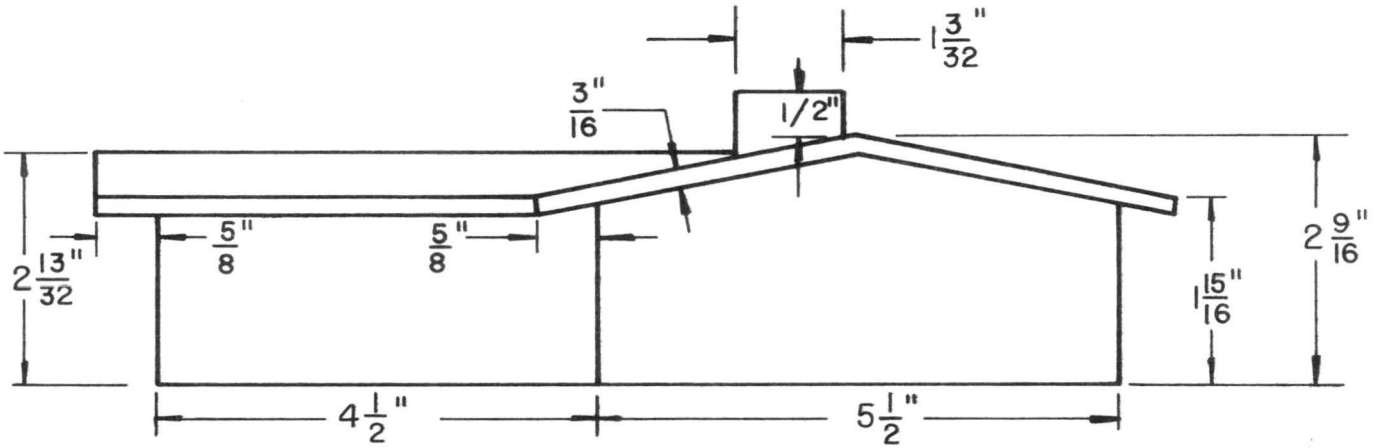

Figure 13. Side view of model house

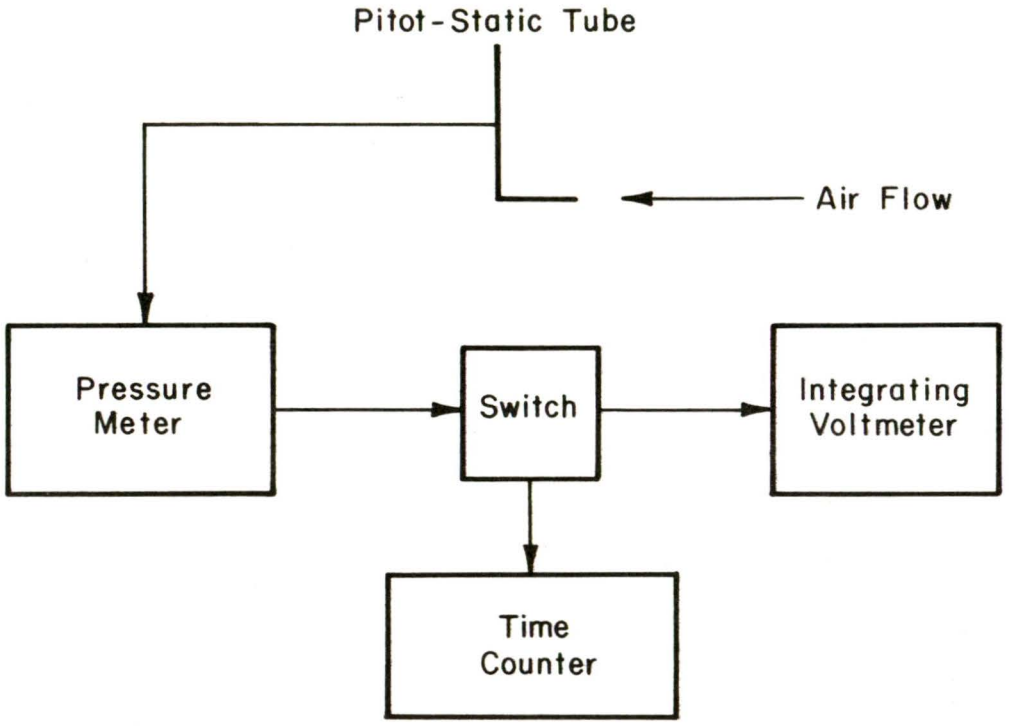

Figure 14. Measurement of mean velocity with pitot-static probe

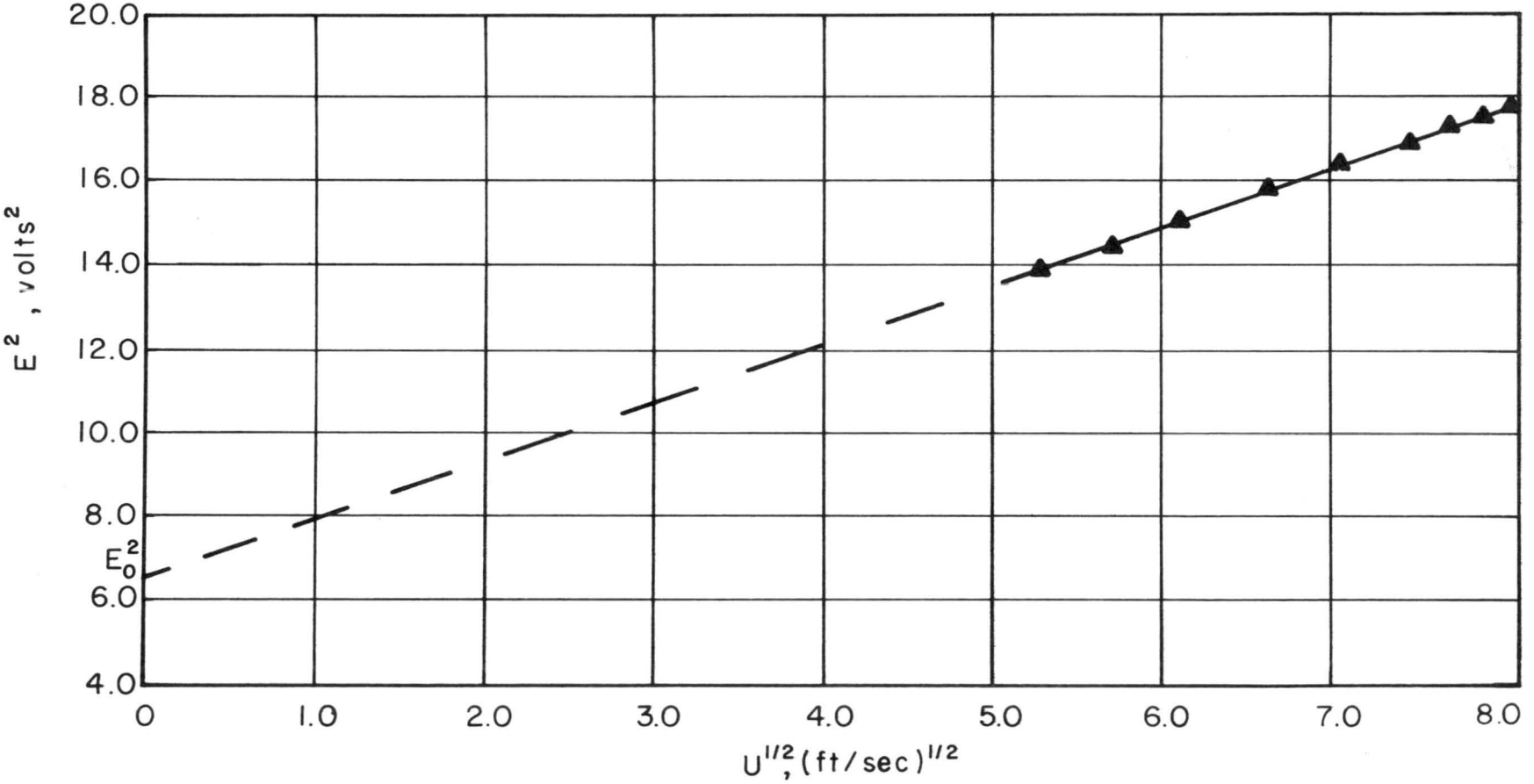

Figure 15. Typical hot-wire calibration curve

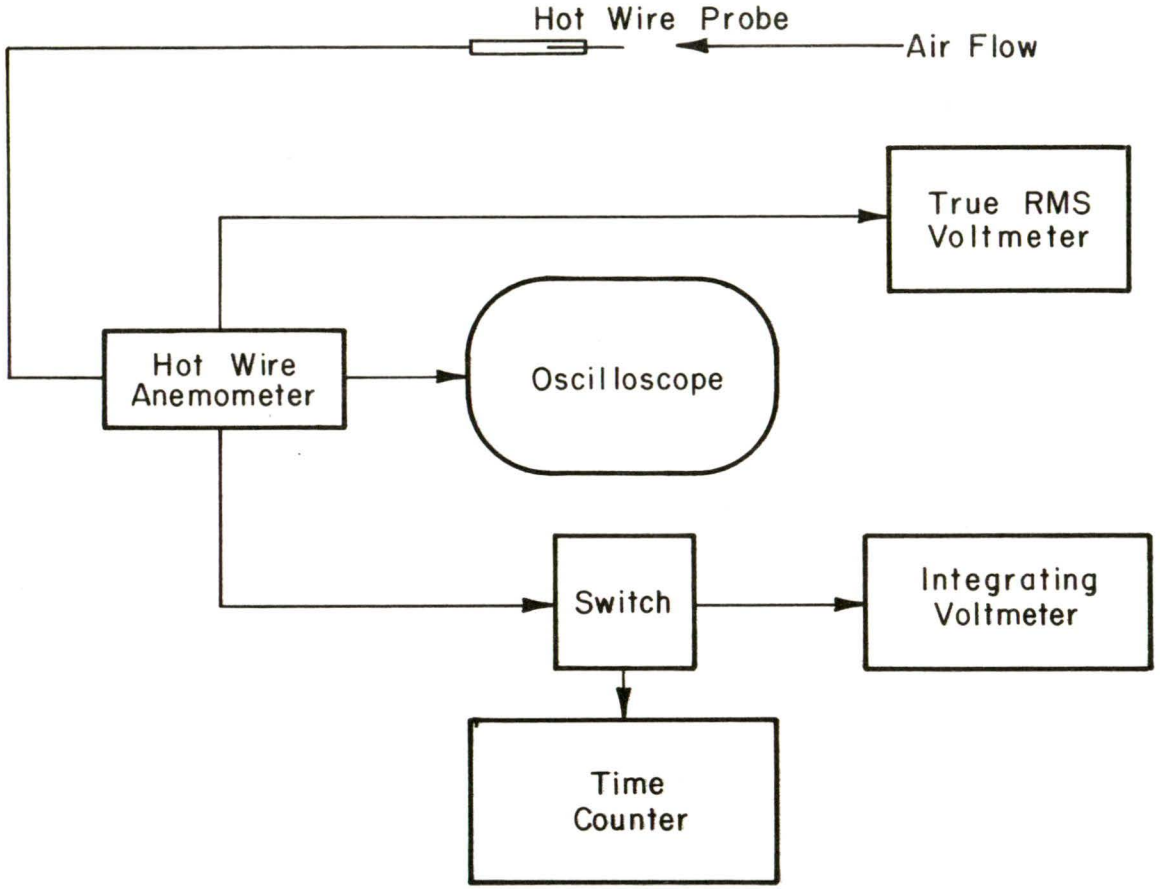

Figure 16. Velocity and turbulence measurements with hot-wire anemometer

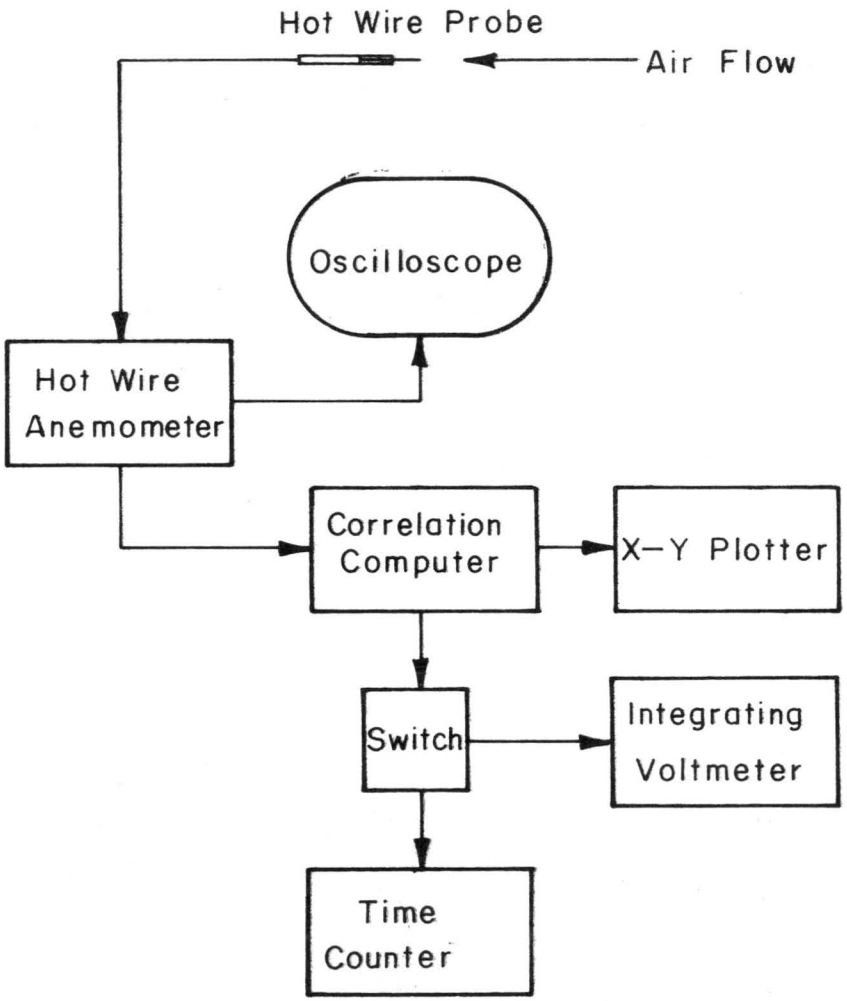

Figure 17. Measurement of integral longitudinal turbulence scale

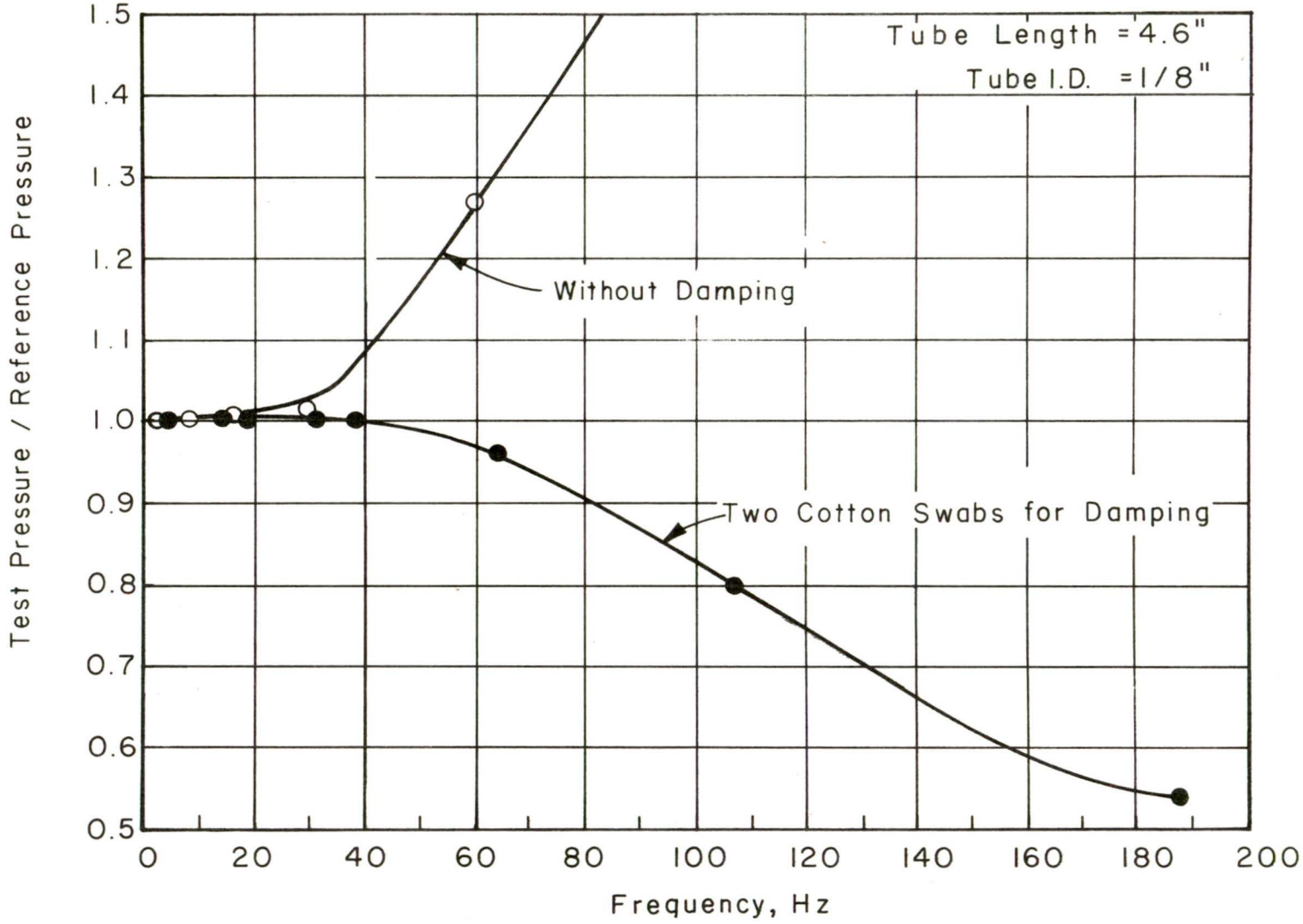

Figure 18. Frequency response of pressure measuring system with Validyne transducers (Courtesy of National Bureau of Standards Center for Building Technology)

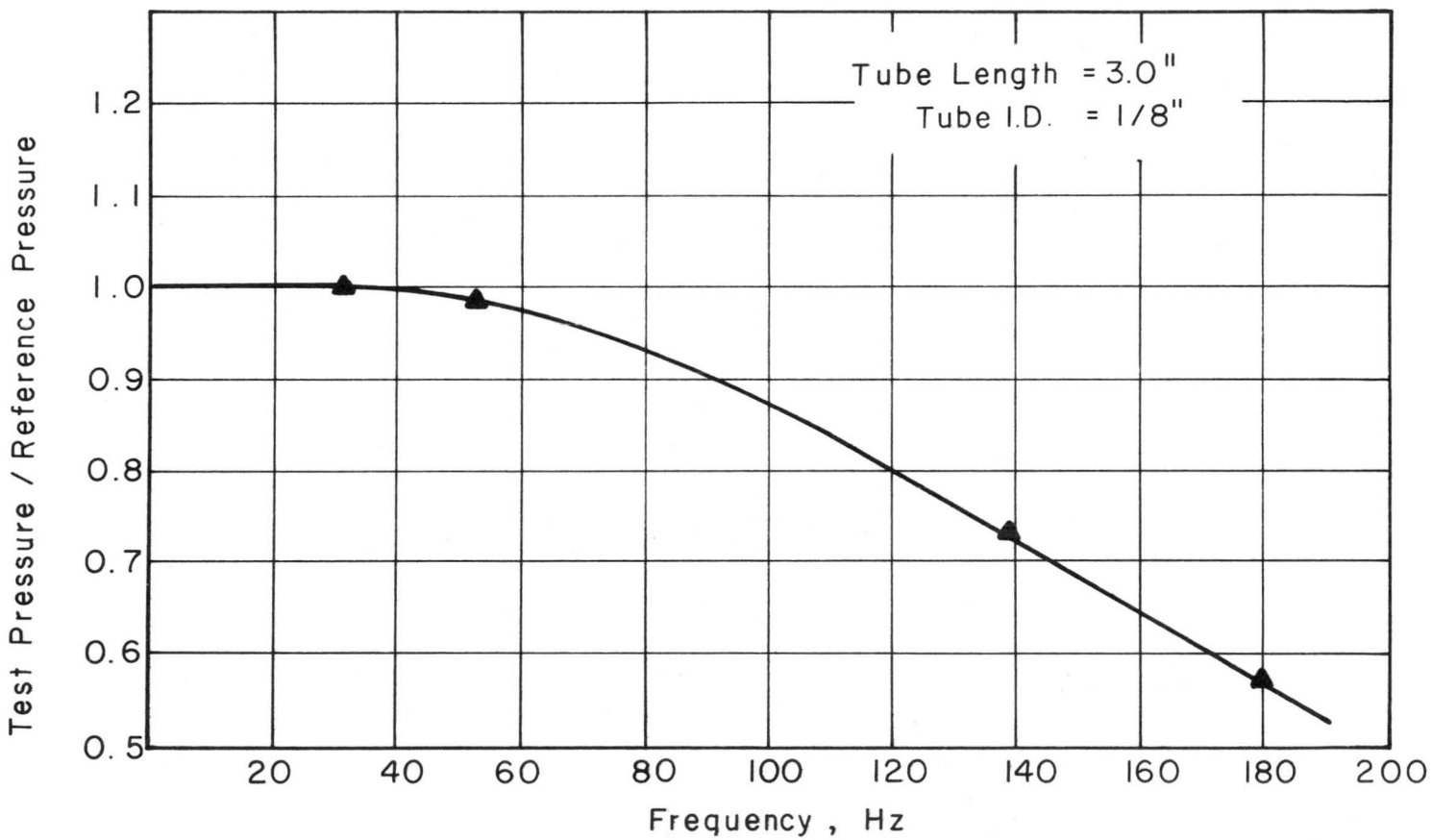

Figure 19. Frequency response of pressure measuring system with Statham transducer (Ref. 10)

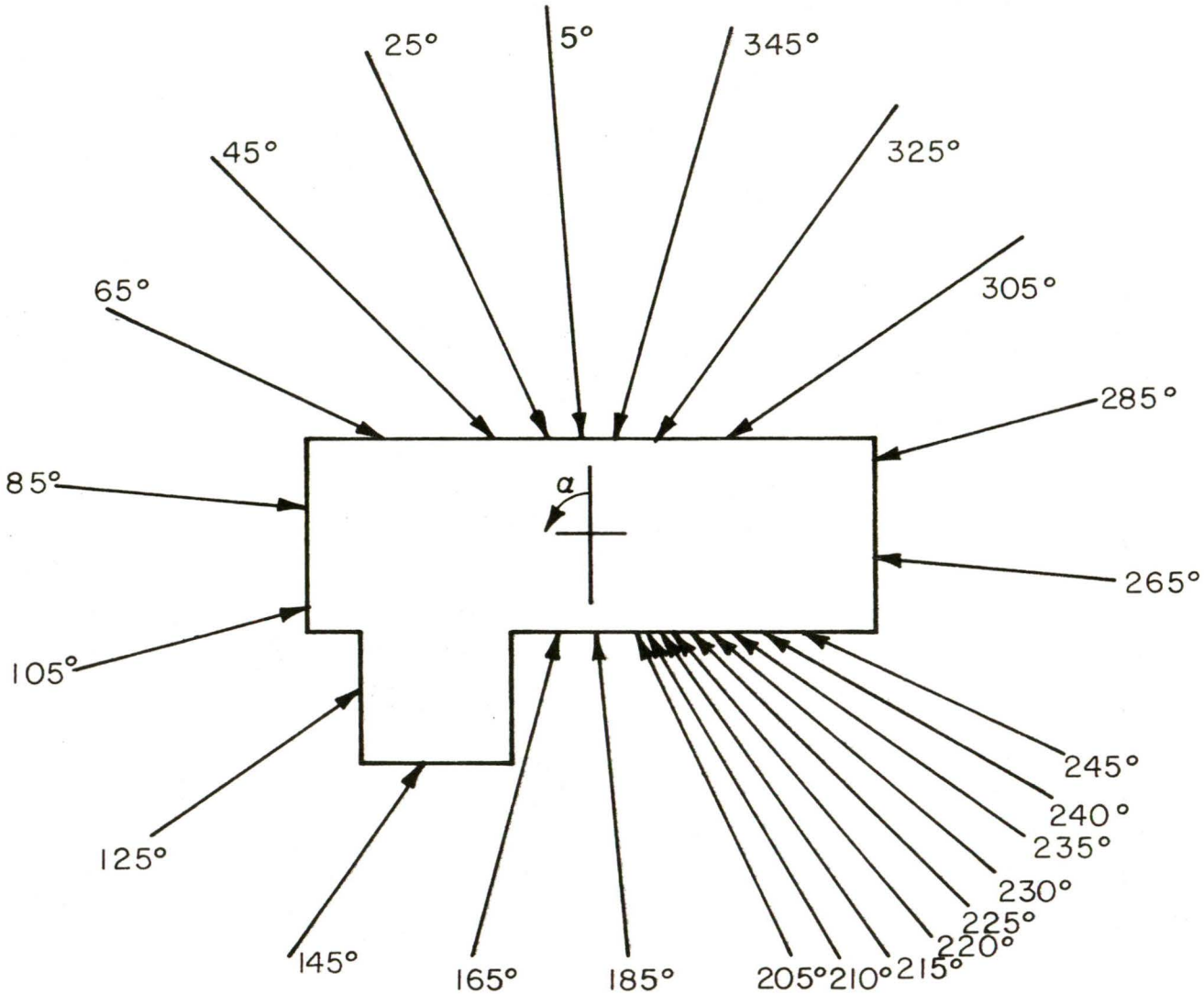

Figure 20. Simulated wind directions

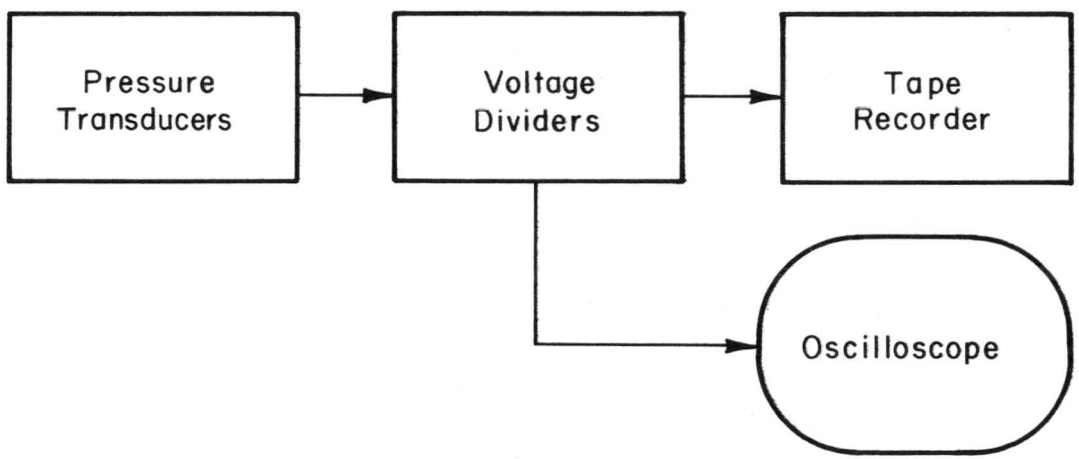

Figure 21. Recording of pressure transducer signals

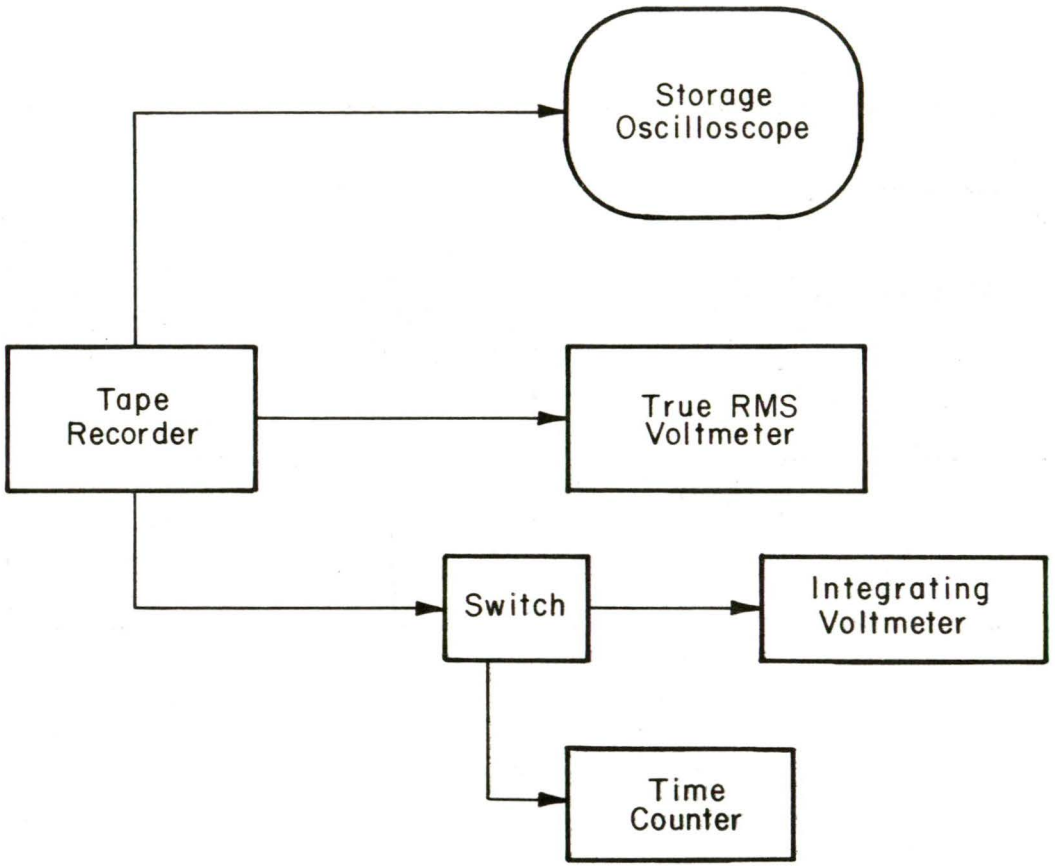

Figure 22. Instrumentation for determining mean, fluctuating, and peak pressures

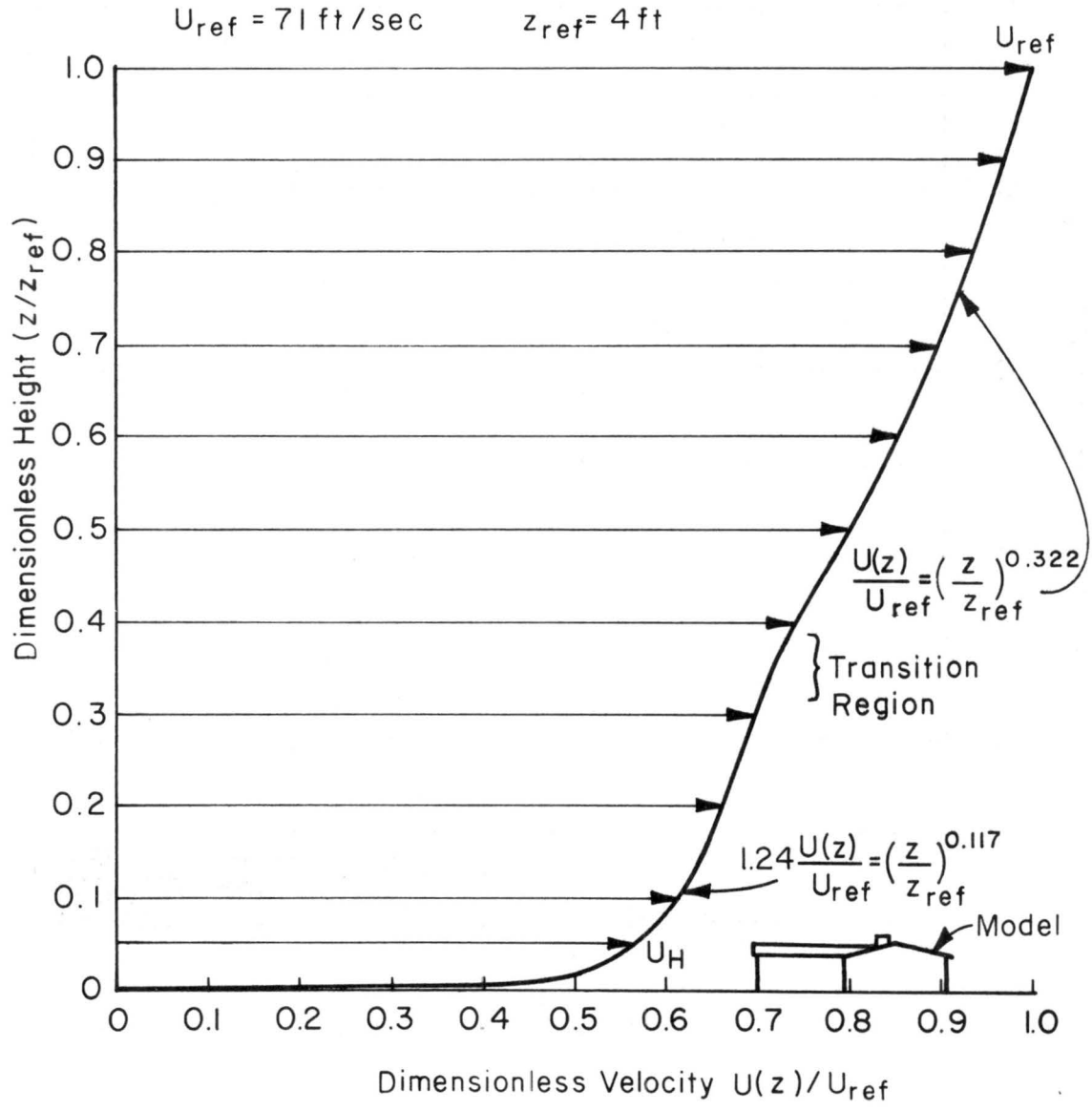

Figure 23. Mean velocity profile for wind-tunnel simulated flow

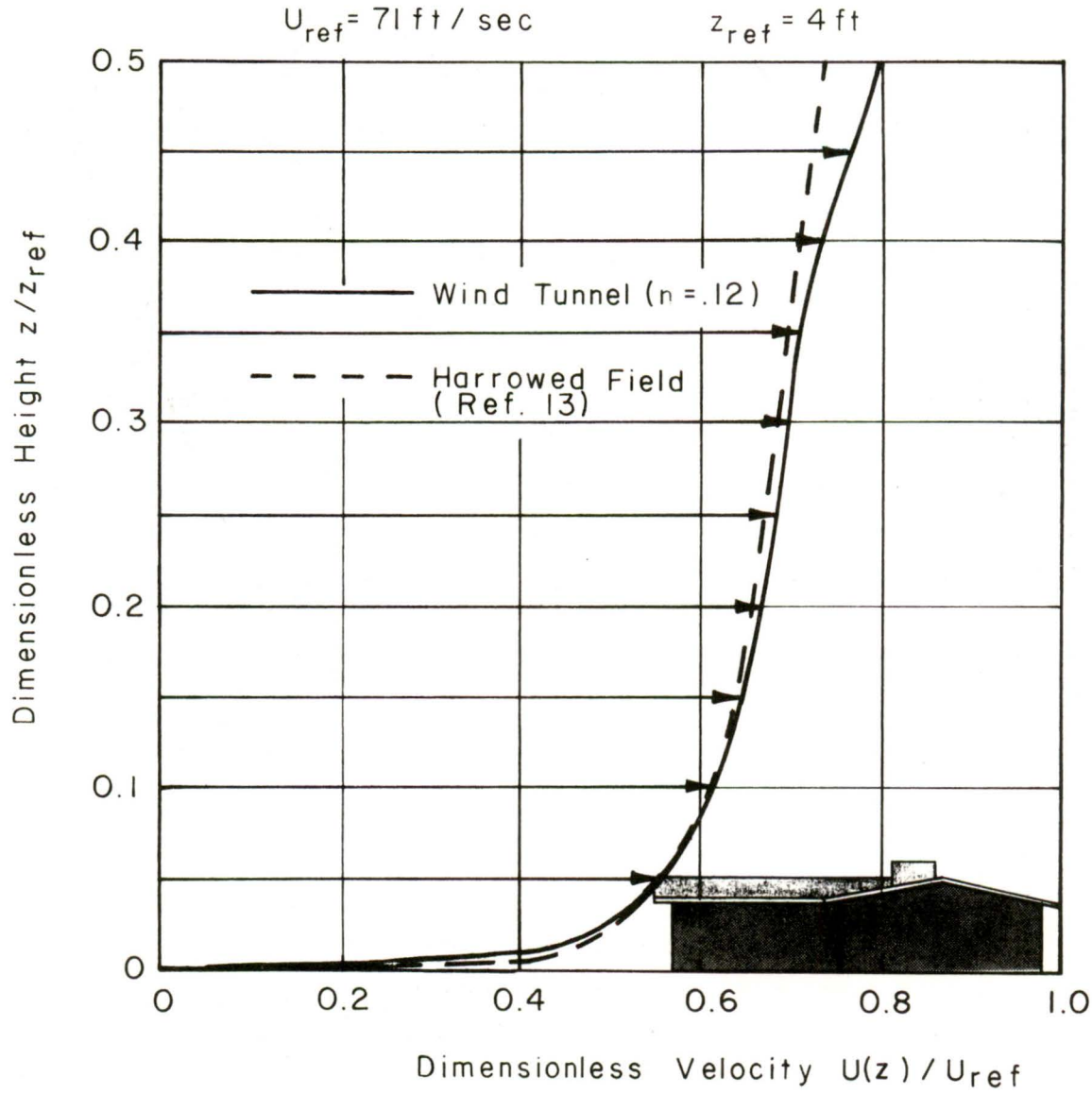

Figure 24. Comparison between wind-tunnel and prototype velocity profiles

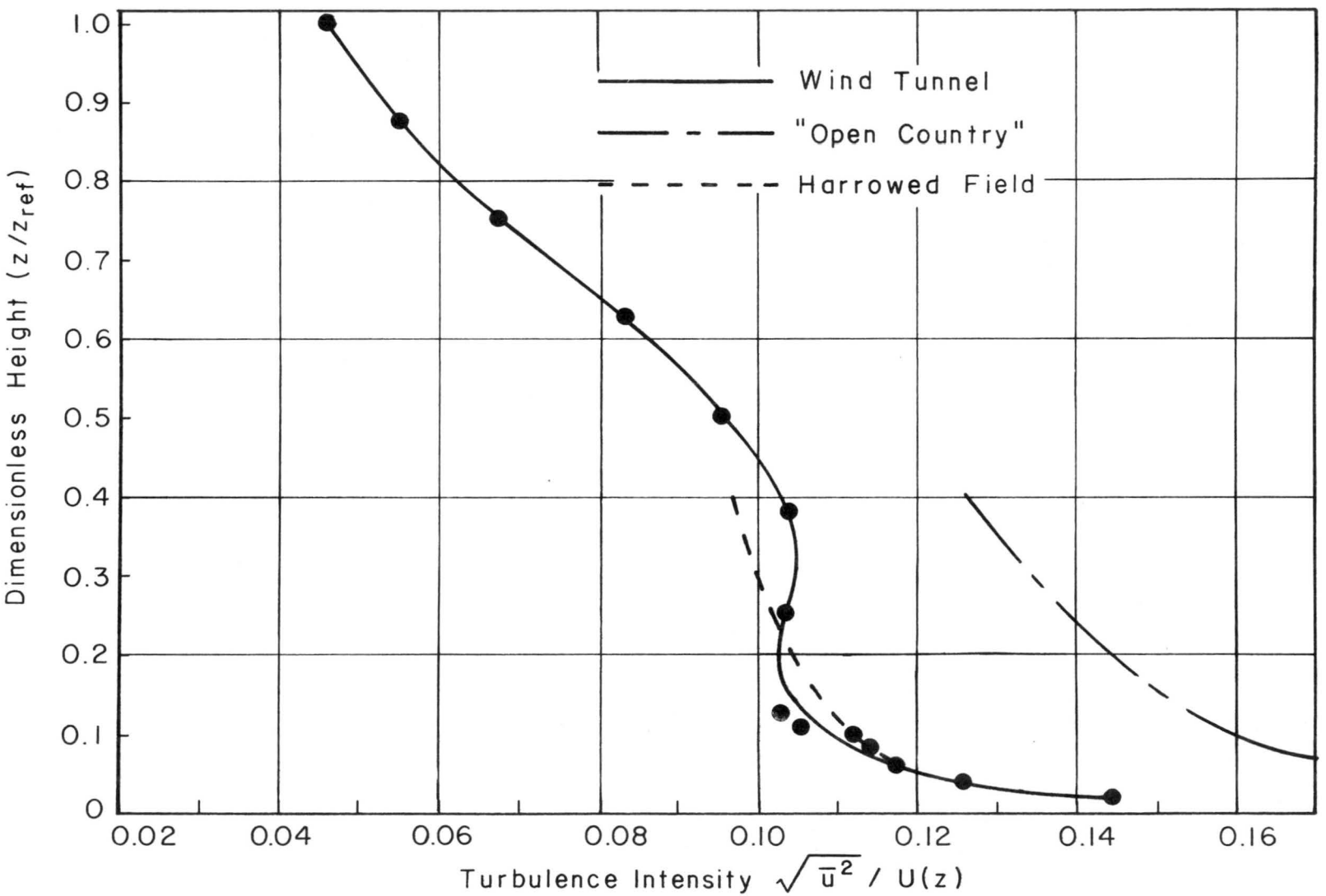

Figure 25. Longitudinal turbulence intensities for wind-tunnel and prototype flows

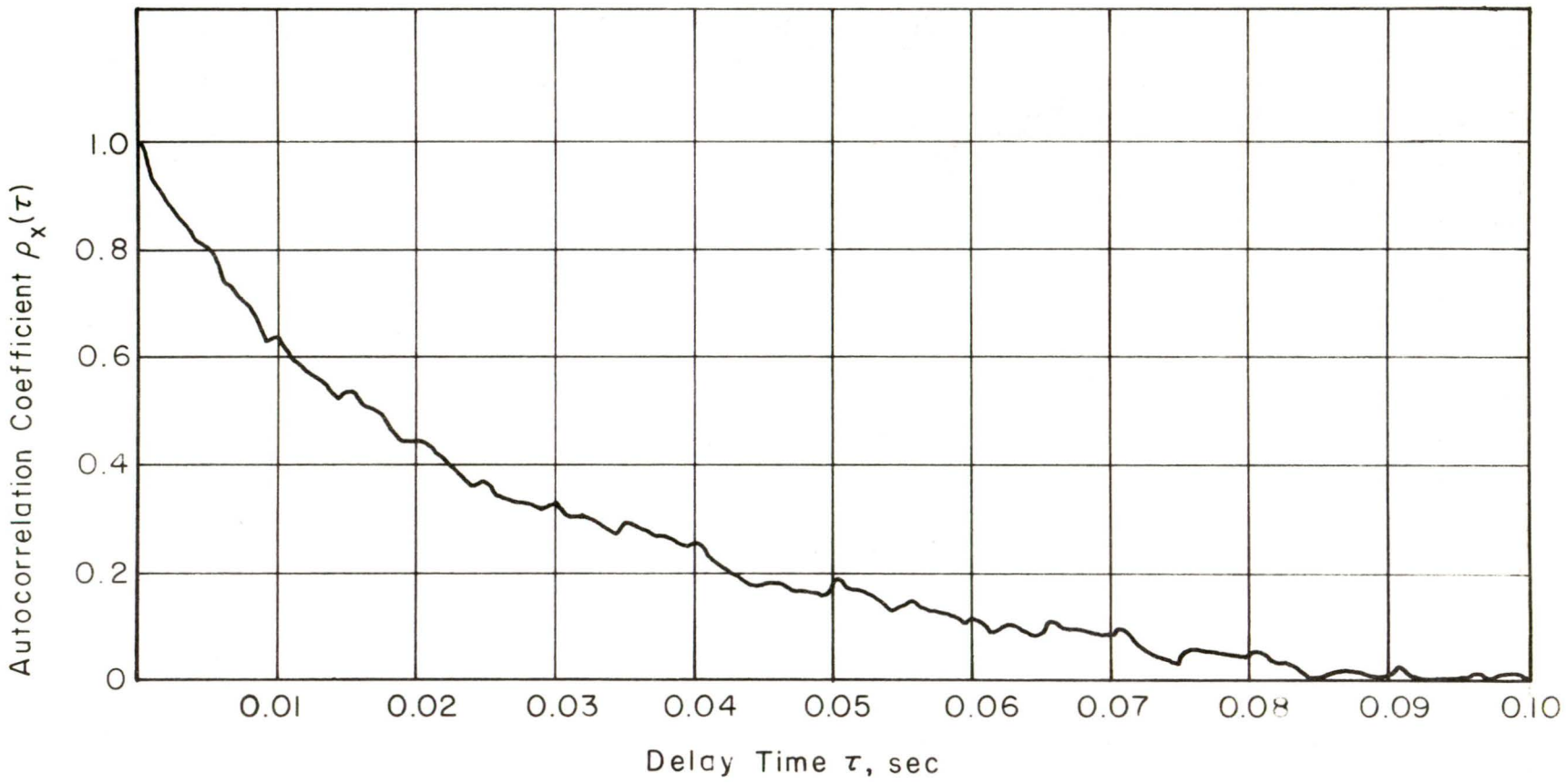

Figure 26. Autocorrelation of longitudinal velocity fluctuations at 5-1/4 in. above wind-tunnel floor

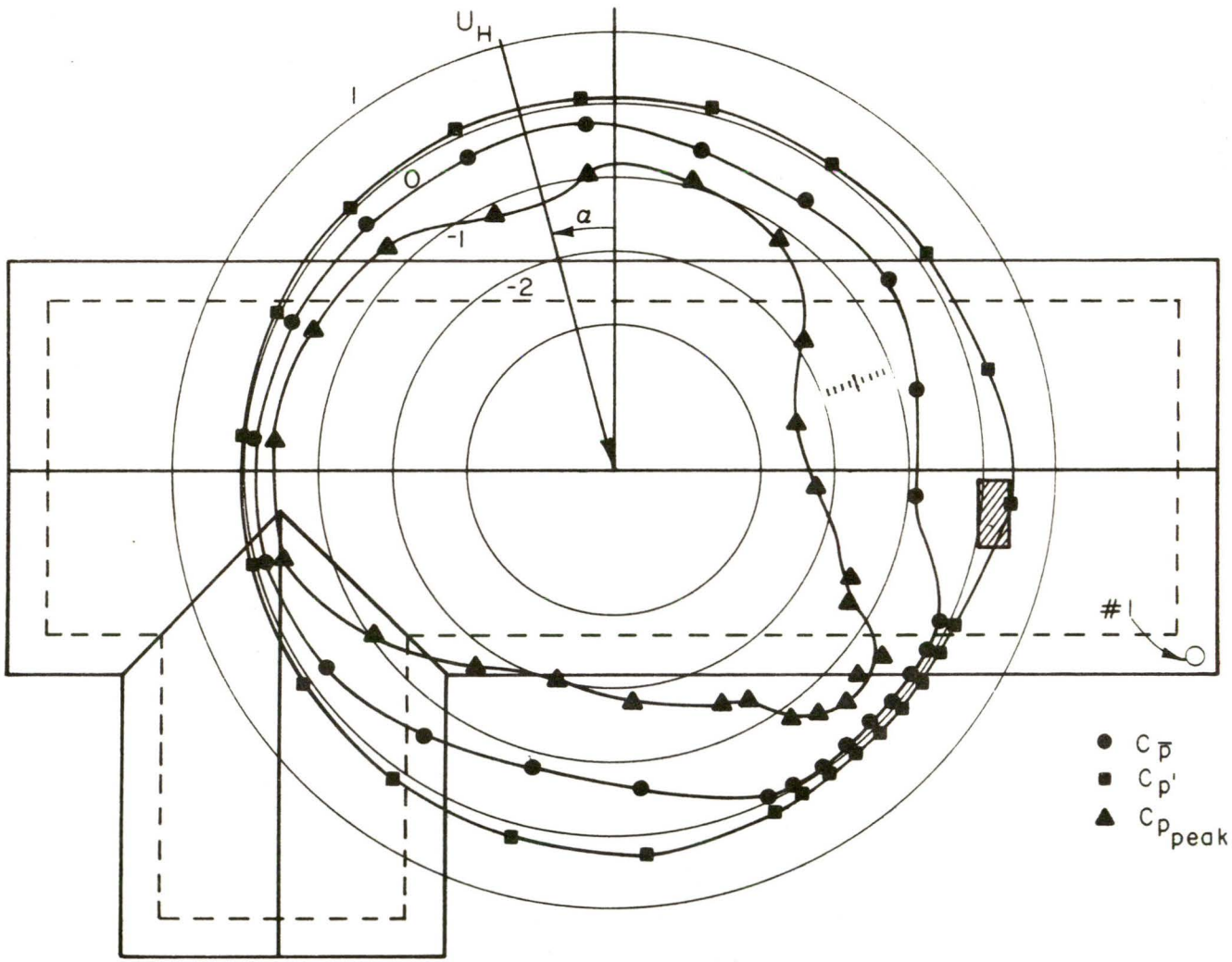

Figure 27. Variation of roof pressure at pressure tap #1

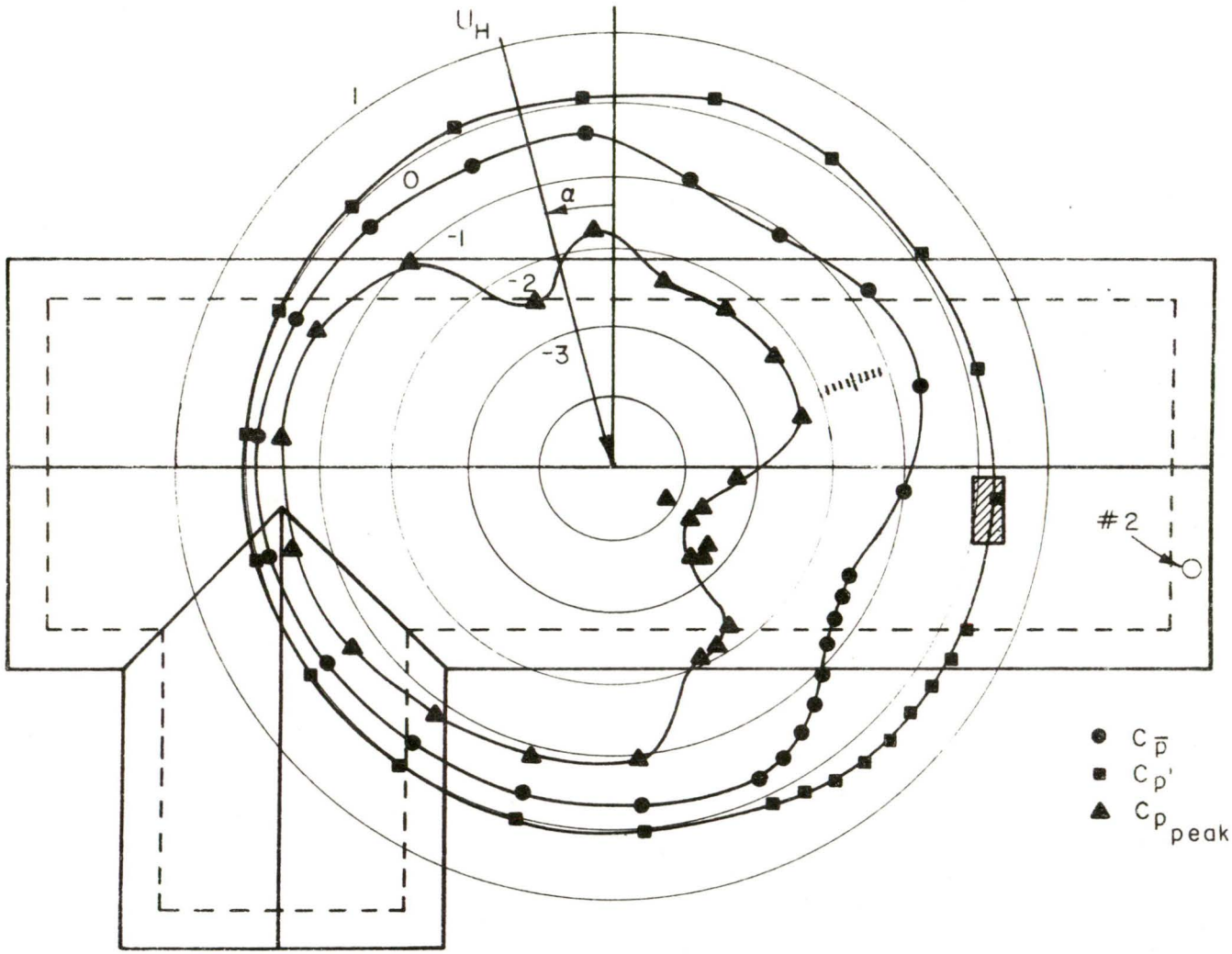

Figure 28. Variation of roof pressure at pressure tap #2

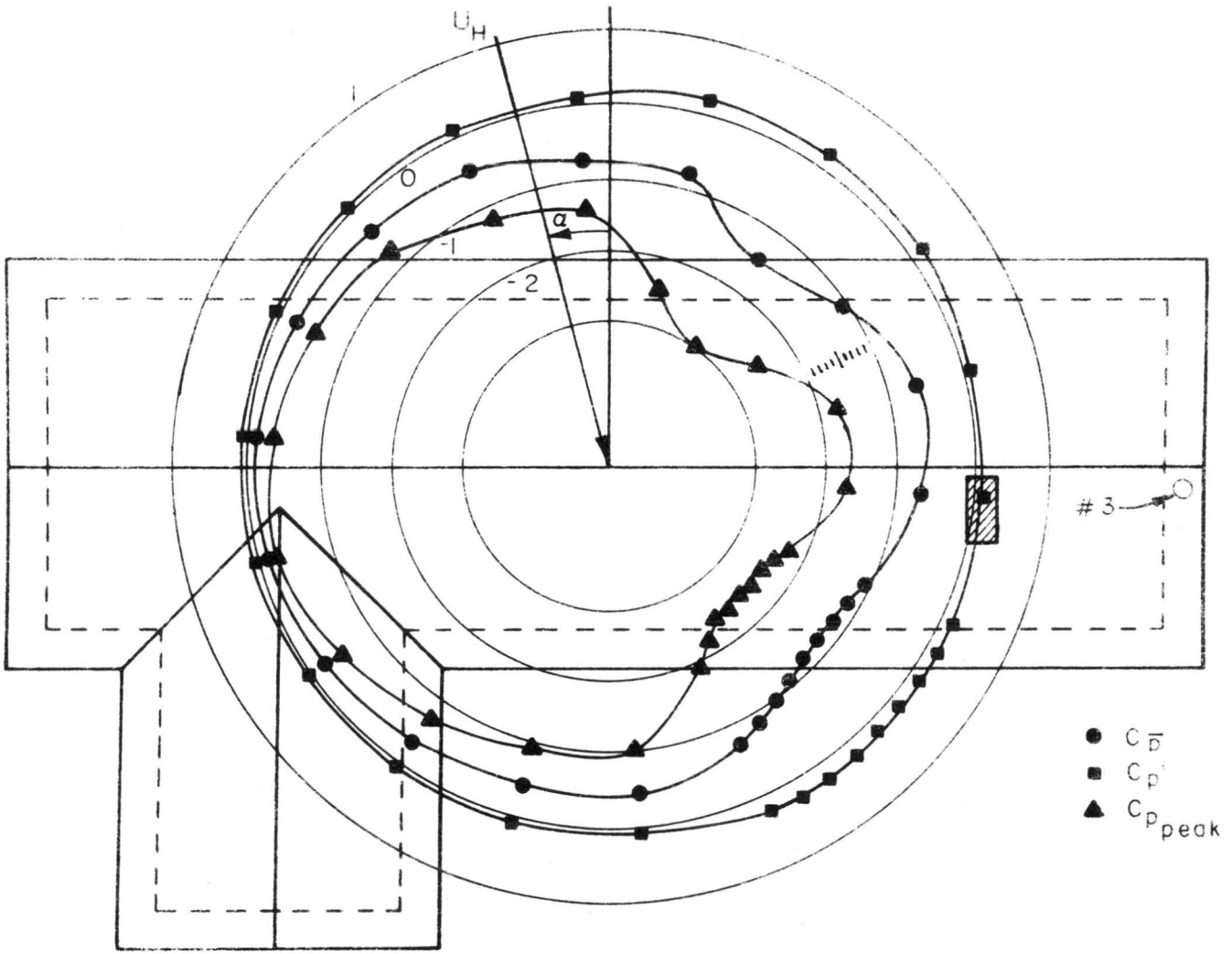

Figure 29. Variation of roof pressure at pressure tap #3

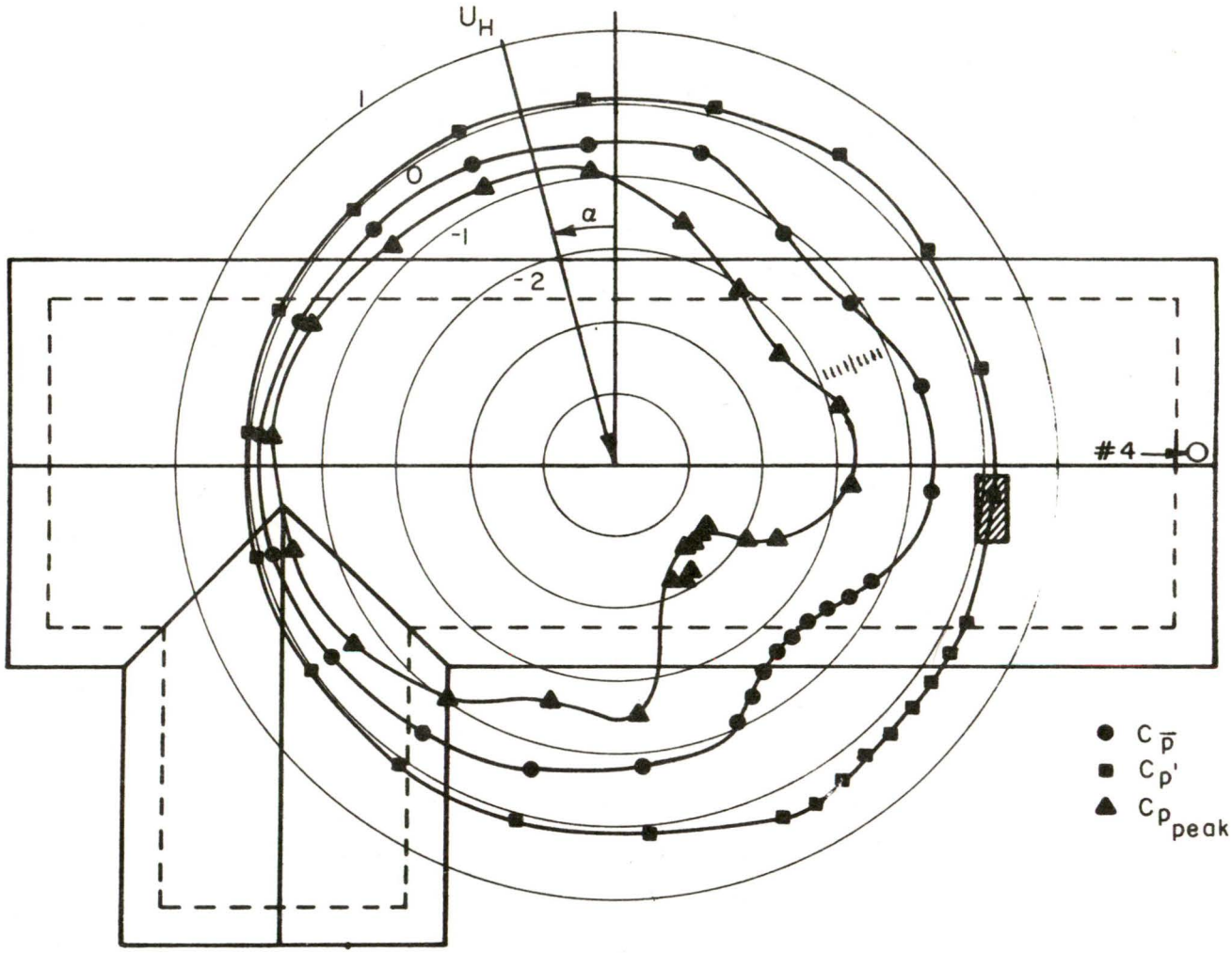

Figure 30. Variation of roof pressure at pressure tap #4

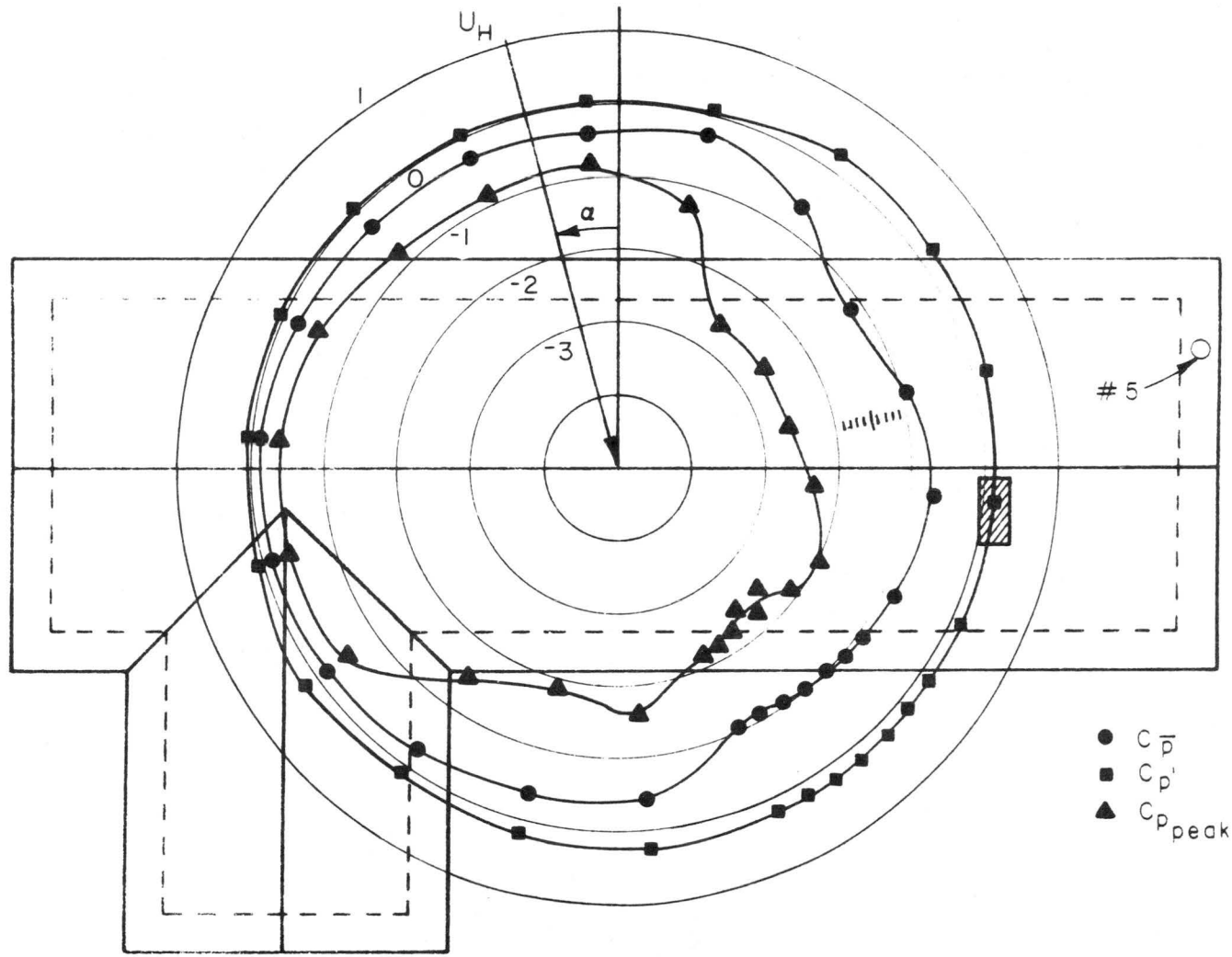

Figure 31. Variation of roof pressure at pressure tap #5

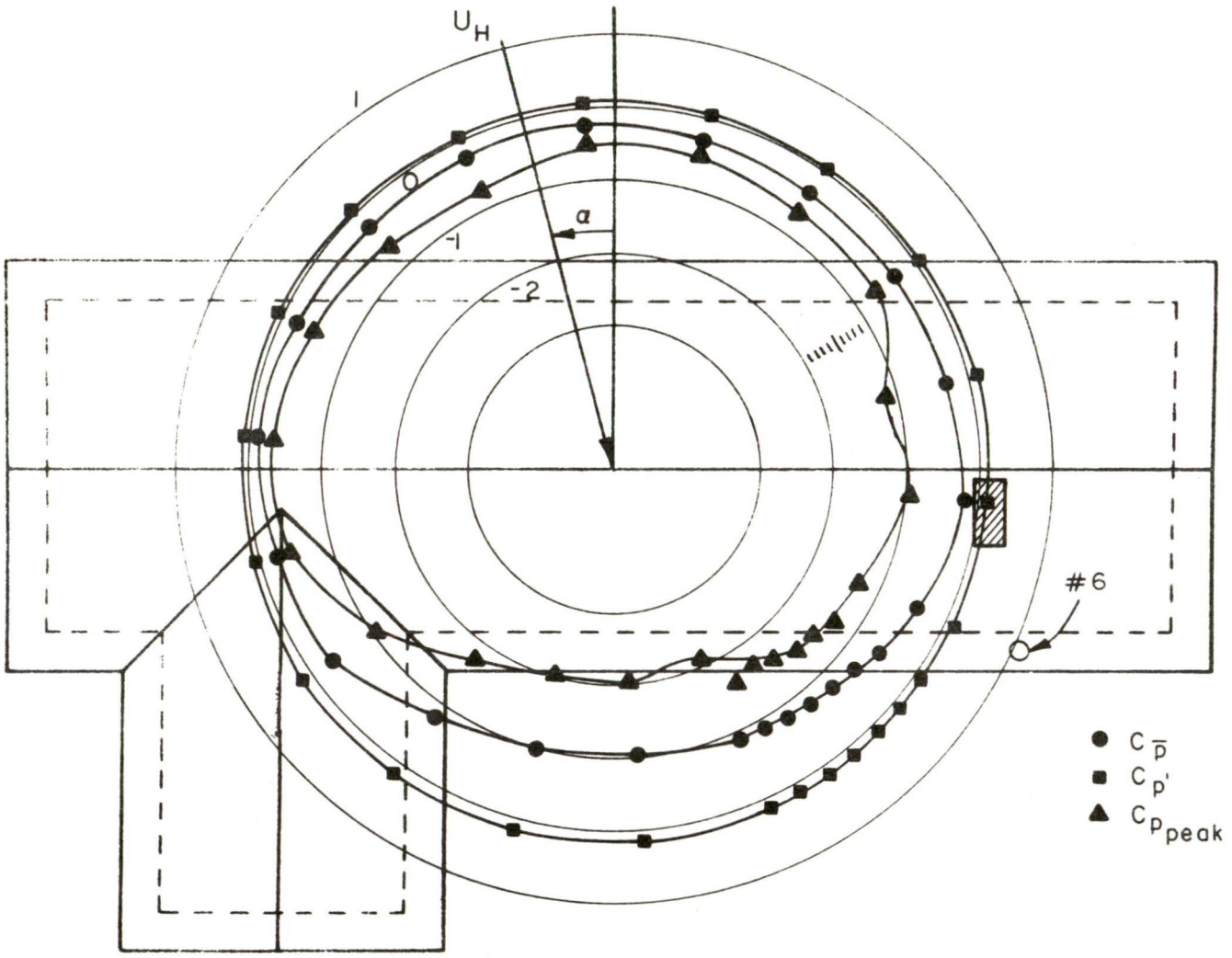

Figure 32. Variation of roof pressure at pressure tap #6

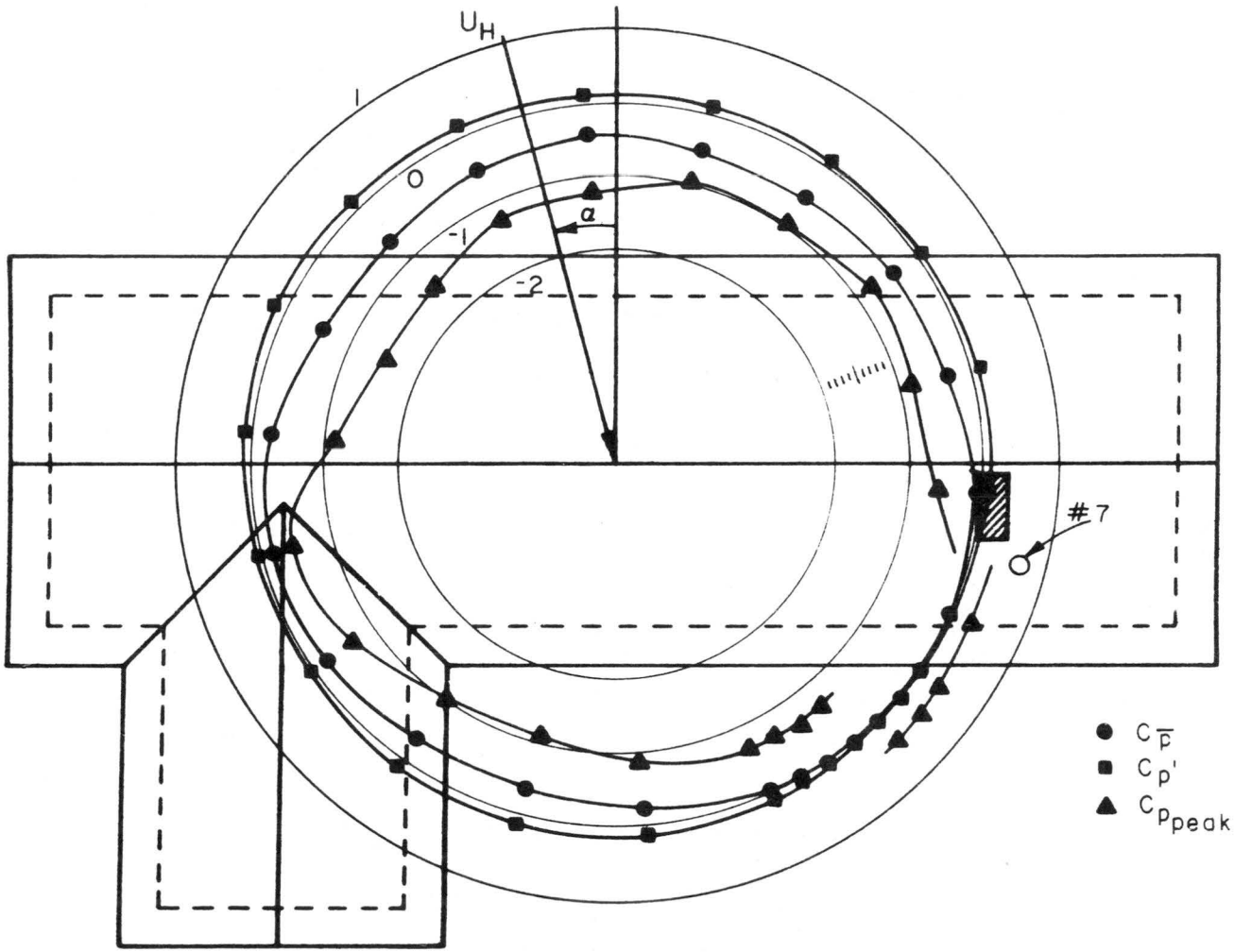

Figure 33. Variation of roof pressure at pressure tap #7

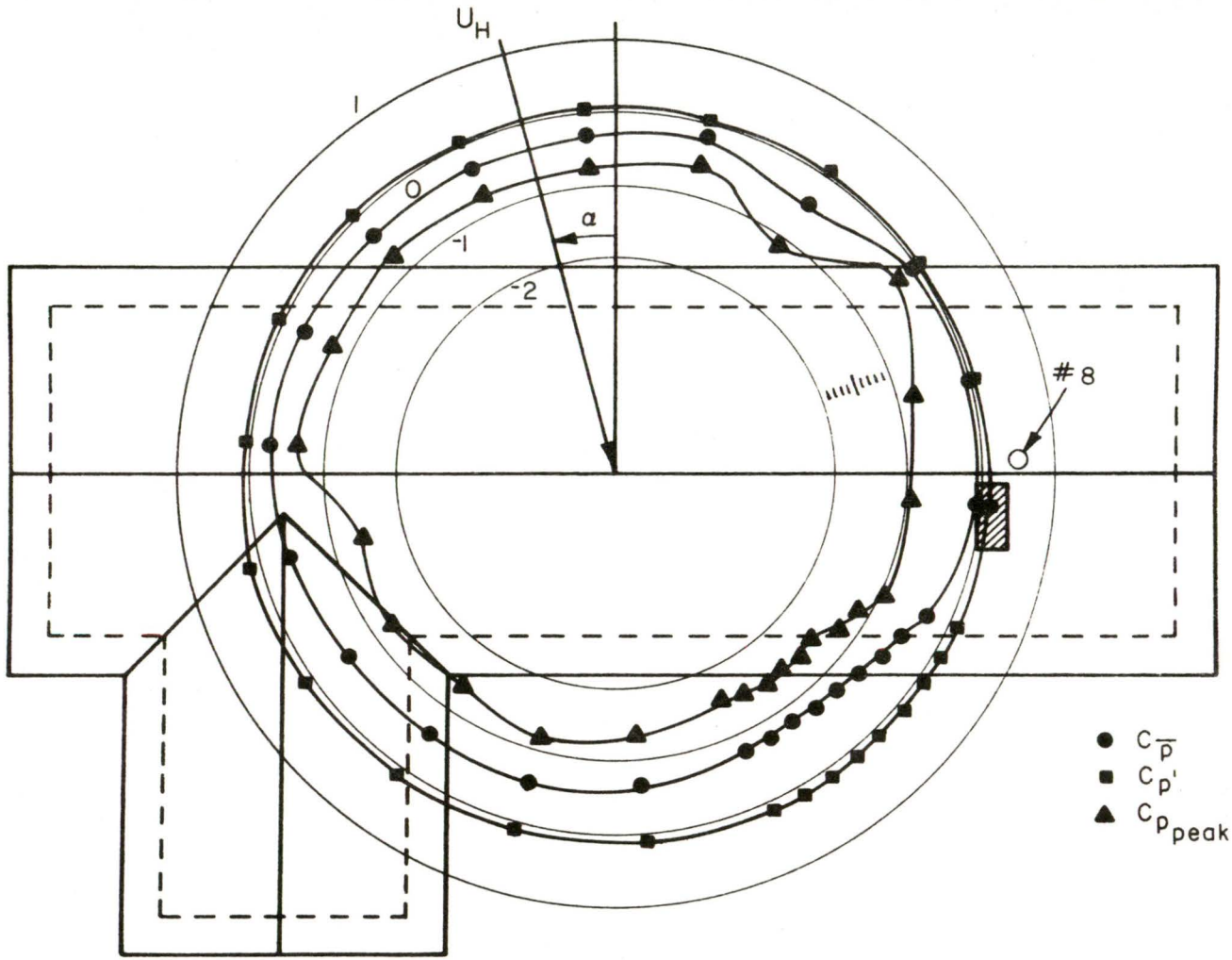

Figure 34. Variation of roof pressure at pressure tap #8

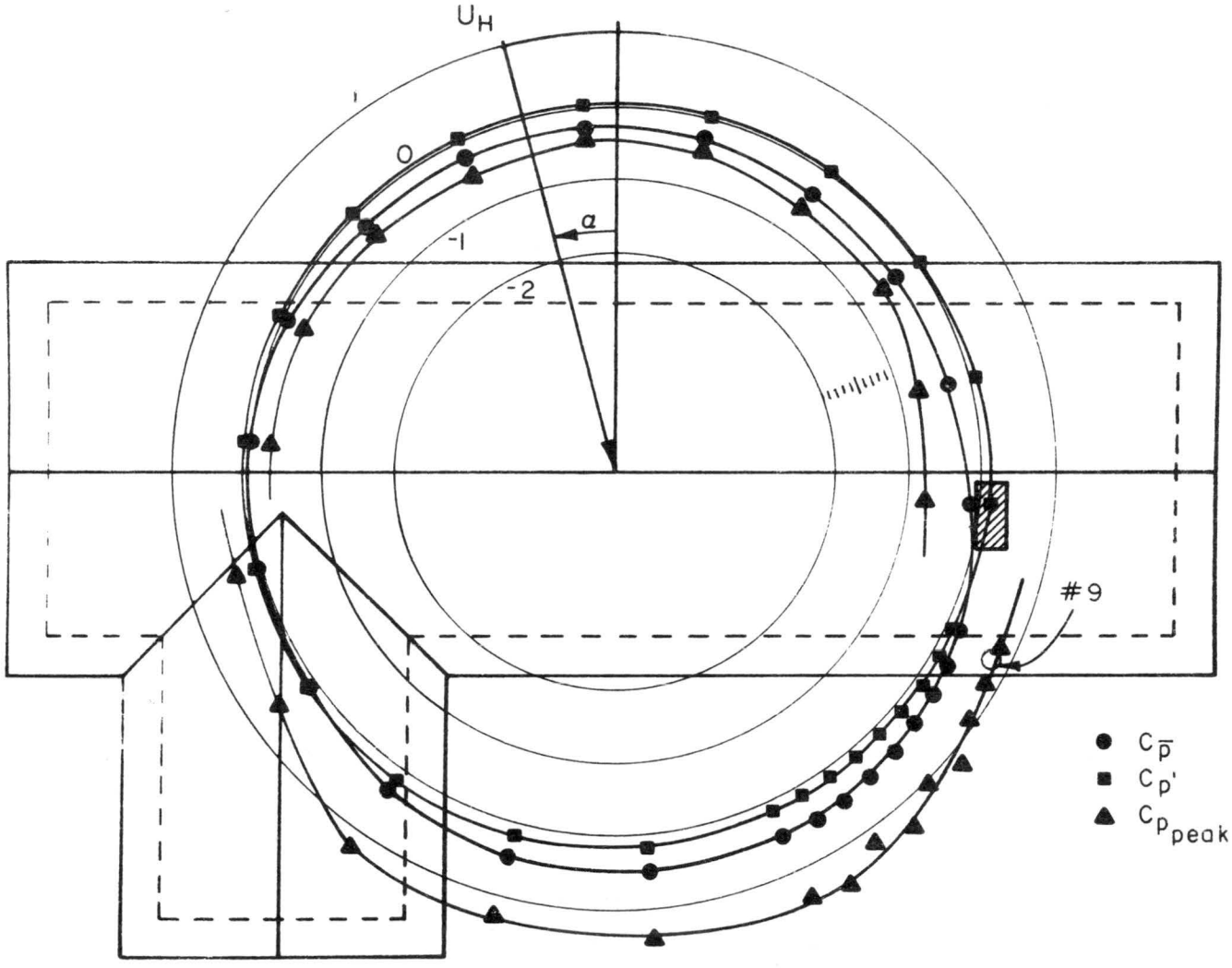

Figure 35. Variation of roof pressure at pressure tap #9 (underneath overhang)

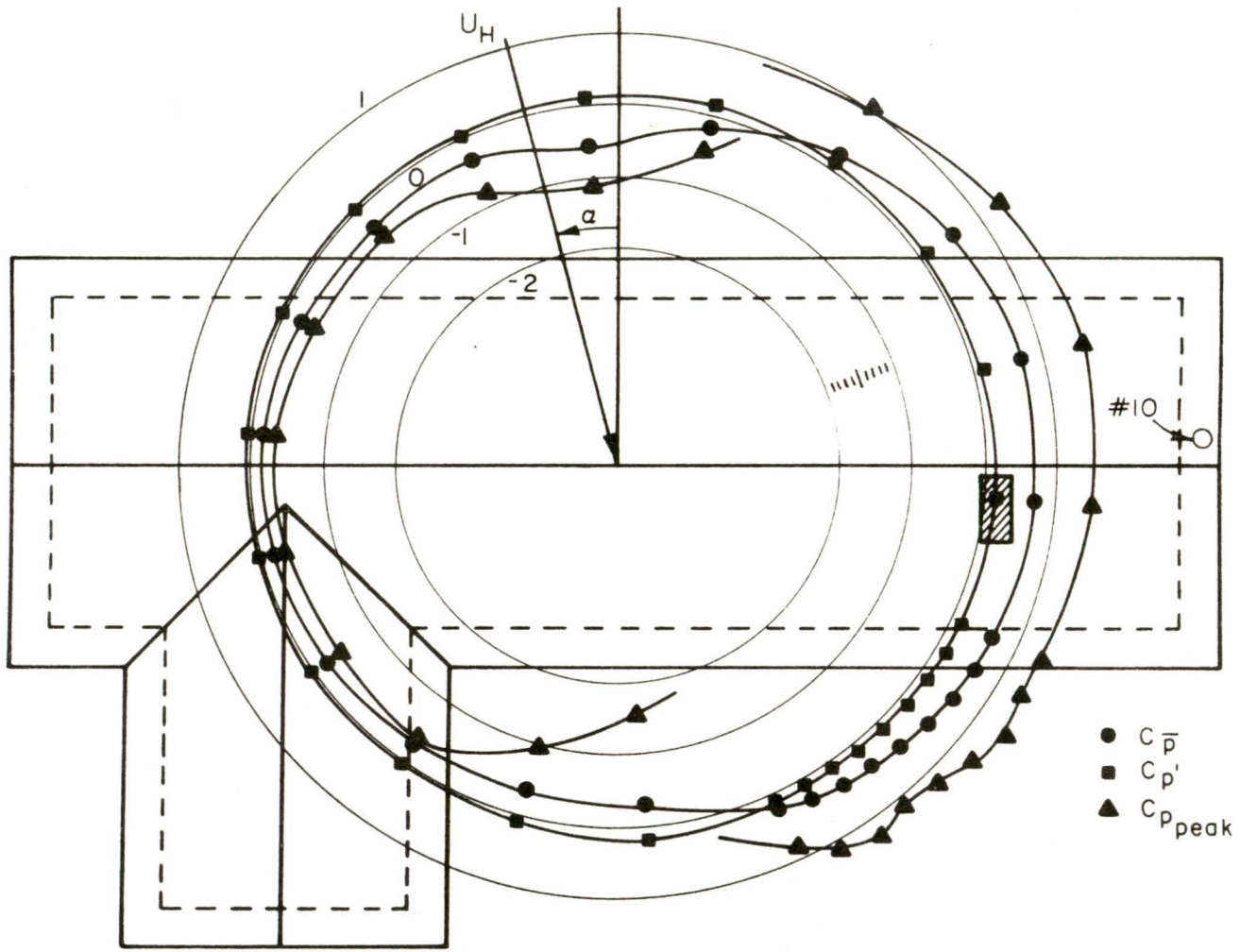

Figure 36. Variation of roof pressure at pressure tap #10 (underneath overhang)

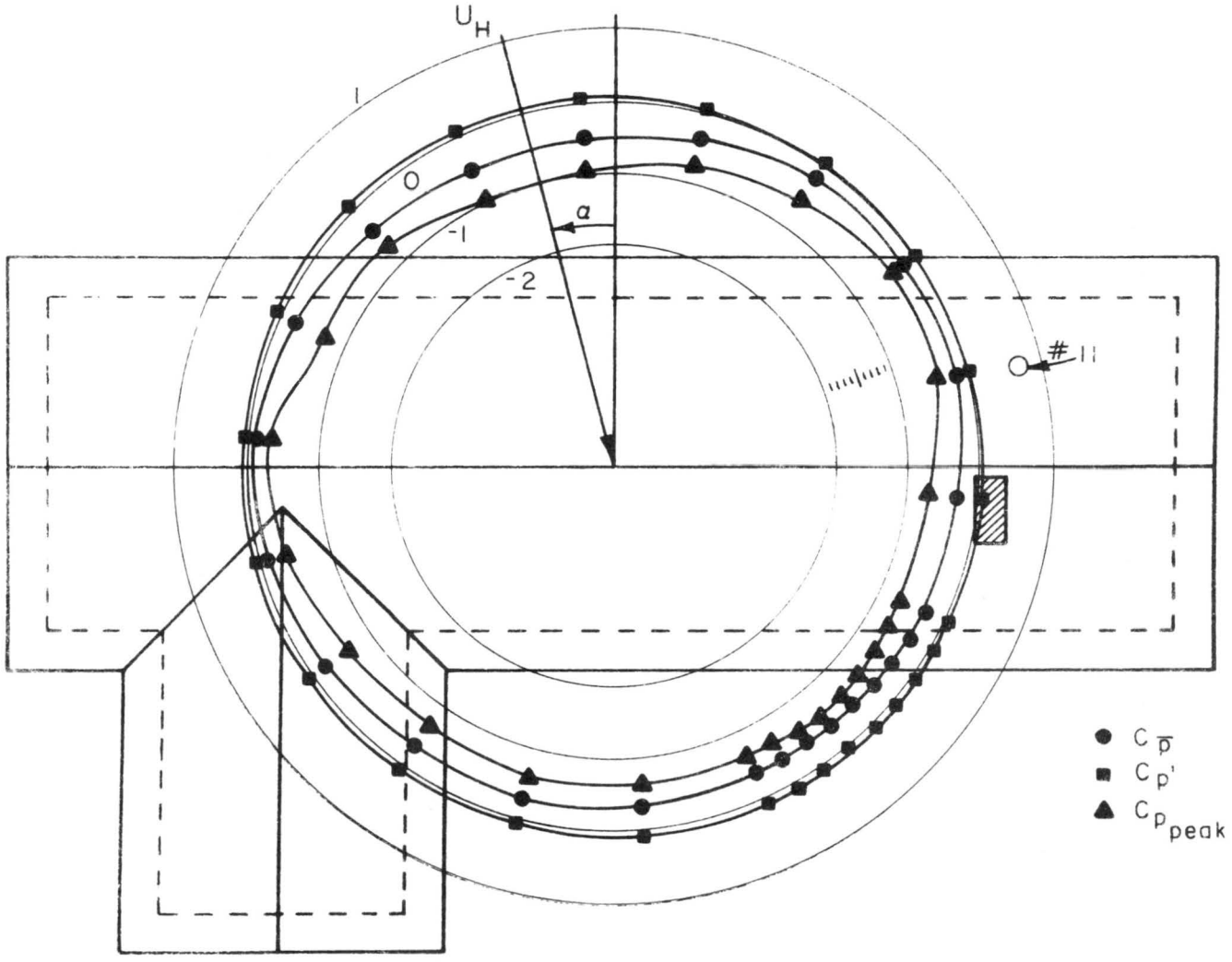

Figure 37. Variation of roof pressure at pressure tap #11 (low-pass filtered at 25 Hz)

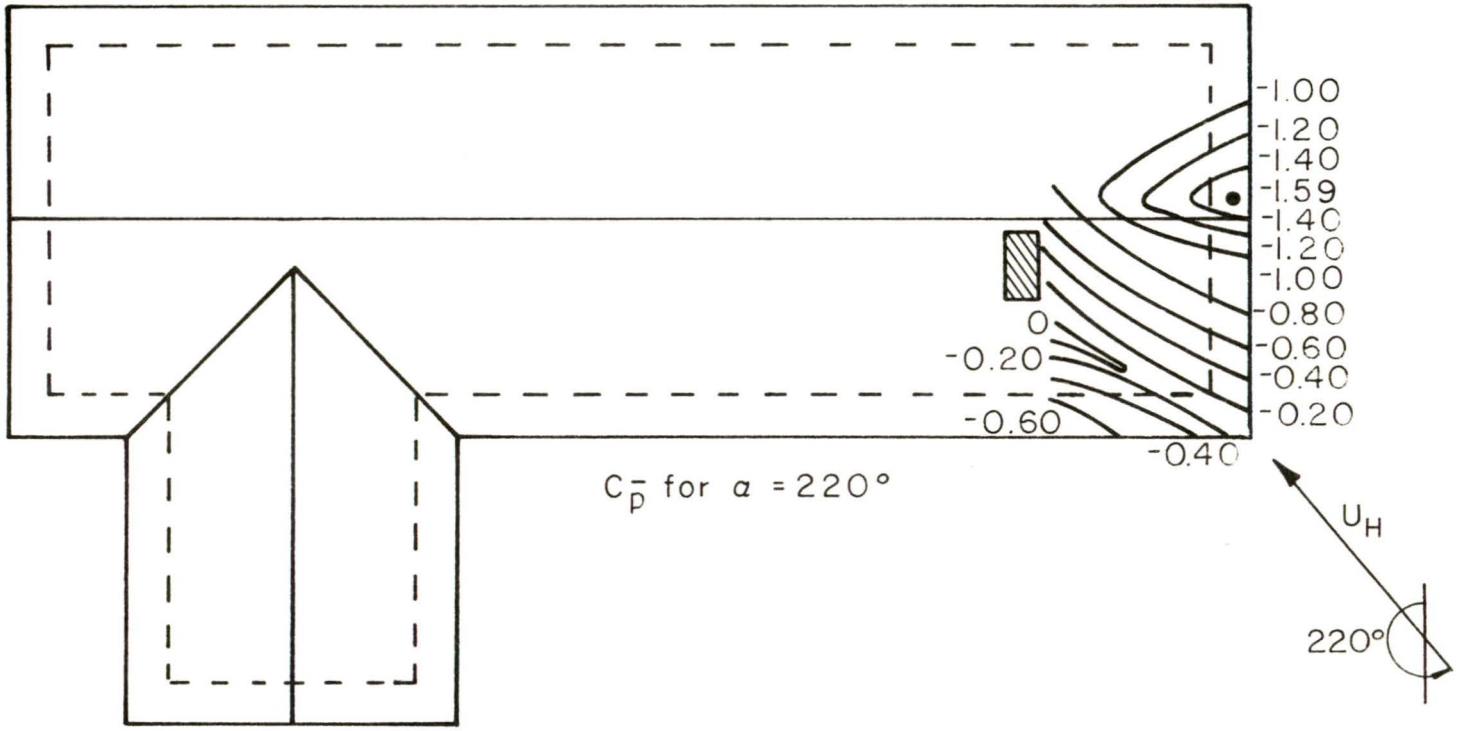

Figure 38. Distribution of mean pressures on top of roof for $\alpha = 220°$

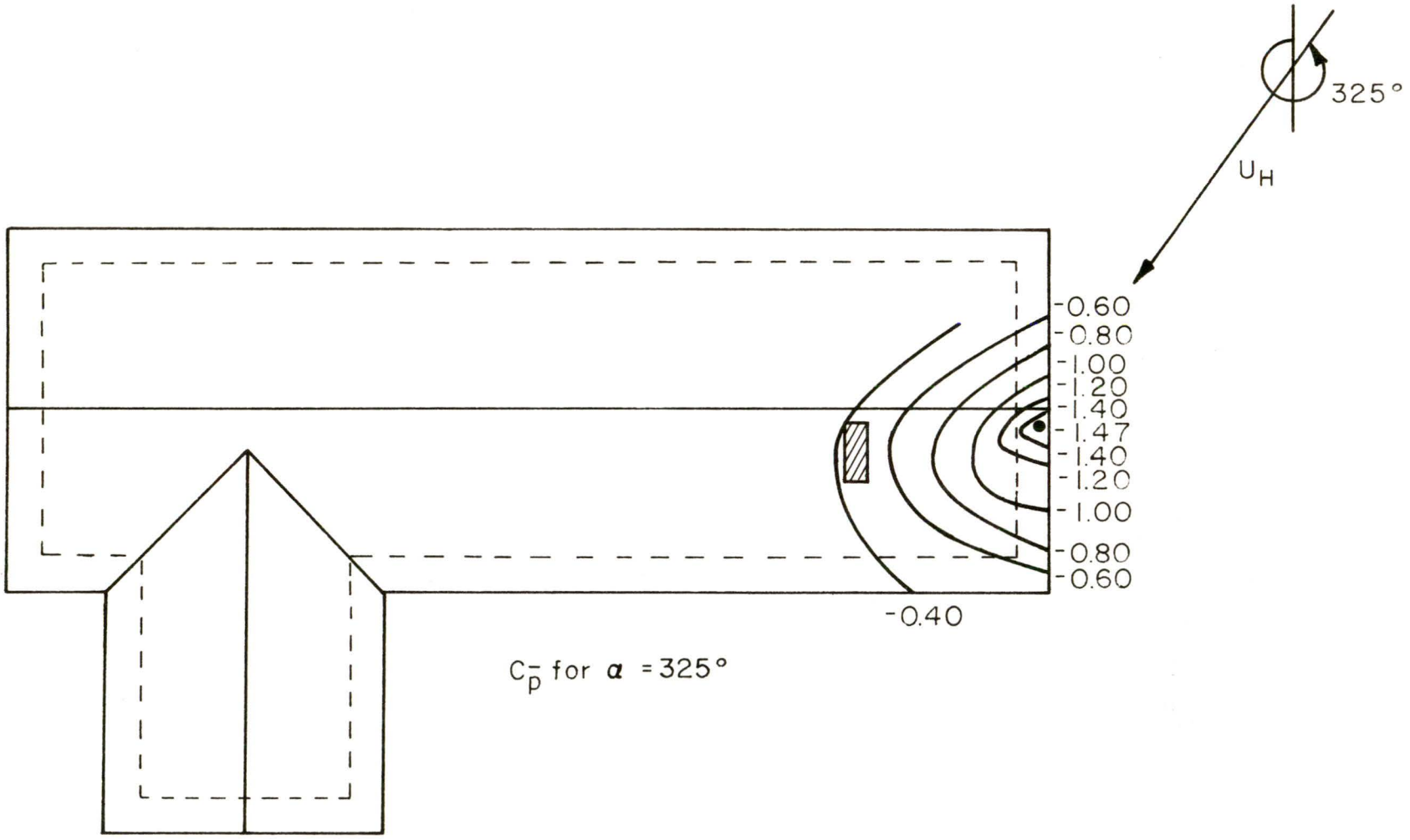

Figure 39. Distribution of mean pressures on top of roof for α = 325°

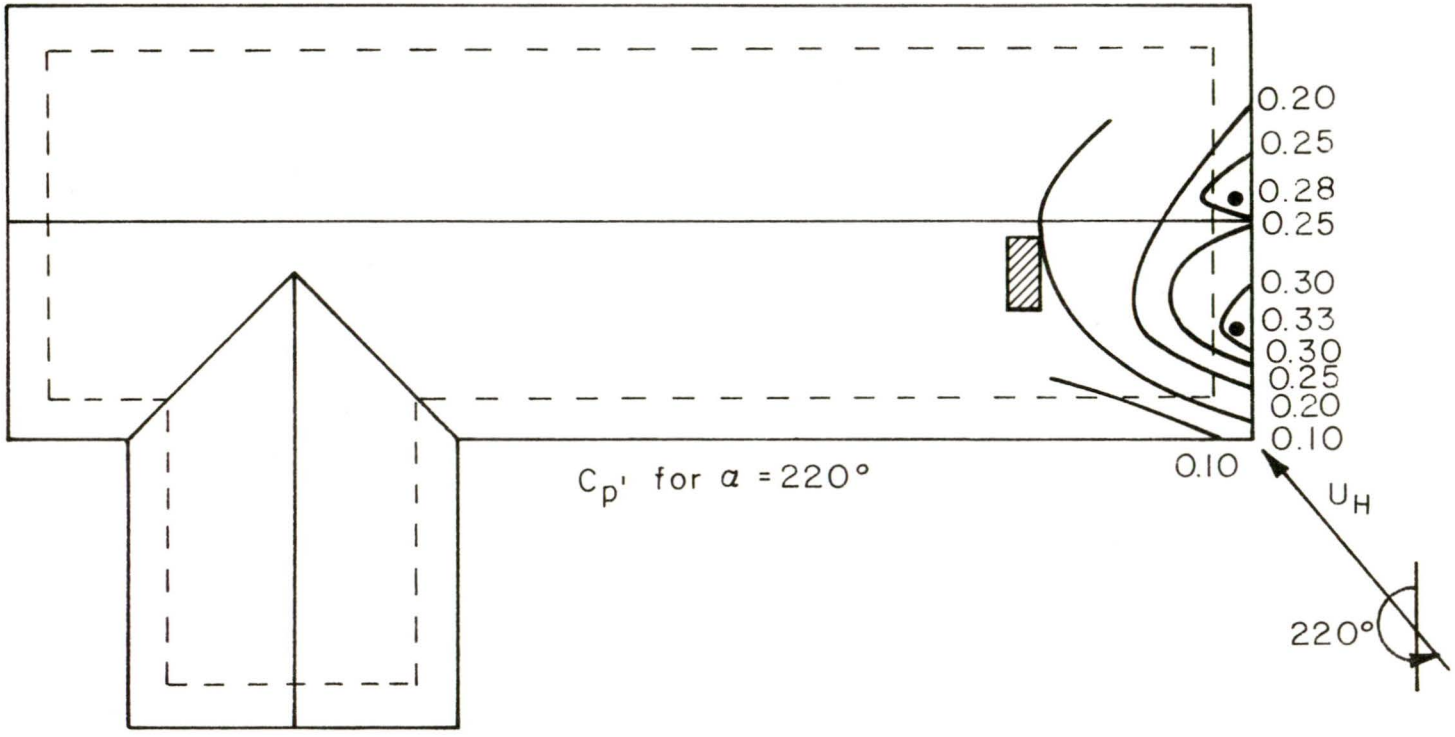

Figure 40. Distribution of RMS pressure fluctuations on top of roof for $\alpha = 220°$

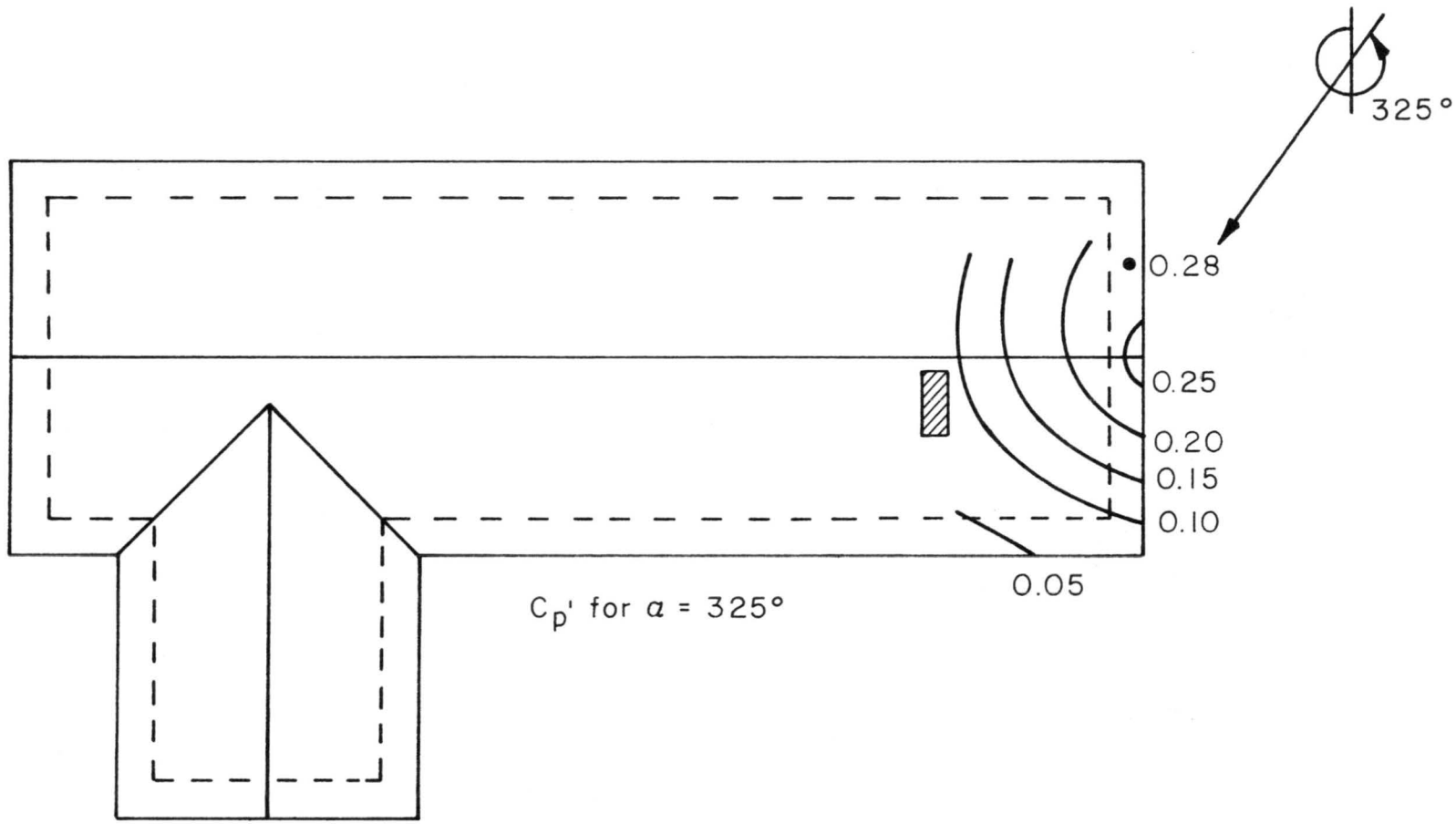

Figure 41. Distribution of RMS pressure flucutations on top of roof for α = 325°

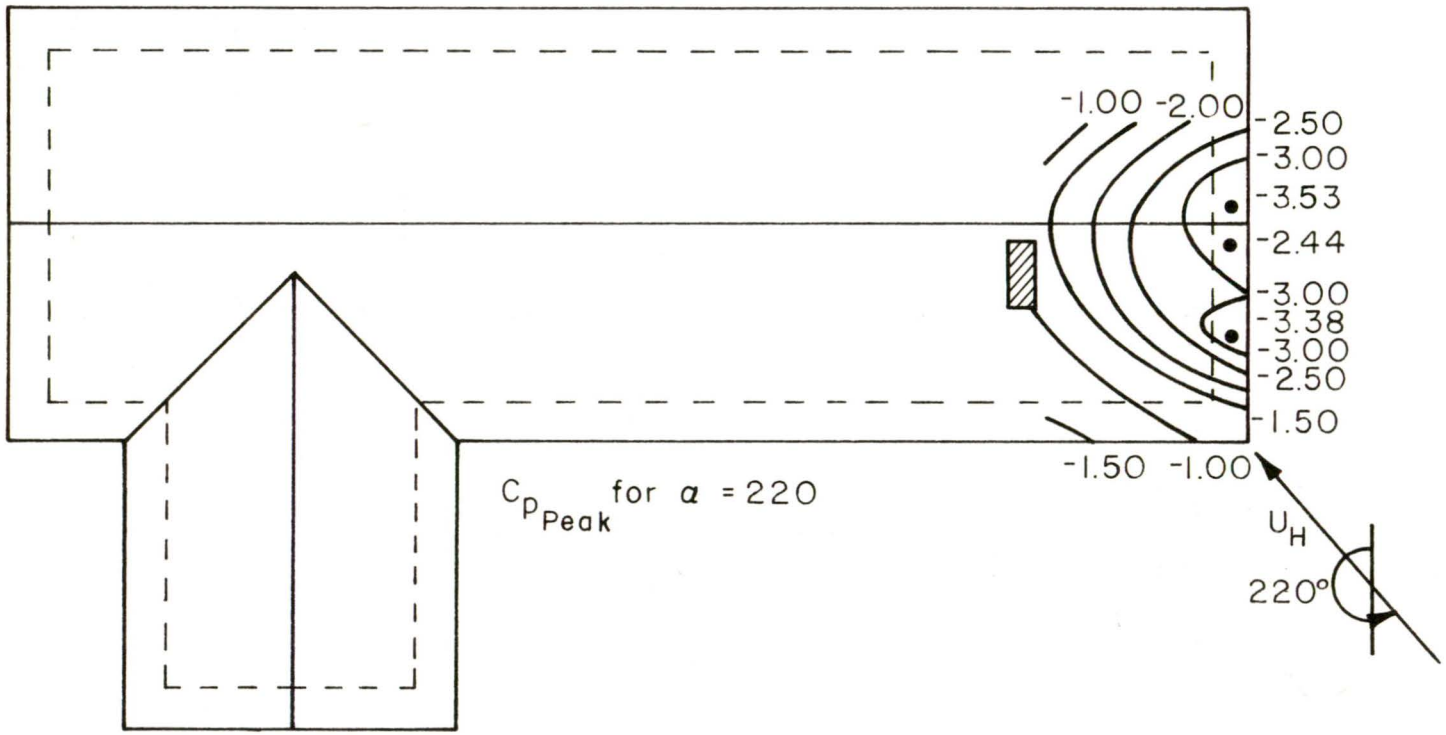

Figure 42. Distribution of peak pressures on top of roof for $\alpha = 220°$

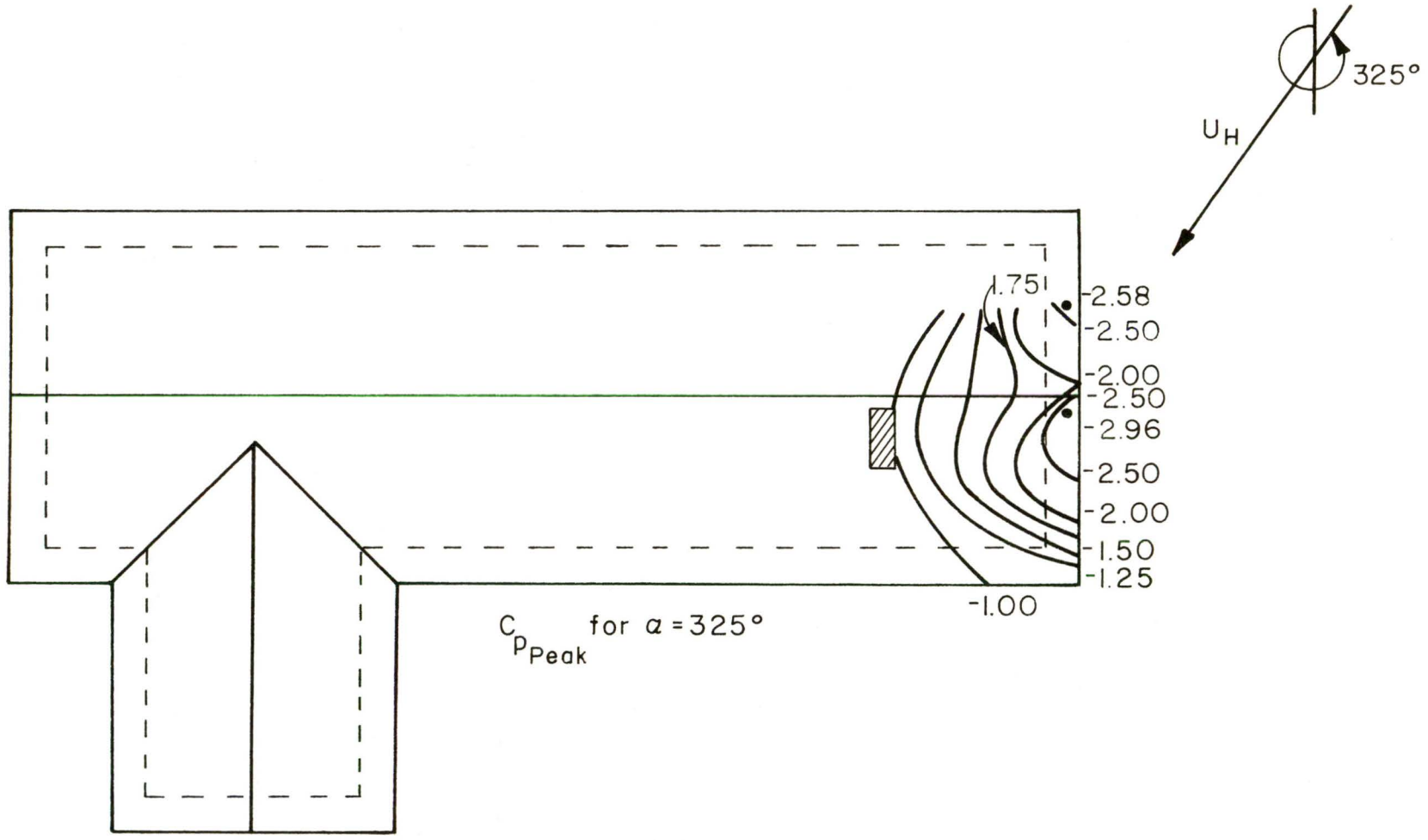

Figure 43. Distribution of peak pressures on top of roof for α = 325°

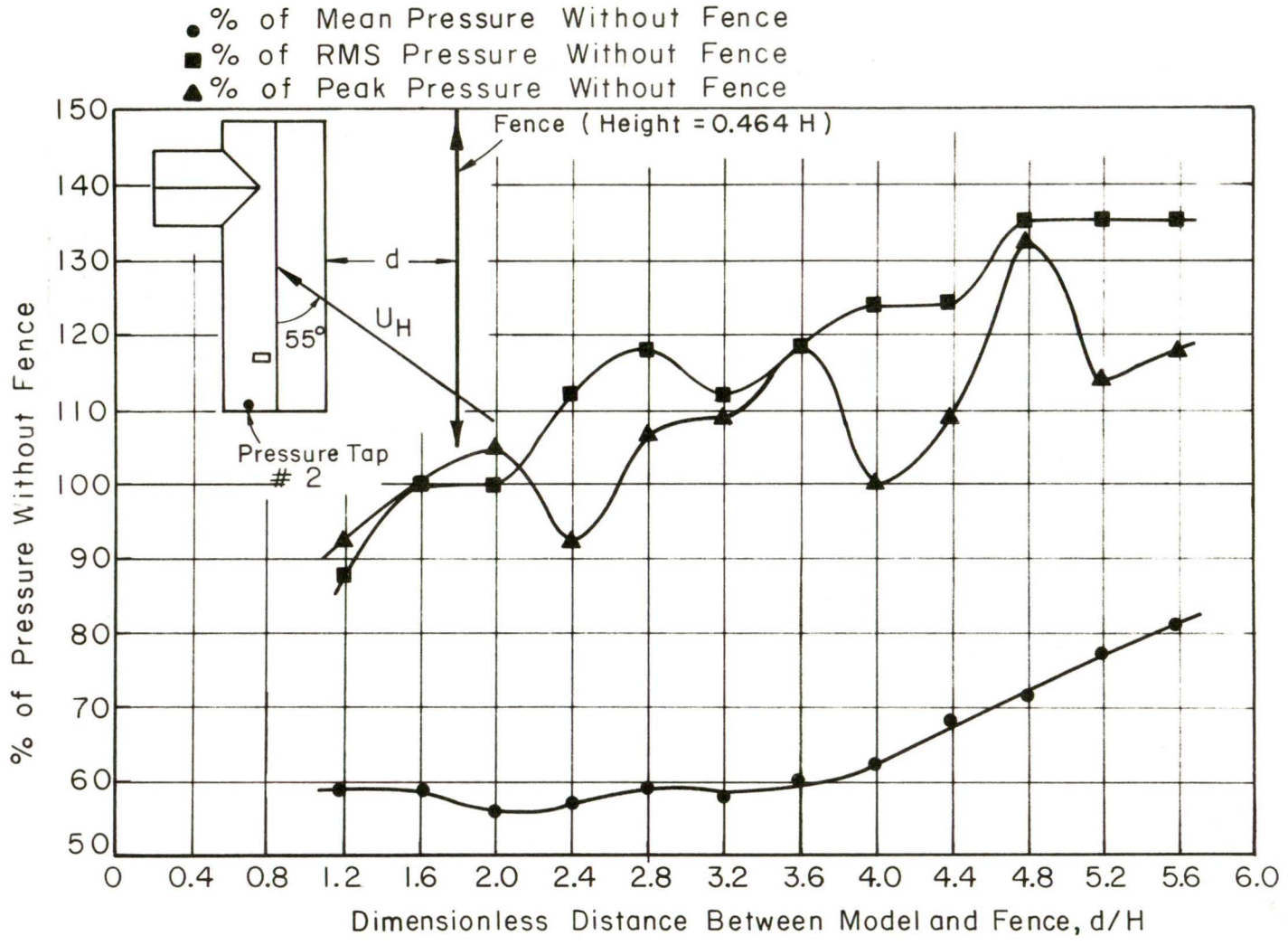

Figure 44. Relative effects of solid fence on roof pressure at pressure tap #2

APPENDICES

APPENDIX A

EQUIPMENT LIST

Amplifier

Dana DC - Model 3500

Output:	±10 v
Impedance:	250 milliohms
Input Impedance:	10 megaohms
Frequency Response:	DC to 20 kc, full amplitude ±1 db
Zero Drift:	±0.02% after a 30 min warmup and 200 hr of operation

Correlation Computer

Princeton Correlation Computer - Model 100

Frequency Range:	DC to 250 kHz
Input Voltage Limit:	±200 v DC or RMS
Operations Performed:	cross-correlation or autocorrelation functions
Averaging Time:	nominally 20 sec
Computation Error:	less than 1% of true value
Calibration Accuracy:	±2%
Zero Drift:	±10 mv/hr
Linearity:	within 1%
Delay Range:	100 microseconds to 10 sec

Hot-Wire Anemometer

CSU Constant-Temperature Hot-Wire Anemometer

Noise:	200 microvolts maximum
Frequency Response:	greater than 100 kHz

Hot-Wire Probe

Base - Disa model 55A20
Tip - Disa model 55A22

Oscillator

General Radio - Model 1309-A

Range:	10 Hz to 100 kHz
Accuracy:	±2% of setting
Stability:	0.01% after warmup
Output Impedance:	600 ohms
Distortion:	less than 0.05% for 200 Hz to 10 kHz
Hum:	less than 0.001% of full output

Oscilloscopes

Tektronix Dual-Beam - Model 502A

Tektronix Storage - Model 564

Power Supply

Harris - Model 6226A

Output:	0-36 v DC, 0-1.5 amps
Load Regulation:	less than 0.02% (constant voltage)
Ripple and Noise:	less than 500 microvolts rms
Stability:	drift less than 0.05%

Pressure Meter

MKS Baratron - Type 77H

Sensitivity:	0.00001 of full scale over entire operating range
Range:	±30 mm Hg differential
Accuracy:	0.02% of full range
DC Voltage Output:	0 to ±100 mv
Speed of Response:	less than 10 milliseconds for 63% response to a step pressure of 30 mm Hg

Pressure Transducers

Validyne - Model DP 15 with CD15 Sine Wave Carrier Demodulator

Range:	±0.1 psi differential
Linearity:	±0.5%
Hysteresis:	0.5%
Overpressure:	to 200% of range in either direction with less than 0.5% zero shift
Inductance:	20mh nominal each coil
Excitation:	5kHz
Output:	0 to ±10 v DC
Output Impedance:	10 ohms nominal
Frequency Response:	flat 0 to 200 Hz within ±5%
Stability:	±0.25% long term

Statham - Model PM283TC

Range:	±0.15 psi differential
Maximum Pressure:	±0.3 psi differential
Natural Frequency:	2,000 Hz
Bridge Resistance:	350 ohms
Excitation:	5 v DC
Full-Scale Output:	±4 mv/v nominal
Resolution:	infinitesimal
Linearity and Hysteresis:	less than 0.75% full scale

Tape Recorders

Honeywell Portable - Model 5600

Ampex - Model FR-1300

APPENDIX B

TABULATED PRESSURE COEFFICIENTS

The mean, fluctuating, and instantaneous peak pressure coefficients obtained from this study were computed for $U_{ref} = 71$ ft/sec and $\rho = 0.00224$ slugs/ft^3. The numbering of the pressure taps is shown in Figure 12, and the wind incidence angles α are shown in Figure 20.

MEAN PRESSURE COEFFICIENTS

Pressure Tap / Incidence Angle	1	2	3	4	5	6	7	8	9	10	11
5	-0.26	-0.39	-0.76	-0.52	-0.35	-0.25	-0.46	-0.32	-0.22	-0.56	-0.45
25	-0.30	-0.43	-0.48	-0.38	-0.29	-0.26	-0.53	-0.35	-0.21	-0.31	-0.48
45	-0.28	-0.31	-0.38	-0.33	-0.28	-0.29	-0.65	-0.34	-0.21	-0.30	-0.39
65	-0.19	-0.21	-0.27	-0.24	-0.21	-0.25	-0.59	-0.33	-0.08	-0.24	-0.23
85	-0.12	-0.11	-0.12	-0.12	-0.12	-0.12	-0.29	-0.30	-0.02	-0.15	-0.11
105	-0.14	-0.13	-0.14	-0.16	-0.14	-0.27	-0.16	-0.41	+0.04	-0.18	-0.15
125	-0.29	-0.23	-0.24	-0.30	-0.20	-0.35	-0.23	-0.59	+0.04	-0.23	-0.26
145	-0.58	-0.30	-0.33	-0.43	-0.31	-0.81	-0.35	-0.61	+0.31	-0.29	-0.34
165	-0.80	-0.32	-0.43	-0.60	-0.40	-0.99	-0.37	-0.58	+0.45	-0.37	-0.30
185	-0.64	-0.31	-0.47	-0.79	-0.43	-1.03	-0.24	-0.69	+0.49	-0.30	-0.35
205	-0.08	-0.29	-0.78	-1.03	-1.08	-0.87	-0.04	-0.77	+0.50	+0.20	-0.39
210	-0.05	-0.37	-0.89	-1.29	-1.12	-0.84	+0.02	-0.78	+0.50	+0.28	-0.39
215	-0.06	-0.52	-1.03	-1.47	-1.09	-0.82	+0.05	-0.80	+0.48	+0.34	-0.39
220	-0.08	-0.71	-1.16	-1.59	-1.03	-0.78	+0.05	-0.77	+0.43	+0.38	-0.37
225	-0.10	-0.95	-1.23	-1.62	-1.02	-0.74	+0.05	-0.74	+0.40	+0.44	-0.38
230	-0.09	-1.17	-1.27	-1.59	-0.99	-0.68	+0.05	-0.68	+0.36	+0.50	-0.35
235	-0.11	-1.32	-1.26	-1.47	-0.95	-0.57	+0.04	-0.58	+0.30	+0.56	-0.33
240	-0.12	-1.39	-1.23	-1.32				-0.50	+0.25	+0.60	-0.30
245	-0.13	-1.45	-1.14	-1.17	-0.84	-0.41	0.00	-0.31	+0.18	+0.60	-0.28
265	-0.92	-1.01	-0.72	-0.69	-0.69	-0.20	-0.06	-0.07	-0.12	+0.68	-0.29
285	-0.79	-0.67	-0.66	-0.71	-0.95	-0.33	-0.31	-0.06	-0.29	+0.68	-0.13
305	-0.51	-0.78	-1.12	-1.12	-1.15	-0.37	-0.40	-0.05	-0.32	+0.53	-0.16
325	-0.52	-1.11	-1.47	-1.06	-0.62	-0.38	-0.52	-0.43	-0.33	+0.27	-0.17
345	-0.49	-0.91	-0.79	-0.50	-0.22	-0.32	-0.54	-0.17	-0.27	-0.12	-0.33

RMS PRESSURE COEFFICIENTS

Pressure Tap / Incidence Angle	1	2	3	4	5	6	7	8	9	10	11
5	0.08	0.10	0.13	0.07	0.07	0.04	0.10	0.06	0.04	0.12	0.07
25	0.10	0.13	0.11	0.08	0.08	0.05	0.12	0.06	0.04	0.06	0.07
45	0.06	0.05	0.07	0.05	0.07	0.04	0.12	0.07	0.04	0.04	0.06
65	0.05	0.05	0.05	0.04	0.05	0.04	0.14	0.06	0.05	0.04	0.04
85	0.04	0.04	0.04	0.04	0.04	0.04	0.10	0.05	0.05	0.04	0.02
105	0.04	0.04	0.04	0.05	0.05	0.05	0.05	0.14	0.05	0.03	0.03
125	0.09	0.04	0.04	0.06	0.17	0.14	0.05	0.12	0.09	0.04	0.04
145	0.16	0.07	0.07	0.10	0.09	0.16	0.14	0.12	0.12	0.05	0.04
165	0.19	0.06	0.08	0.15	0.18	0.16	0.14	0.11	0.15	0.10	0.04
185	0.24	0.07	0.07	0.13	0.22	0.16	0.13	0.12	0.17	0.20	0.05
205	0.16	0.14	0.25	0.38	0.18	0.15	0.11	0.13	0.13	0.11	0.05
210	0.10	0.22	0.27	0.42	0.18	0.14	0.09	0.14	0.12	0.11	0.05
215	0.09	0.27	0.24	0.37	0.20	0.14	0.08	0.13	0.11	0.11	0.05
220	0.09	0.33	0.23	0.28	0.20	0.13	0.06	0.12	0.10	0.12	0.05
225	0.08	0.34	0.18	0.28	0.20	0.13	0.06	0.12	0.10	0.12	0.04
230	0.08	0.31	0.18	0.24	0.17	0.13	0.06	0.12	0.11	0.13	0.04
235	0.09	0.31	0.18	0.26	0.16	0.13	0.06	0.12	0.10	0.13	0.05
240	0.08	0.31	0.19	0.23				0.11	0.10	0.14	0.05
245	0.09	0.32	0.19	0.25	0.15	0.13	0.05	0.12	0.09	0.15	0.05
265	0.38	0.23	0.14	0.14	0.16	0.10	0.08	0.12	0.13	0.17	0.06
285	0.22	0.14	0.12	0.13	0.20	0.10	0.10	0.09	0.07	0.16	0.03
305	0.12	0.12	0.23	0.16	0.22	0.06	0.06	0.05	0.04	0.13	0.02
325	0.07	0.17	0.25	0.25	0.28	0.04	0.07	0.12	0.04	0.11	0.04
345	0.09	0.23	0.24	0.13	0.09	0.04	0.08	0.05	0.04	0.18	0.06

PEAK PRESSURE COEFFICIENTS

Pressure Tap / Incidence Angle	1	2	3	4	5	6	7	8	9	10	11
5	-0.95	-1.73	-1.42	-0.87	-0.82	-0.55	-1.23	-0.74	-0.42	-1.10	-0.95
25	-1.18	-2.50	-1.23	-0.72	-0.85	-0.80	-1.32	-0.76	-0.49	-0.79	-1.18
45	-0.65	-1.03	-0.77	-0.67	-0.78	-0.65	-1.51	-0.72	-0.41	-0.51	-0.65
65	-0.50	-0.55	-0.55	-0.42	-0.52	-0.52	-1.54	-0.74	-0.33	-0.43	-0.50
85	-0.38	-0.45	-0.33	-0.30	-0.37	-0.37	-1.16	-0.62	-0.31	-0.34	-0.38
105	-0.39	-0.48	-0.26	-0.44	-0.40	-0.44	-0.45	-1.45	+0.32	-0.34	-0.39
125	-1.07	-0.63	-0.49	-0.65	-0.53	-1.05	-0.64	-1.32	+0.55	-0.44	-1.07
145	-1.74	-0.81	-0.75	-1.03	-1.49	-1.77	-1.03	-1.40	+1.23	-0.34	-1.74
165	-2.07	-0.84	-0.98	-1.61	-1.87	-2.03	-1.11	-1.20	+1.29	-0.98	-2.07
185	-1.81	-0.97	-1.09	-1.55	-1.61	-2.03	-0.84	-1.36	+1.38	-1.55	-1.81
205	-1.48	-2.07	-1.96	-3.20	-2.24	-2.09	-0.66	-1.52	+1.38	+0.82	-1.48
210	-1.39	-2.16	-2.22	-3.11	-2.25	-1.61	-0.65	-1.46	+1.47	+1.11	-1.39
215	-0.86	-2.28	-2.44	-3.20	-2.32	-1.71	-0.61	-1.43	+1.18	+1.22	-0.86
220	-0.70	-3.38	-2.44	-3.53	-2.51	-1.58	-0.66	-1.46	+1.31	+1.08	-0.70
225	-0.52	-3.22	-2.48	-3.44	-2.28	-1.45	+0.42	-1.46	+1.02	+1.14	-0.52
230	-0.67	-3.30	-2.44	-3.53	-2.48	-1.45	+0.42	-1.49	+1.21	+1.32	-0.67
235	-0.57	-3.72	-2.48	-3.53	-2.09	-1.30	+0.39	-1.27	+0.88	+1.45	-0.57
240	-1.35	-4.15	-2.41	-2.95				-1.17	+0.82	+1.32	-1.35
245	-1.46	-3.64	-2.31	-2.58	-1.96	-1.30	+0.31	-0.95	+0.78	+1.34	-1.46
265	-2.27	-3.30	-1.75	-1.80	-2.32	-0.94	-0.60	-0.95	-0.74	+1.47	-2.27
285	-2.47	-2.33	-1.78	-1.83	-2.58	-1.14	-0.83	-0.79	-0.72	+1.54	-2.47
305	-1.88	-2.33	-2.57	-2.29	-2.58	-0.68	-0.78	-0.30	-0.56	+1.34	-1.88
325	-1.16	-2.37	-2.96	-2.03	-2.58	-0.67	-0.96	-1.12	-0.59	+1.01	-1.16
345	-0.92	-2.33	-2.46	-1.50	-1.27	-0.55	-0.99	-0.58	-0.46	-0.49	-0.92

APPENDIX C

CORRELATION OF MODEL PRESSURES WITH FULL-SCALE PRESSURES

The adequacy of results obtained from a wind-tunnel simulation of wind-induced pressures on a structure is best determined by comparing the simulated pressures with pressures acting on the full-scale structure. Although comparisons have been made for mean pressures on house roofs, comparisons of fluctuating roof pressures have not been made. The purpose of a study currently being conducted by the National Bureau of Standards Center for Building Technology and the Fluid Dynamics and Diffusion Laboratory of Colorado State University is to compare both mean and fluctuating pressures acting on the roof of a prototype house with pressures obtained from a model of the house placed in an appropriate wind-tunnel flow.*

The particular house chosen for this investigation is the ranch-style house shown in Figure 3. This house is located on Malmstrom Air Force Base just outside of Great Falls, Montana. The Validyne pressure transducers described in Appendix A were placed at 11 locations on the roof of the house where the severest wind effects were expected to occur. The transducers were mounted under aluminum housings and were connected to pressure taps in the center of the housings with short lengths of Tygon tubing. Some of the transducers and associated housings are shown installed on the roof in Figure C1. The instrumentation for the full-scale house also included a cup anemometer, a propeller anemometer, and a static pressure probe. These were mounted approximately

---

* The principal investigator for this study is Dr. R. D. Marshall of the National Bureau of Standards.

10 ft above the roof on a mast. When wind speeds reached 30 mph, signals from the anemometers and the 11 pressure transducers were simultaneously recorded on tape.

The 1:50 scale model of the house is shown in Figure 4, and the locations of the pressure taps corresponding to the transducer positions on the prototype house are shown in Figure 12. This model was placed in the wind tunnel shown in Figure 8 where the approaching wind was simulated by use of vortex generators (Figures 10 and 11) and appropriate upstream roughness for the predominant wind directions shown in Figure C2. The model house and roughness configuration is shown in Figure C3 for the wind azimuth of 256^{o} in Figure C2. For the four wind directions, the outputs of the 11 pressure transducers were simultaneously recorded with the signals from a hot-wire anemometer and a pitot-static probe positioned to correspond to the location of the anemometers mounted above the prototype house.

The data from both the prototype and model houses is being digitally analyzed by the National Bureau of Standards. At the present time, results from the prototype house are not available and the model-study data have only been partially analyzed. When the study is completed, the following will have been computed for each pressure tap and wind direction for both model and prototype houses:

(1) mean pressure coefficient,

(2) RMS fluctuating pressure coefficient,

(3) autocorrelation function of the pressure fluctuations,

(4) power spectrum of the energy of the pressure fluctuations, and

(5) cross-correlation function between velocity fluctuations and pressure fluctuations.

These results should soon be available in a report to be issued by the National Bureau of Standards Center for Building Technology.

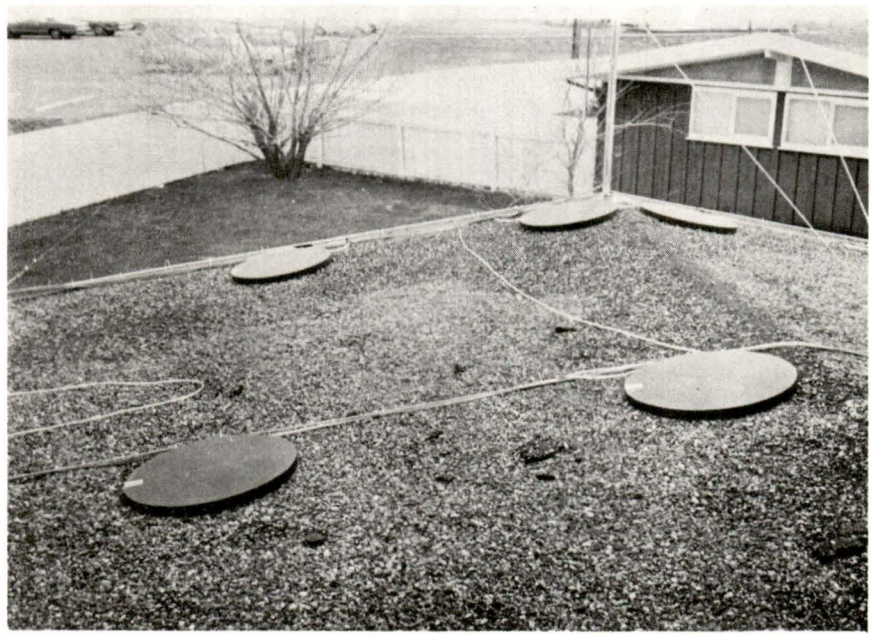

Figure C1. Transducers and aluminum housings installed on the roof of the prototype house

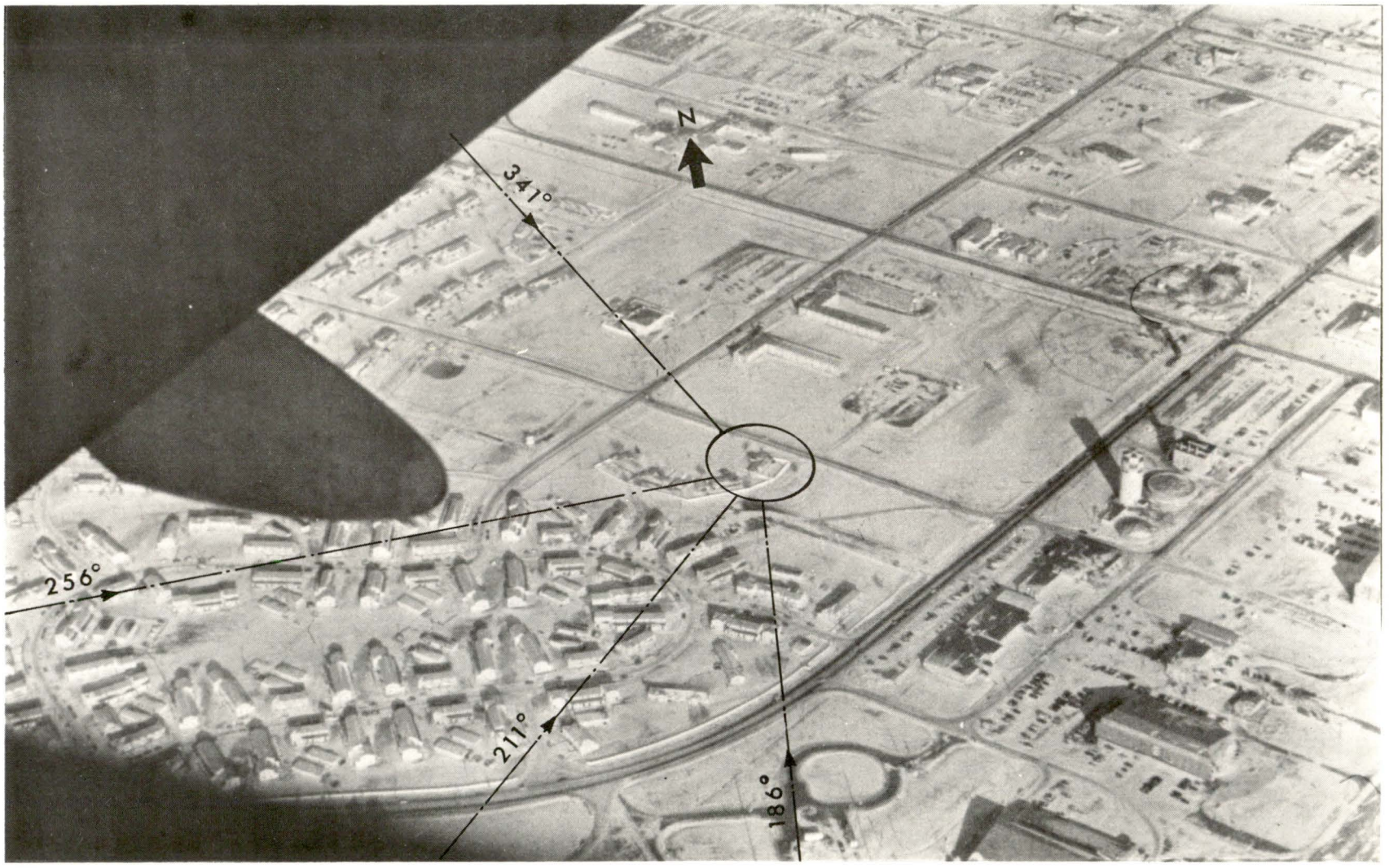

Figure C2. Azimuths of predominant wind directions

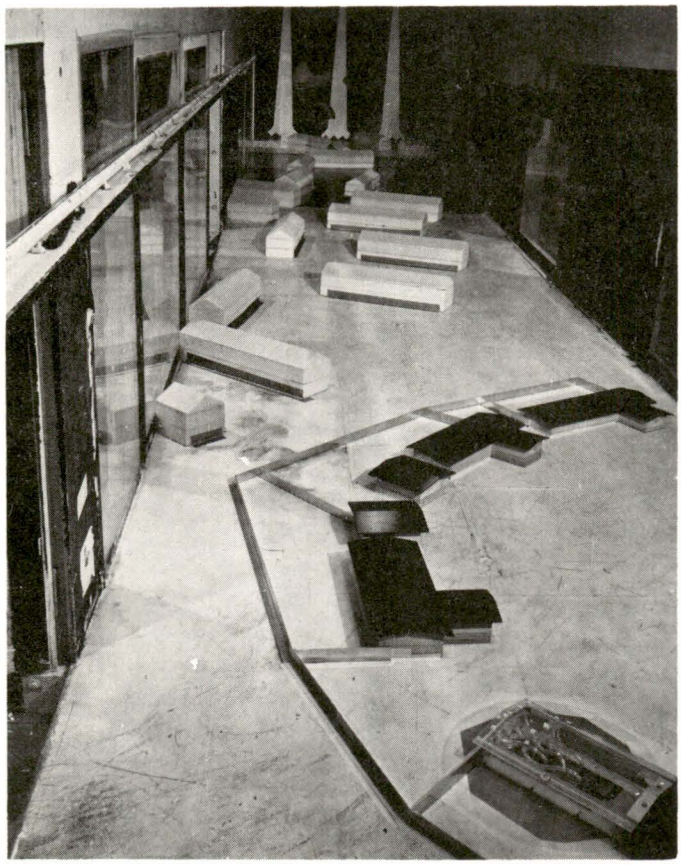

Figure C3. Model house and upstream configuration for wind azimuth of 256°